Investigation of structural phase stability of some polyhedral compounds of Group 3A under high pressure

By

ABHILASH DWIVEDI

PHYS01201204008

Bhabha Atomic Research Centre, Mumbai

A thesis submitted to the

Board of Studies in Physical Sciences

In partial fulfillment of requirements

for the Degree of

DOCTOR OF PHILOSOPHY

of

HOMI BHABHA NATIONAL INSTITUTE

December, 2018

Version approved during the meeting of Standing Committee of Deans held during 29-30 Nov 2013

Homi Bhabha National Institute[1]

Recommendations of the Viva Voce Committee

As members of the Viva Voce Committee, we certify that we have read the dissertation prepared by Abhilash Dwivedi entitled " Investigation of structural phase stability of some polyhedral compounds of Group 3A under high pressure " and recommend that it may be accepted as fulfilling the thesis requirement for the award of Degree of Doctor of Philosophy.

Chairman - Dr. T. C. Kaushik **Date:** 18/07/2019

Guide / Convener - Dr. Chitra Murli **Date:** 18/7/19

Examiner - Dr. Amartya Sengupta **Date:** 18/7/19

Member 1- Dr. S. C. Gadkari **Date:** July 18, 2019

Member 2- Dr. M. N. Deo **Date:** 18/07/2019

Member 3- Dr. A. K. Sinha **Date:** 31/07/2019

Technology Adviser- Dr. N. L. Misra **Date:** 18/07/2019

Final approval and acceptance of this thesis is contingent upon the candidate's submission of the final copies of the thesis to HBNI.

I/~~We~~ hereby certify that I/~~we~~ have read this thesis prepared under my/~~our~~ direction and recommend that it may be accepted as fulfilling the thesis requirement.

Date: 18/07/19

Place: Mumbai

18/7/19

Dr. Chitra Murli

(Guide)

---

[1] This page is to be included only for final submission after successful completion of viva voce.

STATEMENT BY AUTHOR

This dissertation has been submitted in partial fulfillment of requirements for an advanced degree at Homi Bhabha National Institute (HBNI) and is deposited in the Library to be made available to borrowers under rules of the HBNI.

Brief quotations from this dissertation are allowable without special permission, provided that accurate acknowledgement of source is made. Requests for permission for extended quotation from or reproduction of this manuscript in whole or in part may be granted by the Competent Authority of HBNI when in his or her judgment the proposed use of the material is in the interests of scholarship. In all other instances, however, permission must be obtained from the author.

Abhilash Dwivedi

Abhilash Dwivedi

Version approved during the meeting of Standing Committee of Deans held during 29-30 Nov 2013

DECLARATION

I, hereby declare that the investigation presented in the thesis has been carried out by me. The work is original and has not been submitted earlier as a whole or in part for a degree / diploma at this or any other Institution / University.

Abhilash Dwivedi

Abhilash Dwivedi

Version approved during the meeting of Standing Committee of Deans held during 29-30 Nov 2013

List of Publications arising from the thesis

Journals

1. High pressure structural investigations on hexagonal $YInO_3$; **A. Dwivedi**, H. K. Poswal, R. Shukla, S. Velaga, B. D. Sahoo, V. Grover and M. N. Deo, High Pressure Research **39**, 17 (2019).
2. High pressure studies on α-cristobalite form of $Al_{0.5}Ga_{0.5}PO_4$: Hydrostatic versus Non-hydrostatic conditions, **A. Dwivedi**, H. K. Poswal, K. K. Pandey, H. P. Liermann, C. Murli and M. N. Deo, High Pressure Research **39**, 81 (2019).
3. Physics under extreme conditions using Indus-2 synchrotron radiation source, K. K. Pandey, H. K. Poswal, A. K. Mishra, V. Srihari, N. Garg, **A. Dwivedi**, R. Vasanthi, M. N. Deo, and S. M. Sharma, Physics News; Bulletin of the Indian Physics Association **48,** 48 (2018).
4. High pressure structural investigations on $InPO_4$; **A. Dwivedi**, R. Kaiwart, M. Varma, S. Velaga and H. K. Poswal (Journal of Solid State Chemistry, under review).

Conferences

1. **Abhilash Dwivedi**, H. K. Poswal, R. Shukla, V. Grover and M. N. Deo; High pressure Raman studies on hexagonal $YInO_3$; International Conference on Perspectives in Vibrational Spectroscopy; 117, 65 (2018).
2. **Abhilash Dwivedi**, K. K. Pandey and H. K. Poswal; Development of square spiral scanning software to align high pressure Diamond Anvil Cell at BL-11, Indus-2 synchrotron; Proceedings of the DAE Solid State Physics Symposium, D-130, 139 (2017).

3. **Abhilash Dwivedi**, H. K. Poswal, Srihari Velaga, R. Shukla, V. Grover and Surinder M. Sharma; Structural phase stability of (1%) Eu^{3+} doped $YInO_3$ under high pressure; DAE-BRNS Conference on Condensed Matter Physics Under Extreme Conditions, P-2, 36 (2016).
4. **Abhilash Dwivedi**, H. K. Poswal, K. K. Pandey and Surinder M. Sharma; High pressure structural investigation on cristobalite form of $Al_{0.5}Ga_{0.5}PO_4$; Proceedings of the DAE Solid State Physics Symposium, A 160, 68 (2014).
5. **Abhilash Dwivedi**, Ashwani Kumar, Biplab Ghosh, H K Poswal, Ravindra Makde, Surinder M Sharma; Development of energy scanning software to facilitate MAD experiment at PX-BL21, Indus-2 synchrotron; AIP Conference Proceedings 1832, 060013 (2017).
6. **Abhilash Dwivedi**, Rahul Kaiwart and H K Poswal; High pressure structural investigations on $InPO_4$; 47th National Seminar on Crystallography, AB 140, 171 (2019).

Abhilash Dwivedi

Abhilash Dwivedi

Dedicated

to

My father

Late Krishna Chandra Dwivedi

ACKNOWLEDGEMENTS

I would like to thank all the people who have helped me during my doctoral work. My special thanks to Dr. S. M. Sharma for motivating me in this work.

I would like to express my gratitude to Dr. H. K. Poswal for his constant support and encouragement during my doctoral work. I am very thankful to Dr. K. K. Pandey, Dr. A. K. Mishra, Dr. Srihari Velaga, Dr. Nishant Patel, Dr. B. D. Sahoo and Dr. Rakesh Shukla for their valuable scientific discussions. I am very thankful to Shri Rahul Kaiwat for his precious support.

I am thankful to the members of my doctoral committee Dr. T. C. Kaushik, Dr. S. C. Gadkari, Dr. M. N. Deo, Dr. A. K. Sinha and Dr. N. L. Misra for their critical comments and suggestions. My special thanks to Dr. Chitra Murli for her valuable support. I would like to thank Dr. Nandini Garg, Dr. M. Sunder, Dr. Alka Garg, Smt. R. Vasanthi, Smt. Saheli Banerjee, Shri Milind Tandel, Shri Rajendra Pokhale, Ms Meera Varma and Shri Abhishek Chitnish for their generous help during the Ph. D. work.

I express my sincere gratitude to my parents (Late K. C. Dwivedi, Smt. Sushila Dwivedi), my brother (Dr. S. K. Dwivedi), my sisters and my friend Narmada for their continuous encouragement and support.

SYNOPSIS

Pressure is an important thermo-dynamic variable, which is defined as force per unit area. The effect of pressure on materials is to produce lattice compression, change in electronic structure, increase in the energy band widths, shifting of energy bands with respect to Fermi energy, shifting of Fermi level itself etc. These effects produce a variety of remarkable changes in the properties of material, such as transition from an insulator to a metal [1], a normal material to a superconductor [2], a magnetic substance to a non-magnetic one [3], synthesis of novel stoichiometric compounds [4] etc. The framework structures cover a wide range of compounds of importance in the Earth sciences, condensed matter physics, and materials sciences. These compounds have three-dimensional networks of relatively rigid polyhedral units that share corners with one another. These structures are open and provide enough flexibility to form new denser structures under compression. The forces which act within the polyhedral units are much stronger than the forces that act between them. In general, it is much easier to tilt the polyhedral unit than to distort polyhedra [5]. Several polyhedral compounds of Group 3A, such as APO_4 (where, $A = Al, Ga, In$) and its solid solutions, $YAlO_3$ and $YInO_3$ have framework structures. These materials have various technological applications. For example, $AlPO_4$ is used in binder for silica fibres in thermal power plant [6] and protective coating on *C-C* composites in aircraft [7]. The solid solution of $AlPO_4$ and $GaPO_4$ is used in piezoelectric resonators [8]. In fact, structural distortion in system $Al_{1-x}Ga_xPO_4$ varies linearly as a function of *Ga* composition (x), which provides the opportunity to tune its piezoelectric properties [9]. $InPO_4$ has been used in electronic, optoelectronics and telecommunications industries [10]. $YMnO_3$ is a well known multiferroic compound [11]. The structural behaviour of $YInO_3$ under high pressure is useful to explore the geometric ferroelectric behavior observed in $YMnO_3$ type multiferroic compounds. In addition to this, $YInO_3$ doped with *Fe* may be useful for lead free relaxors [12]. $YInO_3$ doped with *Eu* is proposed as efficient red phosphor with high red colour purity [13].

Apart from technological applications, these materials have also geological importance. APO_4 (where, *A* = *Al*, *Ga*, *In*) and its solid solutions are isoelectronic analogous form of silica and form isostructural compounds. High pressure investigation on APO_4 type materials can help in understanding the mechanism of various transformations observed in silica [14, 15] which is the major constituent of the Earth's crust and mantle [16]. Apart from SiO_2, $MgSiO_3$ also exists in high abundance under Earth's lower mantle [17]. The perovskite form of $YAlO_3$ is analogue materials of $MgSiO_3$. Studies show that the high pressure behavior of $YAlO_3$ [18] is in contrast to $MgSiO_3$ in which structural distortion increases with increasing pressure [19]. The Replacement of Al^{3+} (ionic radius 0.54 Å) with bigger size In^{3+} (ionic radius 0.72 Å) [20], can generate internal stress on the structure, therefore high pressure studies of $YInO_3$ compound can help in understanding the structural distortion mechanism in ABO_3 type perovskite.

This thesis deals with the structural behavior of some polyhedral compounds of Group 3A under the application of the pressure. The work may be broadly classified into two parts: I. Instrumentation and technique, II. Materials investigations under pressure. In instrumentation and technique part, various developmental works of Extreme Conditions X- ray Diffraction (ECXRD) beamline, Indus-2 [21] have been presented. In the materials investigations section, the high pressure studies on $Al_{0.5}Ga_{0.5}PO_4$, $InPO_4$ and $YInO_3$ have been described. To the best of my knowledge, no experimental high pressure studies on these compounds are reported.

This thesis consists six chapters, which are described below.

Chapter 1: **Introduction**

This chapter gives a brief overview of the field of high pressure physics. Starting from the basic units of pressure, generation of static pressure methodology and various methods for measurement of pressure are described. The use of diamond anvil cell (DAC) is the most versatile and an established technique for generating the static high pressure [22]. The chapter also includes the preparation and working of DAC in detail. Accurate determination of pressure is one of the most important issues in high pressure DAC based experiments. The most common methods for measuring high pressures are: known equation of state (EOS) of some materials (Au, Cu, Pt etc.) [23] and shift in ruby fluorescence peak with pressure [24]. The detailed descriptions of these methods are given in the chapter. The high pressure behavior of the compounds has been probed with Raman scattering and X-ray diffraction techniques. Raman scattering method provides the information on the local environment of the atoms and explores the microscopic picture of the system [25]. The x-ray diffraction method helps to determine the structure of the material [26]. The brief introduction of Raman scattering and X- ray Diffraction techniques are also given in the chapter. Rietveld refinement is the well established method for refining XRD data [27] which is described in the chapter. A literature survey of high pressure studies on some polyhedral compounds of Group 3A, such as $AlPO_4$, $GaPO_4$ and $YAlO_3$ are also presented in the chapter.

Chapter 2: Extreme Conditions X- ray Diffraction (ECXRD) beamline

High pressure x-ray diffraction experiments have been carried out at Indus-2 and international synchrotron radiation sources. Indus-2 (at Raja Ramanna Centre for Advanced Technology, Indore) is an Indian synchrotron radiation source which is designed to operate at 2.5 GeV, 200 mA. The extreme conditions x-ray diffraction beamline (ECXRD, BL 11) at Indus-2 synchrotron, is optimized for studying the structural behavior of materials under various conditions of pressure and temperature. In this chapter, the design and development of Extreme Conditions X- ray Diffraction (ECXRD) beamline at Indus-2 synchrotron radiation source [21], is presented. Due to high radiation, all the components of the beamline must be remotely controlled. For that, software programs have been written for various components of beamline in Visual Basic 6.0 software language. Brief overviews of these software programs are also described. With the help of user friendly and GUI (graphical user interface) visual basic 6.0 language, a software program has been written for monitoring the on-line intensity of incident x-rays using ionization chamber. One server-client based software program has also been developed to control the movement of slit assembly (Micos, USA make). In our high pressure experiments, the typical diameter of sample chamber of DAC is less than 100 μm and the x-ray beam is to be aligned within ~ 100 μm x 100 μm size. The manual alignment process of sample inside DAC in the path of x-ray beam is cumbersome and time consuming. In addition to this, in case of manual alignment, the sample may not be placed in the vicinity of the most intense position of x-ray beam. This results in poor x-ray diffraction signal and appearance of unwanted gasket peak. To simplify the alignment process of DAC, a scanning program has been made using goniometer stages, picoammeter and x-ray photo diode which is also described in the chapter.

Chapter 3: High pressure studies on α-cristobalite form of $Al_{0.5}Ga_{0.5}PO_4$

The earlier high pressure investigations on α-cristobalite (orthorhombic $C222_1$) form of $AlPO_4$ show that its high pressure behaviour significantly depends on the nature of non-hydrostatic pressure conditions. This compound transforms to monoclinic phase at 4 GPa which on further compression to 11 GPa transform to $VCrO_4$ type orthorhombic *Cmcm* phase under non-hydrostatic pressure conditions [28]. In contrast to this under hydrostatic conditions, ambient α-$AlPO_4$ directly transforms to the *Cmcm* phase with N_2 as pressure transmitting medium (PTM) [29]. However, in the case of $GaPO_4$ [30], its ambient α-cristobalite ($C222_1$) phase transforms to *Cmcm* phase *via.* intermediate monoclinic phase under hydrostatic conditions where methanol-ethanol was used as PTM. The intermediate monoclinic phases observed in $AlPO_4$ and $GaPO_4$ are however different. The high pressure structural behaviour of solid solution of α-$AlPO_4$ and α-$GaPO_4$ under different pressure conditions may exhibit new phase with different sequence of transformation.

In this chapter, the high pressure angle dispersive x-ray diffraction studies on α-cristobalite form of $Al_{0.5}Ga_{0.5}PO_4$ have been described under both hydrostatic and non-hydrostatic pressure conditions [31]. These investigations show that the structural stability of the compound under high pressure depends on the degree of non-hydrostatic pressure conditions in the diamond anvil cell. The studies under hydrostatic pressure using neon as PTM, show that ambient orthorhombic $C222_1$ phase transforms to orthorhombic *Cmcm* phase at 4.9 GPa. The weight fractions of high pressure *Cmcm* phase and low pressure $C222_1$ phase are found to be ~93% and 7% respectively at this pressure. The high pressure *Cmcm* phase remains stable up to the highest pressure in the experiment, *i.e.* 19 GPa. In the *Cmcm* phase *Al/Ga* becomes six coordinated with oxygen atom while phosphorous continues to be four coordinated. In contrast to this, under non-hydrostatic pressure conditions (without any pressure transmitting medium), transformation of ambient $C222_1$ phase to *Cmcm* phase has not been observed up to 37.5 GPa. However, a new monoclinic phase $P2_1$ is observed which contains layers of six coordinated Al/Ga ions separated by less dense five coordinated Al/Ga ions. The high pressure behavior of α-$Al_{0.5}Ga_{0.5}PO_4$ is in contrast to the non-hydrostatic pressure behaviours of isoelectronic end members $AlPO_4$ and $GaPO_4$ [28, 30]. The values of bulk modulus for $C222_1$ and *Cmcm* phases are determined to be 19(2) GPa and 126(4) GPa respectively using third order Birch-Murnaghan equation of state [32].

Chapter 4: Preparation and high pressure studies on $InPO_4$

At ambient conditions, $InPO_4$ crystallizes in the orthorhombic *Cmcm* phase. This phase is the high pressure phase of α-cristobalite form of $Al_{0.5}Ga_{0.5}PO_4$, $AlPO_4$ and $GaPO_4$. Due to bigger atomic size of *In* atom compared to Al/Ga, induced internal stresses lead to stabilization of *Cmcm* phase of $InPO_4$ even at ambient conditions. In this phase, *In* becomes six coordinated with respect to the oxygen atoms while phosphorous continues to be four coordinated. In this chapter, the preparation methodology of ambient orthorhombic *Cmcm* phase of $InPO_4$ *via.* solid state reaction and co-precipitation methods are described in detail. For solid state route, analytical reagent grade powders of In_2O_3 and $(NH4)_2HPO_4$ were used as starting reagents and the structure is formed at 950 ^{0}C. However, XRD pattern shows ~ 4% In_2O_3 along with $InPO_4$ which has come from decomposition of $InPO_4$ to In_2O_3. Therefore, to prepare $InPO_4$ at lower temperature, co-precipitation method has also been used.

The experimental high pressure x-ray diffraction and Raman studies on $InPO_4$ show that ambient *Cmcm* phase remains stable upto ~ 10 GPa. On further increase of pressure to ~ 12 GPa, both the zircon (Space Group $I4_1/amd$) and scheelite (Space Group $I4_1/a$) type tetragonal phases are present along with ambient orthorhombic *Cmcm* phase. In both the zircon and scheelite phases, *In* atom becomes eight coordinated with respect to the oxygen atoms while phosphorous continues to be four coordinated. The high pressure tetragonal phases are earlier predicted in theoretical studies [33]. The transformations of Cmcm phase to tetragonal phases are first order in nature. The high pressure phases persist on release of pressure which shows that the phase transition is irreversible. The value of bulk modulus for *Cmcm* phase is also determined to be 97(6) GPa using third order Birch-Murnaghan equation of state.

Chapter 5: High pressure studies on $YInO_3$

Chapter 4 describes the high pressure behavior of six coordinated In^{+3} ion. It is rare for In^{+3} to occupy trigonal bipyramid coordination. The hexagonal $P6_3cm$ phase of $YInO_3$ has layered structure wherein layers of InO_5 trigonal bipyramids are joined by YO_7 polyhedra through common oxygen along *c*- axis [13]. $YInO_3$ was synthesized by a self-assisted gel combustion route [13] in two modifications, cubic and hexagonal. The cubic phase (space group: $Ia\bar{3}$) is low temperature phase and formed at 600 ^{o}C which remains stable up to 17 GPa. On further heating the sample to 1175 ^{o}C, pure hexagonal $YInO_3$ is obtained.

In this chapter, the high pressure angle dispersive X-ray diffraction and Raman scattering studies on hexagonal $P6_3cm$ form of $YInO_3$ have been presented [34]. Its ambient phase shows anisotropic compression behavior, *i.e.* more compression in the *ab* plane compared to the *c*-axis. The experimental studies have shown onset of a first order irreversible phase transition in this compound in the pressure range 12 GPa - 15 GPa. The high pressure phase of $YInO_3$ is found to be orthorhombic with space group *Pnma.* In the orthorhombic phase, the coordination number of In^{3+} ions changes from five to six. Isostructural compounds of $YInO_3$ such as $YMnO_3$ and $TmMnO_3$ also show pressure induced transition to *Pnma* type orthorhombic phase [35, 36]. The fact that ambient and high pressure phases coexist in both Raman and XRD studies suggest that the transition to high pressure phase is of first order in nature. The bulk modulus of hexagonal $P6_3cm$ phase is determined to be 194 ± 10 GPa which matches well with theoretical calculated value.

Chapter 6: Summary and Conclusions

This chapter gives a summary of the main results and the conclusions of the studies reported in the thesis. This thesis describes the diamond anvil cell based high pressure studies on some framework structural compounds, *i.e.* α-$Al_{0.5}Ga_{0.5}PO_4$, $InPO_4$ and $YInO_3$. In all the compounds, the coordination of Group 3A elements with oxygen change under pressure. Under hydrostatic pressure conditions, α-$Al_{0.5}Ga_{0.5}PO_4$ which has four coordinated Al/Ga atoms, transforms to six coordinated Al/Ga. While, under non-hydrostatic a new monoclinic phase $P2_1$ is observed which contains layers of both six and five coordinated Al/Ga. The *Cmcm* phase of InPO4, which has six coordinated *In* atoms, transforms to zircon and scheelite types tetragonal phases (eight coordinated *In*) at ~ 12 GPa. The hexagonal $P6_3cm$ form of $YInO_3$ in which, *In* atoms are in five coordination, shows irreversible phase transition

to orthorhombic *Pnma* phase (six coordinated *In*) in the pressure range of 12 GPa - 15 GPa. The observations of new high pressure phases in these polyhedral materials are of importance to solid state engineering, formation of new materials and understanding of phase transition behavior of some geophysical materials. The results of the thesis may be exploited for exploring the future works on framework structural compounds of Group 3A.

References

1. D. Mondal, V. Srihari, C. Kamal, H. Poswal, A.B. Garg, A. Thamizhavel, S. Banik, A. Chakrabarti, T. Ganguli and S. M. Sharma, *Phys. Rev. B* **95**, 134105 (2017).
2. A. P. Drozdov, M. I. Eremets, I. A. Troyan, V. Ksenofontov, and S. I. Shylin, *Nature* **25**, 73 (2015).
3. K. Umeo, H. Kadomatsu and T. Takabatake, *Phys. Rev. B* **54**, 1194 (1996).
4. W. Zhang, A. R. Oganov, A. F. Goncharov, Q. Zhu, S. E.Boulfelfel, A. O. Lyakhov, E. Stavrou, M. Somayazulu, V. B. Prakapenka, Z. Konopkova, *Science* **342**, 1502 (2013).
5. R. M. Hazen, L. W. Finger, *Comparative Crystal Chemistry. John Wiley & Sons Ltd, New York*, 231(1982).
6. J. F. Huang, W. Yang and L. Cao, *Journal of Materials Science & Technology* **26**, 1021 (2010).
7. Y.N. Pitak, and Y.V. Churilova, *Refractories and Industrial Ceramics* **45**, 275 (2004).
8. J. Haines and O. Cambon, *Z. Kristallogr.* **219**, 314 (2004).
9. J. Haines and O. Cambon, D. Cachau-Herreillat, G. Fraysse and F. E. Mallassagne, *Solid State Science* **6**, 995 (2004).
10. O. Pluchery, J. Eng Jr., R.L. Opila, Y.J. Chabal, *Surf. Sci.* **502**, 75(2002).
11. E. F. Bertaut, E.F. Forrat and P. H. Fang, *C.R.Acad.Sci.Paris* **256**, 1958 (1963).
12. R. Shukla, F. N. Sayed, V. Grover, S. K. Deshpande, Apurav Guleria and A. K. Tyagi, *Inorganic Chemistry* **53**, 10101 (2014).
13. R. Shukla, S. K. Gupta, V. Grover, V. Natarajan and A. K. Tyagi, *Dalton Transactions* **44**, 10628 (2015).
14. D. C. Palmer and L. W. Finger, *American Mineralogist* **79**, 1 (1994).
15. D. C. Palmer, R. J. Hemley, and C. T. Prewitt, *Physics and Chemistry of Minerals* **21**, 481 (1994).
16. A. E. Ringwood and S. E. Kesson, *The Moon* **16**, 425 (1977).
17. A. E. Ringwood, *Geochim. Cosmochim. Acta* **55**, 2083 (1991).
18. N.L. Ross, J. Zhao and R.J. Angel, *Journal of Solid State Chemistry* **177,** 1276 (2004).
19. Nancy L. Ross, *Reviews in Mineralogy and Geochemistry* **41**,257 (2000).
20. R. D. Shannon, *Acta Crystallographica.* **A32**, 751 (1976).
21. K. K. Pandey, H. K. Poswal, A. K. Mishra, A. Dwivedi, R.Vasanthi, N. Garg, and

S. M. Sharma,Pramana *J. Phys*.**80**,607 (2013).

22. A. Jayaraman, *Scientific American ISSN 0036-8733*, **250**, 54 (1984).
23. R. J. Angel, *Reviews in Mineralogy and Geochemistry* **41**, 35 (2000).
24. H. K. Mao, J. Xu, and P. M. Bell, *J. Geophys. Res.* **91**, 4673 (1986).
25. B. E. Warren, *X-ray diffraction (Addison-Wesley, Reading, Massachusetts* (1969).
26. D. Long, *Raman Spectroscopy (McGraw-Hill International Book Company* (1977).
27. A. B. Larson and R. B. Von Dreele, *Los Alamos National Laboratory Report LAUR* **86**, 748 (2000).
28. H. K. Poswal**,** N. Garg, M. Somayazulu, and S. M. Sharma, *American Mineralogist* **98**, 285 (2013).
29. S. Klotz, J. C. Chervin, P. Munsch, G. Le Marchand, *J. Phys. D: Appl. Phys.* **42**, 075413 (2009).
30. L. C. Ming, Y. Nakamoto, S. Endo, C. H. Chio and S.K. Sharma, *Journal of Physics: Condensed Matter* **19**, 425202 (2007).
31. A. Dwivedi, H K Poswal, K K Pandey, H. P. Liermann, C. Murli and M. N. Deo; *High Pressure Research* **39**, 81 (2019).
32. F. Birch, *J. Geophys. Res.*, **83**, 1257 (1978).
33. S L-Moreno and D. Errandonea, *Phys. Rev. B* **86**, 104112 (2012).
34. A. Dwivedi, H. K. Poswal, R. Shukla, Srihari Velaga, B. D. Sahoo, V. Grover and M N Deo; *High Pressure Research* **39**, 17 (2019).
35. P. Gao, Z. Chen, T. A. Tyson, T. Wu, K. H. Ahn, Z. Liu, R. Tappero, S. B. Kim and S. W. Cheong, *Phys. Rev. B: Condens. Matter Mater. Phys.* **83**, 224113 (2011).
36. L. J. Wang, S. M. Feng, J. L. Zhu, Q. Q. Liu, Y. C. Li, X. D. Li, J. Liu and C. Q. Jin, *High Press. Res.* **30**, 258 (2010).

List of Figures

List of Tables

List of Boxes

Contents

Chapter 1: Introduction

1.1 Overview

In this ever developing world, the inventions of new materials gain substantial scientific attention. The arduous search for new materials continues even today for cheaper, faster and more efficient products. The physical and chemical properties of a material are influenced by the thermodynamic variables, in particular, pressure and temperature. Pressure is an important thermodynamic variable, which serves as a versatile tool in materials research. The universe has a wide range of pressure of nearly 62 orders of magnitude, *i.e.* around 10^{-32} atmosphere in the outer space of intergalactic voids to over 10^{30} atmosphere at the centre of a neutron star (Figure 1.1)[1]. Application of pressure of a few GPa results in a volume change as high as 50% or more in the case of soft solids like hydrogen[2] while typically ~ 10% change in volume is observed from ambient temperature to the melting of solid. Increased pressure alters the energy of atomic bonds by forcing atoms closer together in a smaller volume. This leads to increase in the free energy (G) of the system. The change in Gibbs free energy of elements with application of pressure[3] is nearly 10 kJ/mol/GPa which is nearly 100 times more as compared to effect of temperature, *i.e.* 0.1 kJ/mol/^{0}C. As inter atomic distance decreases, the overlap of outer electronic orbital in a material increases. This leads to increase in the energy band widths, shifting of the energy bands with respect to the Fermi energy and shifting of the Fermi level itself to the higher values. Pressure thus serves as a powerful parameter to alter the atomic interactions and chemical bonding.

The molecules of gases are held together by weak van der Waal's forces under ambient conditions. With the application of pressure, the molecules of gases come closer and become solids at very high pressures. The gases such as iodine[4] and oxygen[5] transform to metallic form at higher pressures. Xenon[6] and nitrogen[7] gases become non molecular metal and semiconductor respectively at high pressures. Hydrogen gas has been predicted to become metallic under pressure[8]. Theoretical studies also predict that metallic hydrogen might be a superconductor at room temperature[9]. In recent studies by Dias and Silvera, the formation of metallic hydrogen is claimed at nearly 500 GPa and 5.5 K[10]. However, several authors disagree with the studies of Silvera et al.[11, 12]. Recent studies on H_2S have explored that at 1.5 Mbar and ~ 203 K, it becomes superconductor[13]. Several metal hydrides have been proposed to become superconductor under pressure with high value of critical temperature (T_c)[14]. The compound CaH(6) in which hydrogen forms unusual 'sodalite' cages, shows superconducting behavior at 150 GPa with superconducting critical temperature of 220 K[15]. Recent experimental studies show that at 190 GPa, lanthanum superhydride (LaH_{10}), displays superconductivity nearly at room temperature[16].

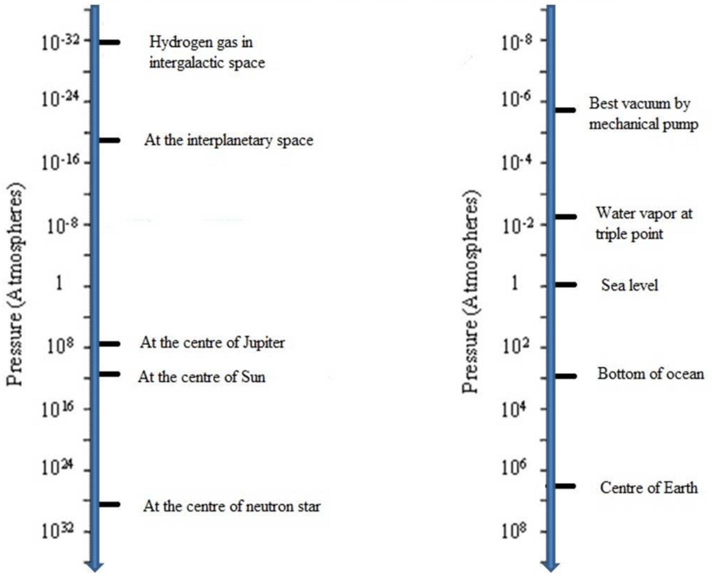

Figure 1.1 Pressure range in the universe.

Pressure can also change the nature of bonding in a material, such as hybridization of orbitals, ionic and covalent nature of bonds etc. For example, graphite which has half of the π bonds (sp^2 hybridization), gets converted into diamond, a super hard material having all σ bonds (sp^3 hybridization) at ~1500 K and 7.5 GPa[17]. Zeng et al. have produced super hard amorphous diamond at high pressure and high temperature[18]. Formation of super hard materials under high pressure is of great interest in many industrial areas such as for making abrasives, polishing tools, cutting equipment and protective coatings. Cubic boron nitride, another super hard material which is ranked second after diamond in hardness, can be produced at 5 GPa and 1500 °C[19].

Application of pressure on different substances can alter the reactivity between them due to change in the ionic radii, electronic structure, chemical affinity, electro negativity and bonding characters. For example, inert gas argon and hydrogen form compound under pressure[20]. Xenon, another inert gas has been found to form compounds with hydrogen with various stoichiometric configurations, such as XeH, $Xe(H_2)_7$ and $Xe(H_2)_8$[21]. The reverse effect of pressure on reactivity, *i.e.* decrease in reactivity with pressure is also possible. For example, reactive molecules H_2 and O_2 become inert with respect to each other[22] under pressure.

Pressure induced phase transformation or amorphization

Minimization of free energy is the deciding factor for a particular crystal structure of a material. As the free energy increases with pressure, the minimum free energy criterion for the parent structure may not be satisfied and the system may transform to another structure. For example alkali metals (Na, K, Rb, Cs) are found in the body centre cubic phase at ambient pressure. But all these metals transform to face centre cubic at various pressures.

However in many of the crystalline solids, the shape of the molecular units may be such that under compression, efficient close packing (to minimize free energy) of atoms is not possible. This may be sterically hindered due to the strong intra-molecular bonding which act within the molecular units[23, 24]. Further closer packing requires modification in the shape of the molecular units through coordination change. As the molecular arrangements are dictated by minimum free energy, the system would try to lower its free energy by sacrificing the translational order to obtain closer packing and the crystalline system therefore transforms to amorphous state[25].

Box 1 Derivative of Gibbs free energy.

$$G = H - TS$$

$$G = U + PV - TS$$

$$dG = dU + PdV + VdP - TdS - SdT$$

$$\left(\frac{\partial G}{\partial P}\right)_T = V$$

$$\left(\frac{\partial G}{\partial T}\right)_P = -S$$

$$\left(\frac{\partial^2 G}{\partial P^2}\right)_T = V\beta$$

$$\left(\frac{\partial^2 G}{\partial T^2}\right)_P = -\frac{Cp}{T}$$

$$\left(\frac{\partial^2 G}{\partial P \partial T}\right)_T = V\alpha$$

The classification of phase transition by Ehrenfest[26] depends on the relation between the thermodynamic quantity and the Gibbs free energy function. According to this, a transition is said to be of first order if the first order derivative of the Gibbs free energy, *i.e.* volume and entropy, shows discontinuity at the transition point. In the second order phase transition, the first order derivative of the Gibbs free energy remains continuous while the second order derivative, *i.e.* specific heat capacity (C_p), coefficient of thermal expansion (α) or compressibility (β), shows discontinuity at the transition point.

1.2 Generation of high pressure: Diamond Anvil Cell

Compression of a material can be brought about either by static methods using different anvil cells, multi anvil apparatus, piston-cylinder systems etc., or by dynamic methods such as shock loading using gas gun, lasers, nuclear methods etc.

	Bar	Atmosphere	kg/cm^2	lb/inch^2
Bar	1	0.9869	1.0197	14.5038
Atmosphere	1.1033	1	1.0332	14.6960
kg/cm^2	0.9807	0.9678	1	14.2234
lb/inch^2	0.0689	0.0680	0.0703	1

1 torr = 1 mm Hg = 1.3332 X 10^{-3} bar

1 Pascal = 1 Newton/m^2

1 GigaPascal = 10^4 bar

Table 1.1 The commonly used units of pressure and their inter-conversion.

The dynamic compression is adiabatic in nature (which causes heating of the specimen), of short time interval and non-hydrostatic. In contrast to this, using static pressure on a material, isothermal and hydrostatic conditions of pressure can be achieved for desired time duration. The static high pressure generating devices can be broadly classified into two categories, *i.e.* piston-cylinder and opposed anvil devices. The basic piston-cylinder apparatus is made of two opposed pistons (generally constructed of tungsten carbide) which presses the sample in a cylinder (generally constructed of high strength steel). Using piston-cylinder, maximum pressure of ~ 10 GPa can be achieved[27]. The opposed anvil devices are evolution of piston-cylinder devices in which pressure on the sample is magnified by massive supported tapered pistons. The pistons with flat tapered tips, known as anvils, reduce the large working stresses quickly to tolerable levels. By applying high enough load on the larger area (loading face) of the anvils, a large stress is generated at the smaller area (working face). The pressure capability of opposed anvil devices depends on the strength of the anvil material. Because of very high strength (bulk modulus of ~ 440 GPa), diamond can be used as anvil to achieve very high pressure. Except infrared absorption band (0.2 to 0.5 eV) and inter-band electronic transitions, diamonds are transparent to most of the electromagnetic radiations extending from the far infrared to x-ray[28-31]. Hence, diamond provides an excellent window for observing the sample in the pressurized state. In addition to this, very small sizes of diamond's anvils make the high pressure cell small, light weighted and portable. Therefore, a sample can be examined by many techniques in the pressurized state. The use of diamond anvil cell (DAC) is the most versatile and established technique for generating static high pressure[32].

In this thesis, I restrict myself to the high pressure study of materials under static pressures using diamond anvil cell. A modified Mao Bell kind of diamond anvil cell (Figure 1.2) for high pressure experiments has been used in this thesis. Pressure can be applied on the sample with the help of a lever arm which works on the principle of a nutcracker. Diamond anvil cell consists of a rocker and a cylinder as backing plates (generally made of hardened steel or tungsten carbide) on which anvils of diamonds are mounted. Before mounting, the top surfaces of the backing plates are polished, as any non-uniformity on the surface may cause the glue to flow between the diamond and the backing plate. The elasticity and adhesivity of the glue can change under pressure and the diamonds may get displaced from the mounted position. Before the application of forces on the diamond's anvils which are mounted on rocker and cylinder, diamonds have to be aligned parallel to each other by using tilt and translation movements of these backing plates. Rocker is provided with screws for tilting, while the cylinder contains screws for translational movements. Initially, translational shift of both the diamonds is corrected by translational movements of cylinder. After that, using tilting of rocker, the culets of both the diamonds are made parallel to each other. Parallelism is judged by minimizing the interference fringes which are formed due to small air gap between the two culets. With the minimization of the interference fringes, it is possible to determine the variation of less than $\lambda/2$ in the thickness of air gap between two culets. For example, a light of wavelength 5000 Å, a single fringe on the diamond culet (diameter of 500 μm) corresponds to an angle between the two culet faces of less than 0.115^0. A zero fringe condition would indicate a perfect alignment of the anvils in the cell.

When the sample is compressed between the culets of diamonds having diameter of ~ 200 to 400 μm, it experiences a large pressure gradient. In addition to this, diamond is a very brittle material, a small shock generated due to collision of the two diamonds may produce crack in the diamond. In order to prevent the breaking of the diamonds and reduction in the pressure gradients inside the sample chamber, a gasket is placed between the anvils. Generally the gaskets are prepared from a metal sheet (made of stainless steel, tungsten or rhenium) which is approximately 200-300 μm thick. In addition to this, the gaskets also serve other important purposes. For example, in X-ray diffraction studies, the gasket of high Z material reduces the background. The gaskets are first pre-indented, *i.e.* sandwiched between the culets of diamonds. Pre-indentation is made for work-hardening of the gasket material which is necessary to stop the failure of gasket in the experiments at high pressure. Pre-indentation also helps in centring the gaskets over the culet. Then a hole is drilled right at the centre of the pre-indented gasket which acts as a sample chamber. Sample, pressure marker and pressure transmitting medium are placed into sample chamber. Typically 50 μm thickness of indented portion and 100 μm hole diameter in tungsten gasket are good enough for achieving a pressure of 50 GPa.

1.3 Pressure transmitting medium

When force is applied on a material, stress is generated on it. The stress at a point can be represented by an infinitesimal small cube (Figure 1.3). Total nine components of stress are needed to describe the stress which can be organized into the matrix form as shown in Figure 1.3. There are three stress components on each of its six faces, *i.e.* one direct or normal stresses (σ_{xx}, σ_{yy}, σ_{zz}) and two shear stresses (σ_{xy}, σ_{xz}, σ_{yx}, σ_{yz}, σ_{zx}, σ_{zy}). If the diagonal normal components of stress are equal and off-diagonal shear stresses are zero, the state of stress is called ‘hydrostatic’.

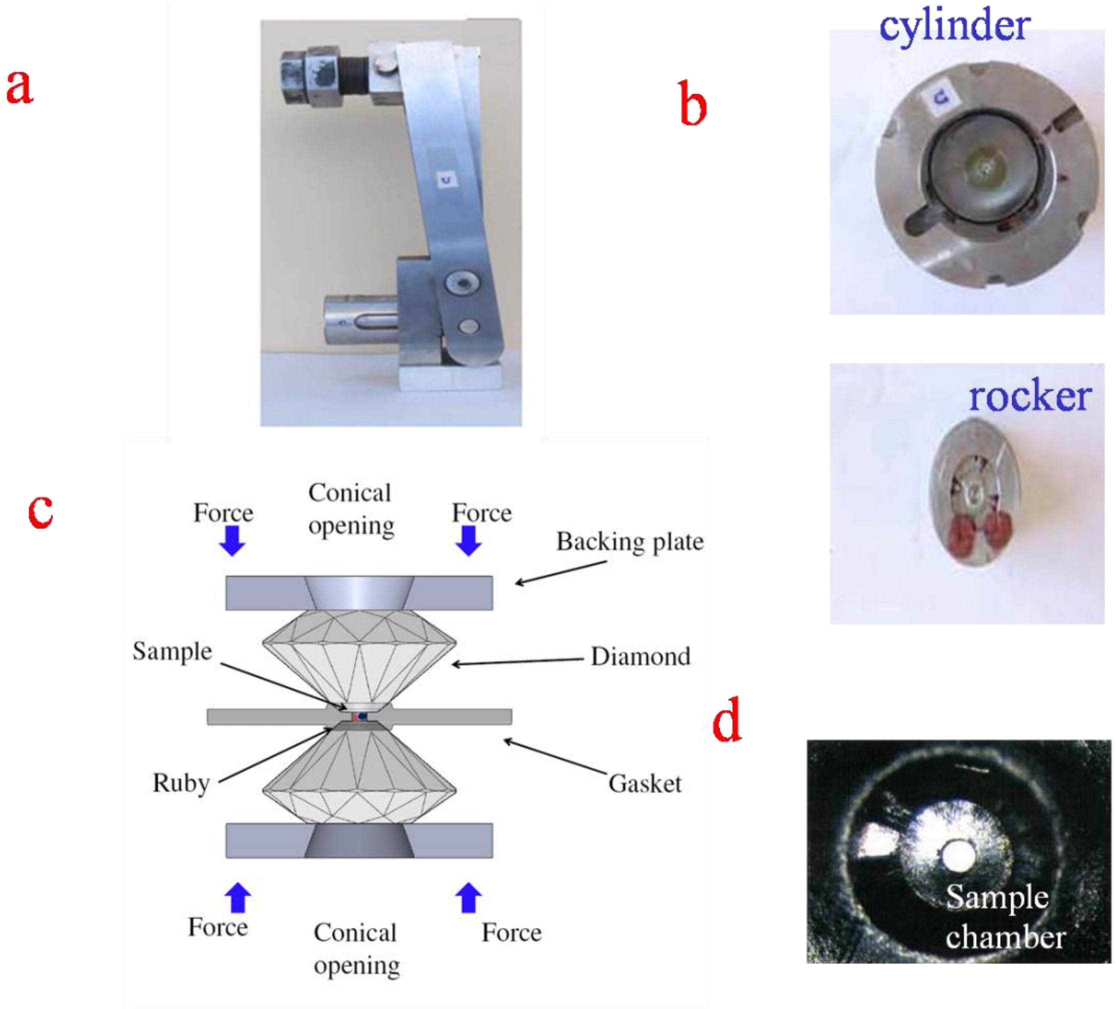

Figure 1.2 (a) Picture of used diamond anvil cell (DAC). (b) Cylinder and rocker backing plates. (c) Working of DAC (d) Sample chamber inside DAC.

The hydrostatic environment (free of any shear or differential stress) plays a vital role in the high pressure experiments. Inhomogeneous strains due to non-hydrostatic stress can generate the broadening of the diffraction peaks which results in the reduction of the signal to noise ratio of the measured diffraction data. Apart from that there can be differences in the evolution of the cell parameters of the crystalline samples under hydrostatic and non-hydrostatic conditions. Non-hydrostatic stresses lead to broadening of Raman modes and thus it can cause to inaccurate determination of peak position of Raman modes. Sometimes non-hydrostatic stresses can change the transition pressure or even can change the phase diagram of a material[33-35]. In order to achieve hydrostatic environment, sample within the pressure chamber is immersed in a medium which displays hydrostatic behavior and does not support any shear stress. The pressure transmitting medium (PTM) should not dissolve or react with the sample. Depending upon the type of experiments, large variety of pressure transmitting medium like soft solids (CsI, NaCl, KBr), condensed gases (neon, argon and helium), mixture of alcohols (ethanol-methanol, ethanol-methanol-water) and silicone oil are used. For high pressure experiments reported in this thesis, neon and methanol-ethanol mixture (4:1) have been used as PTM. Neon provides hydrostatic conditions up to 16 GPa and quasi hydrostatic up to nearly 50 GPa[36]. Methanol-ethanol mixture remains hydrostatic up to its glass transition temperature, *i.e.* 10.4 GPa[36]. Its hydrostatic limit can be increased up to 17 GPa by heating the mixture to 100 ^{0}C[37]. Table 1.2 summarizes the hydrostatic limits of different pressure transmitting mediums.

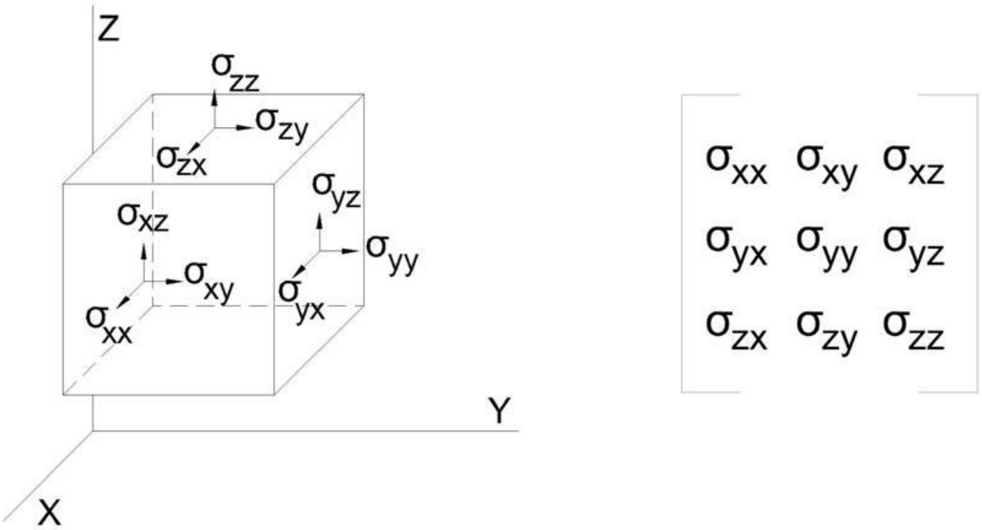

$$\begin{bmatrix} \sigma_{xx} & \sigma_{xy} & \sigma_{xz} \\ \sigma_{yx} & \sigma_{yy} & \sigma_{yz} \\ \sigma_{zx} & \sigma_{zy} & \sigma_{zz} \end{bmatrix}$$

Figure 1.3 Nine components of stress are shown on infinitesimal small cube.

Pressure transmitting medium	Hydrostatic limit (GPa)
Silicon oil	2.5
Methanol : Ethanol (4:1)	10.4
Helium	20
Neon	16
Argon	11
Nitrogen	13

Table 1.2 Hydrostatic limit of different pressure transmitting mediums.

1.4 Measurement of Pressure

Accurate determination of pressure is one of the most important issues in the high pressure experiments. The techniques of measurement of pressure can be broadly classified into two parts, *i.e.* primary or absolute method and secondary method. The primary methods are based on the fundamental equations relating pressure to other physical quantities. The most basic method to determine pressure is to measure force per unit area from loading of a piston of known area by a known weight. However, using this method pressure up to ~ 2.6 GPa can be measured with high accuracy[38]. At higher pressure, the primary scale of pressure can be established using shock wave experiments, where pressure can be determined from the fundamental equations of conservation of momentum and energy[39]. The absolute pressure scale can also be established by measuring elastic constant and density[40] where, formulation does not require shock wave data. The secondary pressure scales are based on the systematic variation of any physical property of a substance with pressure. The secondary pressure scales are calibrated with primary scales. The common methods for measuring pressure inside the DAC are Equation of state (EOS) and Ruby fluorescence. EOS for a number of substances, such as *NaCl, CsCl, KCl, Cu, Ag, Au, Pt, Mo, W, Pd, Al, Pb* are being used for pressure calibration. For high pressure experiments reported in thesis, I have used EOS of gold and ruby fluorescence methods.

Equation of State method

Equation of state (EOS) of a substance is a relation between its pressure, temperature or volume. For practical purposes in the static high pressure experiments, EOS relating pressure and volume at specified temperature is used to determine the pressure. Since, volume can be measured accurately with the aid of X-ray or neutron diffraction.

Theoretically, EOS can be constructed from first principle calculations but their accuracy is not good enough. Therefore, some semi empirical equation of states have been developed which provide reasonably good accuracy. The most common EOS is Birch–Murnaghan[41] which can be derived from theory of finite strain.

Box 2 Birch–Murnaghan Equation of State.

$P = 3/2\, B_0\, x^{-7}\, (1 - x^2)\, [1 + c\, (x^{-2} - 1)]$

Where, $c = 3/4\, (B_0' - 4)$ and $x = (V/V_0)^{1/3}$

Here, B_0 is the bulk modulus at zero pressure, and B_0' is the first order pressure derivative of bulk modulus.

The bulk modulus at constant temperature is defined as

$B_T = -V\, (\delta P/\delta V)_T$

There are several requirements on a substance for use as x- ray pressure marker. It should be chemically stable and non-reactive with the sample as well as pressure transmitting medium in the desired pressure range. For X-ray diffraction studies, a high Z material with cubic structure is preferred as pressure marker. Because of large X-ray scattering factor, small amount of high Z materials can give sufficiently strong diffraction peak. Cubic materials not only have the advantage of fewer peaks which results in the minimum interference with the diffraction pattern of the sample, but also enable one to estimate pressure from a single diffraction peak.

Ruby fluorescence method

Ruby is corundum mineral in which α-Al_2O_3 (alumina) with impurity of Cr^{3+} (~ 0.05%) is present. When Cr^{3+} is introduced in alumina lattice, it substitutes Al^{3+} and the fivefold degeneracy of *3d* electrons of Cr^{3+} is removed by octahedral crystal field. The *U* or *Y* bands absorb the light radiation and populate the metastable ^2E states as shown in Figure 1.4 (a). Ruby is excited by a suitable laser such as Ar-ion, He-Cd or He-Ne. De-excitation of electrons from these metastable ^2E state to the $^4A_2$ ground state, produce two strong luminescence lines at R_1 = 694.25 nm (14404 cm^{-1}) and R_2 = 692.86 nm (14433 cm^{-1}). These two well defined peaks (R_1 and R_2) shift to higher wavelengths with increasing pressure. The shift in R_1 luminescence line of Ruby with pressure is used to determine pressure. The width and the distance between R_1 and R_2 peaks can be used to monitor the hydrostatic pressure conditions inside the high pressure cell[42]. Barnett et al. and Piermarini et al.[43, 44] have calibrated the shift in ruby fluorescence with the Dekker EOS of NaCl up to 19.5 GPa. Later, Mao et al.[45] have extended the ruby pressure scale up to Mbar region under quasi hydrostatic conditions. The shifts are linear up to ~ 30 GPa at the rate of 0.365 nm/GPa. However, above 30 GPa, the scale is non-linear and can be calibrated up to 200 GPa by the relation shown in *Box* 3.

Box 3 Relation between R_1 luminescence line of Ruby with pressure.

$$\mathbf{P = (1904/B)*[\lambda/\lambda_o)^B -1)]}$$

where, P is pressure in GPa

B = 7.665 for quasi-hydrostastic case

= 5 for non-hydrostatic case

λ = Peak wavelength of the ruby R_1 line at high pressure (nm)

λ_o = Peak wavelength of the ruby R_1 line at ambient pressure (nm)

Figure 1.4 (b & c) shows the ruby pressure measurement set-up for our EXCRD beamline at Indus-2 synchrotron. The diode pumped solid state laser of wavelength 532 nm is used to excite the ruby crystal. Two dichroic mirrors are used to deflect the laser towards the 20X objective lens. The lens focuses the laser beam on the sample inside the DAC. The collected signal is analyzed by Maya 2000 (Ocean Optics made) optical spectrograph. The typical ruby fluorescence spectra collected at different pressures are also shown in Figure 1.4 (d).

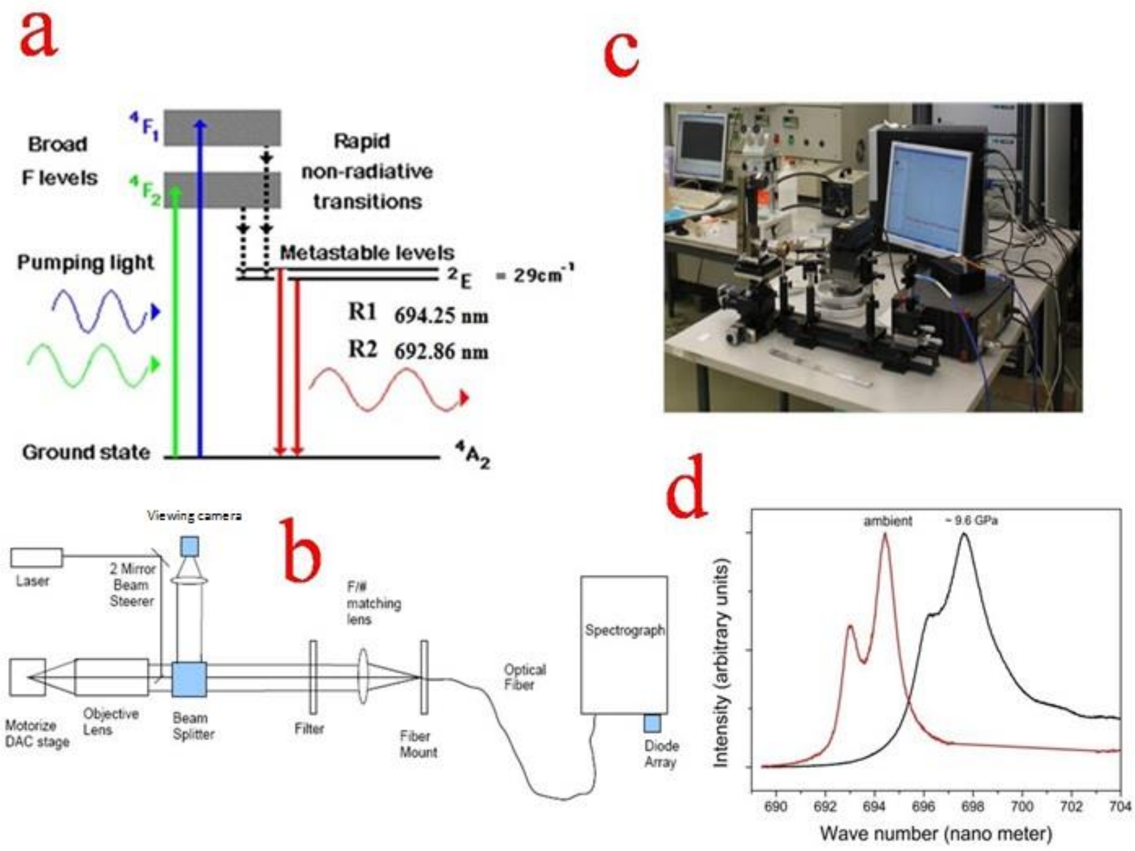

Figure 1.4 (a) Energy levels of Cr^{3+} in ruby. (b) The schematic diagram of ruby setup. (c) Photograph of the ruby setup at BL-11, Indus 2[46]. (d) Collected ruby fluorescence signal.

1.5 Literature survey of high pressure studies on AlPO$_4$, GaPO$_4$ and YAlO$_3$

The framework structures cover a wide range of compounds of importance in the Earth science, condensed matter physics and materials science. These compounds have three-dimensional networks of relatively rigid polyhedral units that share corners with one another. These structures are open and provide enough flexibility to form new denser structures under compression. The forces which act within the polyhedral units are much stronger than the forces that act between them. In general, it is much easier to tilt the polyhedral unit than to distort them[47]. Several polyhedral compounds of Group 3A, such as APO_4 (where, $A = Al, Ga, In$) and its solid solutions, $YAlO_3$ and $YInO_3$ have framework structures. In the following section, I have described the high pressure studies reported in the literature on $AlPO_4$, $GaPO_4$ and $YAlO_3$. These studies form a basis for the high pressure work which is reported in the thesis.

AlPO$_4$ and GaPO$_4$

Aluminium phosphate ($AlPO_4$) and Gallium phosphate ($GaPO_4$) belong to the group of compounds which crystallize with tetrahedral framework. Due to technical importance, geophysical relevance and substantial natural abundance, tetrahedral framework structures have been extensively investigated under high pressure. The structures of $AlPO_4$ and $GaPO_4$ are formed by corner linked AlO_4 or GaO_4 and PO_4 tetrahedra. At ambient conditions, these are crystallized in berlinite type trigonal phase with space group $P3_121$. The berlinite type structures of $AlPO_4$ and $GaPO_4$ are iso-structural to that of α-quartz SiO_2. Their structures can be related to the α-quartz structure by replacing one SiO_4 tetrahedra with AlO_4 or GaO_4 and one with PO_4 thus doubling the c-axis of α-quartz as shown in Figure 1.5. The high pressure behaviour of $AlPO_4$ (berlinite) was claimed to exhibit the memory glass effect[48]. It means that under high pressure, $AlPO_4$ transforms to amorphous phase and with release of pressure, amorphous phase reverts back to the original structure. However, memory glass behaviour in $AlPO_4$ has been disapproved in subsequent studies[49]. $AlPO_4$ (berlinite) and $GaPO_4$ having corner linked tetrahedral network structure at ambient conditions transform to high pressure phase with corner and edge shared polyhedral units (space group *Cmcm*) at nearly 13 GPa and 17 GPa respectively[50, 51].

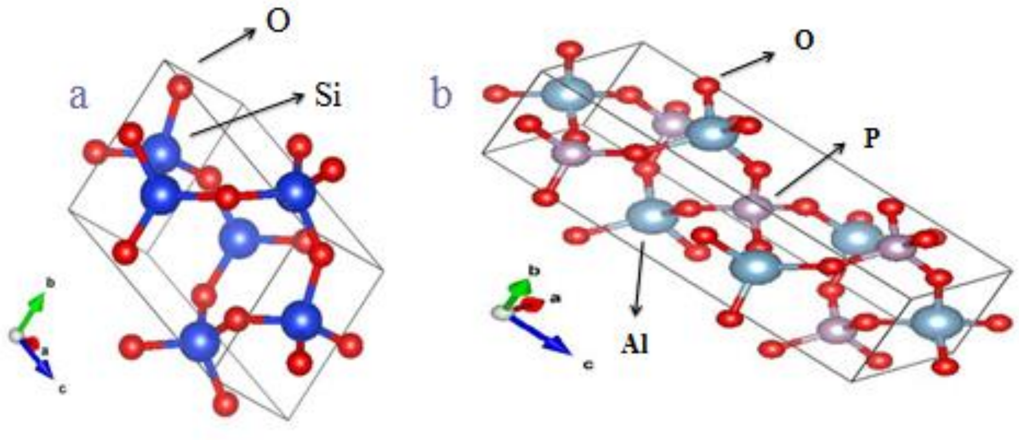

Figure 1.5 Pictorial view of trigonal $P3_121$*phase (a)* SiO_2 *(b)* $AlPO_4$*.*

The high pressure structure consists of octahedral bonded aluminium or Gallium atom while the phosphorus atom remains four coordinated. Porres et al. have reported that on further increase in pressure, the *Cmcm* phase transforms to $CaCl_2$ type monoclinic phase which has six coordinated Aluminium and phosphorus atoms[52]. Until now six coordinated phosphorus has not been observed in $GaPO_4$.

Both $AlPO_4$ and $GaPO_4$ are also found in $C222_1$ type orthorhombic phase. This is the high temperature phase of $AlPO_4$ as well as $GaPO_4$ which remains stable at ambient conditions in meta-stable form. The high pressure studies on $C222_1$ phase of $AlPO_4$ and $GaPO_4$ show that ambient phases of these compounds transform to *Cmcm* phase under high pressure[53, 54].

$YAlO_3$

The compounds having ABO_3 type of structure is known as perovskite. The structure of an ideal perovskite is cubic and formed by BO_6 octahedra wherein *A* cation occupies the larger cuboctahedral (AO_{12}) site. Depending on the tilting and distortion of the BO_6 octahedra, lower symmetry structures such as orthorhombic, tetragonal etc. are obtained from ideal perovskite cubic structure. Action of high pressure on perovskite is a useful method to change their structure and thus useful to explore their properties.

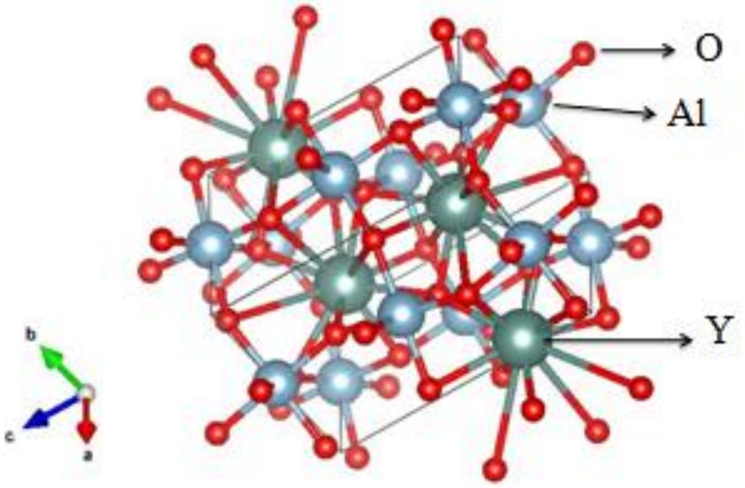

Figure 1.6 Pictorial view of orthorhombic Pnma phase of $YAlO_3$.

$YAlO_3$ is isostructural to $MgSiO_3$ compound which is supposed to form the bulk of the Earth's lower mantle. Apart from geological importance, $YAlO_3$ has various technological applications. For example, doped $YAlO_3$ is a very efficient laser host material. The compound $YAlO_3$ crystallizes in the orthorhombic *Pnma* structure which is made of YO_{12} and AlO_6 polyhedra. High pressure studies show that the compression of the YO_{12} site is anisotropic. The YO_{12} site is composed of four long *Y–O* bonds and eight shorter *Y–O* bonds. The longer *Y–O* bonds are more compressible than the shorter *Y–O* bonds. The compression in AlO_6 site is more than that of YO_{12} site. The tilting of *Al–O–Al* bond decreases with pressure and hence, the structure becomes less distorted with increasing pressure. High pressure behaviour of $YAlO_3$[55] is in contrast to $MgSiO_3$, $CaSnO_3$ etc. in which structural distortion increases with increasing pressure. This contrast high pressure behaviour of $YAlO_3$ can be ascribed to the different compression behaviour of the AO_{12} and BO_6 sites.

1.6 X-ray diffraction

The structural information of a material is important to understand its physical or chemical properties. Diffraction is one of the important methods which can reveal details of the structure at atomic level. These studies can be carried out using X-ray photons, neutrons and electron beams. X-ray is an electromagnetic radiation, which has the wavelengths of photons ranging from 0.1 Å to 100 Å. X-rays are scattered by the electron density cloud surrounding an atomic nucleus, electron beams by the positive potential of the nucleus and neutrons by the nucleus itself. However, electron radiation has significantly less penetrating power than x-rays, and therefore requires very thin specimens and generally used in surface studies. The flux per unit area of third generation x-rays sources is several orders of magnitudes greater than neutron sources. So, for our high pressure experiments, x-rays have been used. The diffraction of x-rays by crystal was first treated by Laue in 1912. An equivalent formalism is given by the W. H. Bragg and W. L. Bragg.

Consider two monochromatic X-ray waves which are scattered from particles in adjacent parallel planes separated by a distance *d* as shown in Figure 1.7. The intensity of the reflected beam at certain angles will be maximum, where the two scattered waves from two different planes have a path difference equal to an integral multiple of the wavelength of X-ray photon, *i.e.* interfere constructively. This combined effect of scattering and interference is called diffraction.

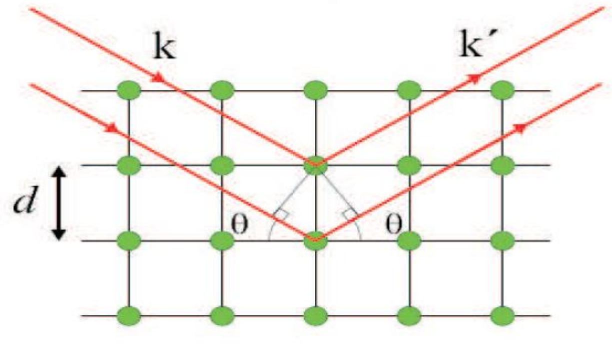

Figure 1.7 Basic principle of X-ray diffraction.

The total path difference between the waves is $2d\sin\theta$. In the case of constructive interference, $2d\sin\theta = n\lambda$ where, n is an integer (n = 1, 2, 3.........). The condition is known as Bragg's law. As from the Bragg's equation $\sin\theta \leq 1$, therefore, $n\lambda \leq 2d$ is necessary condition for diffraction.

For most sets of crystal planes *d* is of the order of 3 Å or less, which means that λ can not exceed about 6 Å. Therefore, a crystal can not possibly diffract ultra violet or larger wave length radiation. On the other hand, if λ is too small, *i.e.* for gamma rays, the diffraction angles are very small to be conveniently measured. Therefore, x-rays are the most suitable probe for diffraction studies of materials. For ambient characterization of the sample, rotating anode X-ray generator (RAG) based X-ray diffraction setup has been used in our laboratory. It contains anode target of Molybdenum which has characteristic line at 0.71069 Å. The characteristic K line from the background of bremsstrahlung radiation is filtered using (002) planes of pyrolytic graphite monochromator. The X-ray diffraction data has been collected on Image Plate area detector (Mar345). The two dimensional diffraction patterns are converted into one-dimension with the help of FIT2D software[56]. The XRD patterns are refined using the Rietveld method[57] using the software package GSAS[58].

1.7 Rietveld refinement

X-ray diffraction data of powdered samples have some limitations. The information from the three dimensional crystal lattice is compressed into one dimension and the reflections from various crystallographic planes overlap. Apart from that the observed XRD peaks are not delta functions. They are broad and may be slightly shifted from the calculated positions. Rietveld refinement is a technique by which the model of a crystal structure can be refined from an experimental powder diffraction pattern.

The intensity of each individual data point *i* is Y_{ic} which can be calculated using the equation:

$$Y_{ic} = Y_{ib} + \sum_{k=k1}^{k2} G_{ik} I_k$$

Y_{ib} is the intensity of the background at point *i* in the pattern.

k1 to k2 are the other reflections contributing to data point *i* in the pattern.

G_{ik} is the peak profile function. This describes how the intensity of the diffraction peak is distributed over a range of 2θ rather than at a single 2θ point. The profile is due to instrument broadening, sample broadening etc. The peak profile function G_{ik} has both the Gaussian and Lorentzian contributions. The variation of Gaussian component with 2θ is given by the following equation[59]:

$$\mathrm{H}_k = \left(U \tan^2\theta + V \tan\theta + W\right)^{1/2}$$

where, H_k is Caglioti function. U, V and W are refinable parameters. While, the Lorentzian component is dependent on 2θ in the following manner, X and Y are refinable parameters :

$$\text{Lorentzian Part} = \left(X \tan\theta + Y/\tan\theta\right)$$

I_K is the intensity of the Bragg's diffraction peak. The intensity of the diffraction peak I_K, can be determined by the following equation:

$$I_K = S\, M_K\, L_K\, |F_K|^2 P_K\, A_K\, E_K$$

- S is an arbitrary scale factor, which used to adjust the relative contribution of individual phases to the overall diffraction pattern.
- M is the multiplicity of the reflection. The observed intensity of diffraction peak at any 2θ position is sum of diffraction from equivalent planes. For example, (001) (100) (010) are equivalent planes in cubic system.
- L is the Lorentz polarization factor.
- P is the modification of intensity due to preferred orientation.
- A is absorption correction.
- E is extinction correction.
- F is the structure factor, which is the amplitude of scattered light due to the crystal structure. Structure factor can be represented by following equation:

$$F_{hkl} = \sum_{j=1}^{N} f_j \exp[2i\pi(hx_j + ky_j + lz_j)$$

where, f_j is atomic scattering factor of atom j and (x_j, y_j, z_j) are its fractional coordinates.

The Rietveld refinement is based on the least square method. It is used to minimize the differences in the observed and calculated intensities of the diffraction pattern by the following equation:

$$Minimization\ factor = \sum_i w_i[y_i\ (observed) - \ y_i(calculated)]^2$$

For the refinement of our high pressure XRD pattern, GSAS program with a graphical user interface ExpGUI[60] has been used. The quality of refinement is judged by visual inspection along with several indications from software, such as R_{wp}, R_F, χ^2.

Box 4 The goodness of fit parameters in ExpGUI program.

$$R_F = \sum_{hkl} |F_{hkl}(\text{obs}) - F_{hkl}(\text{calc})| / \sum_{hkl} |F_{hkl}(\text{obs})|$$

$$R_{wp} = \left\{ \sum_i w_i[y_i(\text{obs}) - y_i(\text{calc})]^2 / \sum_i w_i[\,y_i(\text{obs})]^2 \right\}^{1/2}$$

$$R_{\text{exp}} = \left[(N - P) / \sum_i^N w_i y_i(\text{obs})^2 \right]^{1/2}$$

where, N is the number of observations and P is the number of parameters.

$$\chi^2 = \left(\frac{R_{wp}}{R_{\text{exp}}} \right)^2$$

1.8 Raman scattering

Depending on the bonding and structure, a material can exhibit different kinds of vibrational motions. These vibrational motions of all the atoms in the unit cell may be expressed in terms of the normal modes. The quantized vibrational energy corresponding to each of the normal mode of vibration is called a phonon. During a vibrational motion, there is a change in the charge distribution of the atoms in the unit cell. As a result, interaction of an electromagnetic radiation with various vibrational states of the material can manifest in the form of Raman scattered light, IR absorption spectrum etc. When there is a change in the dipole moment during a vibration, the resultant mode is called infrared active mode. If the vibration changes the polarization of the atoms in the unit cell, the vibrational modes correspond to Raman active mode. Raman scattering is an inelastic scattering. The scattered photons which are observed at higher frequency from the incident frequency ($\upsilon_0 + \upsilon_m$) are known as anti-Stokes while those observed at lower frequency ($\upsilon_0 - \upsilon_m$) are known as Stokes as shown in Figure 1.8 (a). The basic theory of Raman scattering is described in detail by D. A. Long[61].

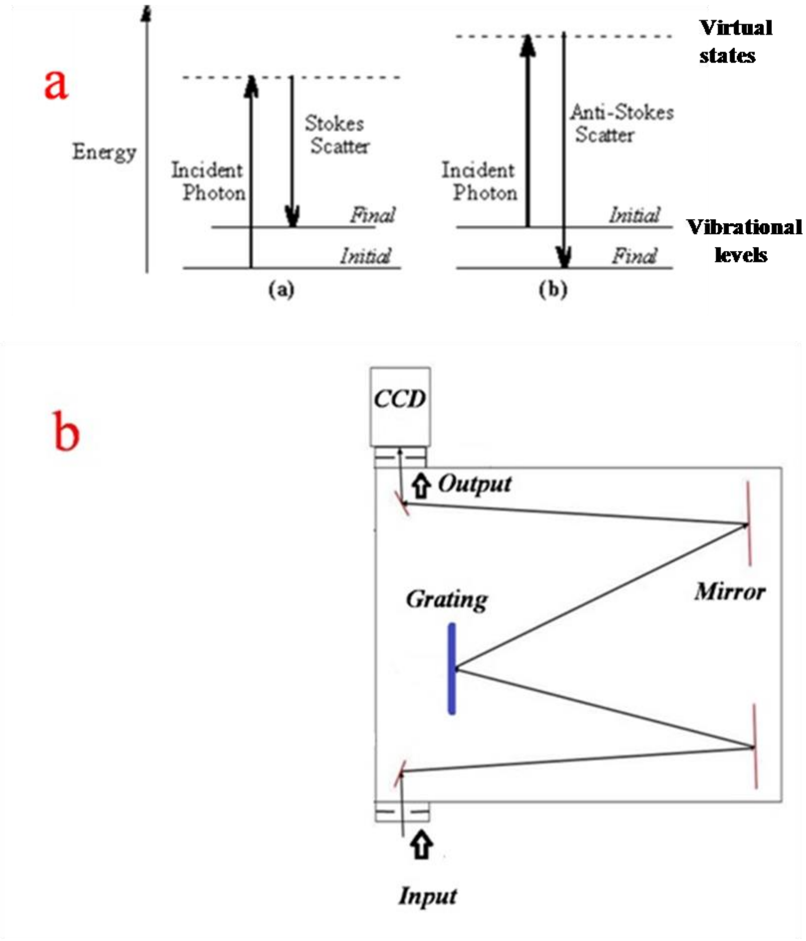

Figure 1.8 a) Basic principle of Raman Scattering. b) Schematic diagram of conventional Raman set up.

Raman scattering method provides the information on the local environment of the atoms and explores the microscopic behaviour of the system which is very useful to study the phase transitions behaviour of materials under pressure. A detail review on Raman scattering under high pressure has been presented by A. F. Goncharov[62]. The schematic diagram of conventional Raman scattering set up is shown in Figure 1.8 (b). The set up may be divided into four parts: laser for excitation of sample, stray light reduction optics (such as rejection filters), collecting optics and detector. The intensity of a Raman peak mainly depends upon polarizability of the material, concentration of active species, intensity and wave length of the source. The spectral resolution of Raman spectra is mainly decided by dispersion power of spectrograph, width of entrance slit and pixel size of CCD detector. The dispersion power of spectrograph depends on focal length of spectrograph, groove density of grating and wavelength of excitation source. The intensity of Raman signal is very weak typically 1 in 10^6 scattered photons. To detect weak Raman signal, it must be separated from the strongly scattered Rayleigh light. Generally, a Rayleigh rejection filter is used to eliminate Rayleigh signal. The filter contains few layers of special dielectric materials. By introducing appropriate thickness of the layers, the condition for destructive interference for the Rayleigh wavelength is being created. Second method to remove Rayleigh line is by using three stages of monochromator. Our Raman spectroscopic measurements were carried out on a Jobin Yvon triple-stage T64000 Raman spectrometer equipped with a Peltier cooled charge-coupled device detector (Synapse) in the backscattering geometry (Figure 1.9). The spectrometer can be operated in additive or subtractive modes. In additive mode each stage disperses the spectrum of the incoming light. The first stage of the monochromator disperses the spectral radiation into separate wavelength components, allowing a specific spectral window to enter the second stage. The second and third stages dispersed the light in the same way and finally the dispersed light is collected on the detector with a lower level of stray light. The resolution in additive mode is better than that of a single stage spectrometer. In the subtractive mode, grating of second stage rotate opposite to the first stage and recombines all the dispersed light from the first stage and focuses it into the entrance slit of the third stage.

The third stage again disperses the light and it is possible to go ~5 cm^{-1} closer to the Rayleigh line.

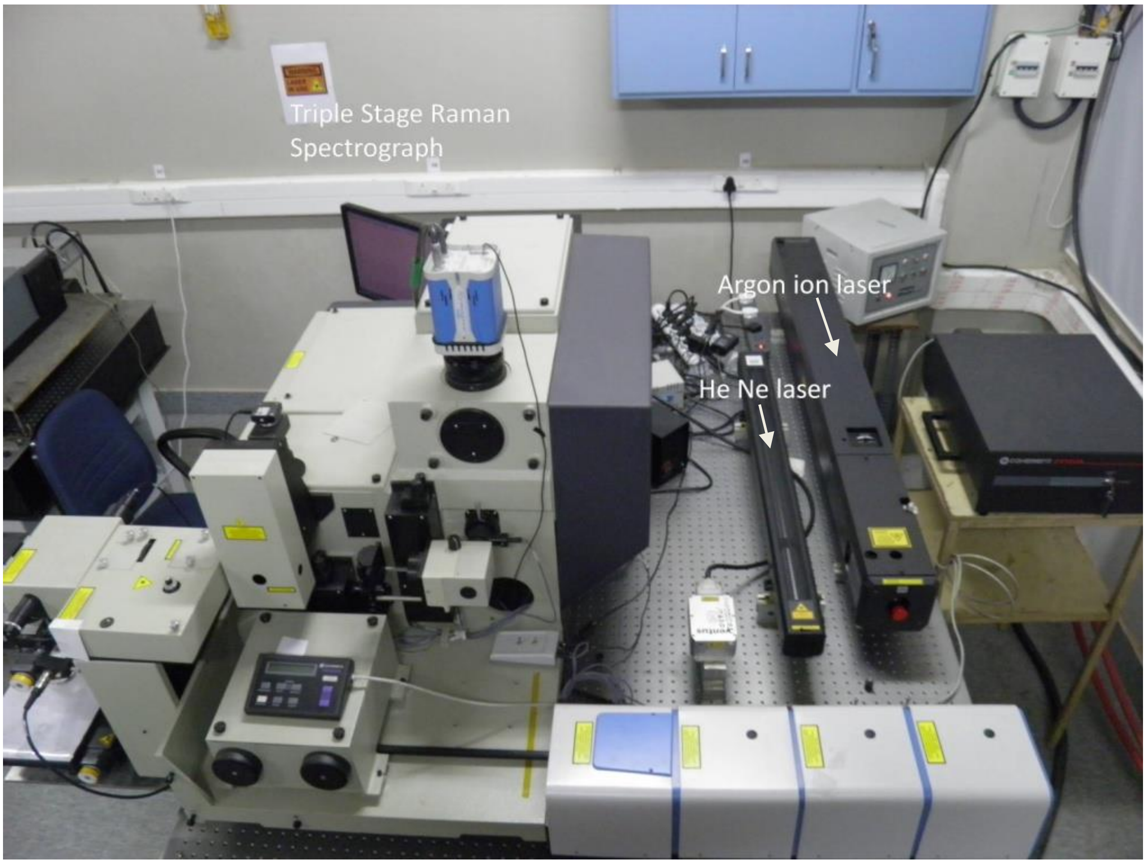

Figure 1.9 Image of Triple stage T64000 Raman spectrometer.

Chapter 2: Extreme Conditions X- ray Diffraction (ECXRD) beamline

2.1 Introduction

As already described in previous chapter, x-rays are the most suited for diffraction studies of materials under high pressure. The sources of x-rays are mainly classified into two categories, *i.e.* conventional generator and synchrotron radiation source. The X-ray diffraction measurements using conventional source, *i.e.* laboratory source has poor resolution and low signal to noise ratio. Due to the high intensity and directionality with synchrotron radiation source, resolution and signal to noise ratio of XRD data can be improved drastically. Therefore, the high pressure diffraction studies presented in the thesis have been carried out at synchrotron radiation source.

Synchrotron is a charge particle accelerator in which electrons or positrons move at relativistic speed along a curved trajectory with a large radius of curvature and the emitted radiation is called synchrotron radiation. The evacuated ring in which charged particle revolves, is called storage ring. Bending magnets are responsible for circulating the charge particle in synchrotron. The radio frequency (RF) system provides energy to the charged particle. This is necessary since the synchrotron radiation (SR) constantly drains the energy of charged particle. Both the magnitude of the magnetic field and the frequency of RF system are synchronized to maintain a charge particle at an orbit of constant radius. Indus-2 is an Indian synchrotron which is designed to operate at 2.5 GeV, 200 mA. It uses dipole magnet of magnetic field 1.5 Tesla to circulate electron. The RF system of ~505.8 MHz is used to energize electron. Important parameters of Indus-2 are shown in Table 2.1[63]. The emitted radiation from Indus-2 contains photons of energies from the infrared to the hard X-ray region. A simulated spectral output of synchrotron radiation emitted by bending magnets (INDUS-2, India) is shown in Figure 2.1. XOP software program has been used for simulation[64].

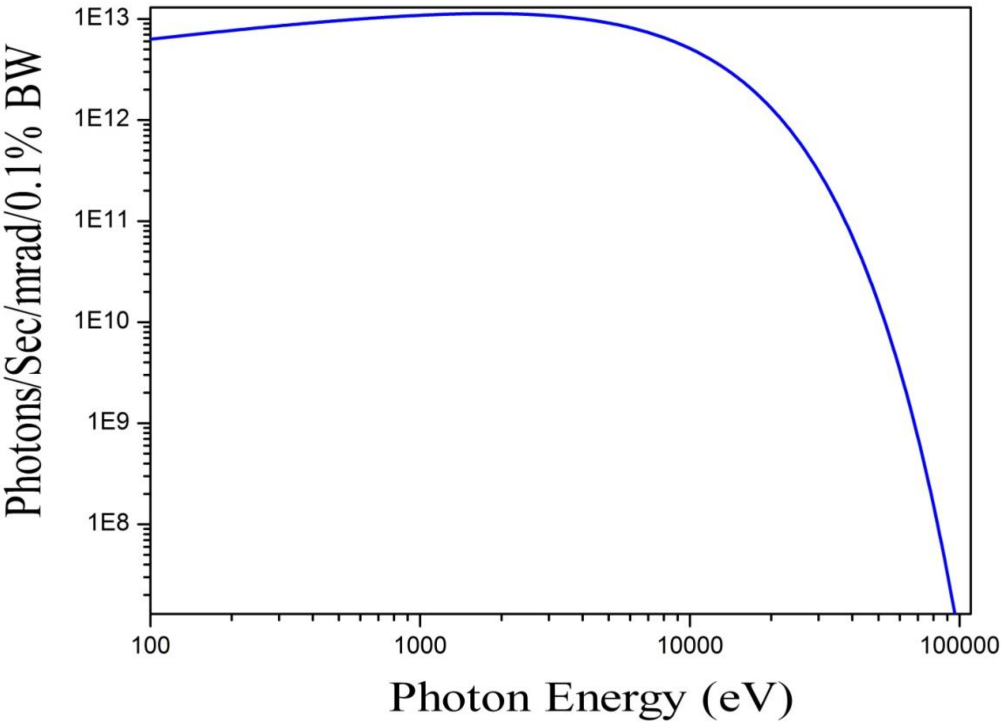

Figure 2.1 Simulated spectrum of emitted radiation from Indus-2.

The intensity of emitted synchrotron radiation is of many orders of magnitudes higher than the conventional lab X-ray source. Relativistic electron, where velocity of electron (v) ~ velocity of the light (c), emits the radiation in a narrow cone in the direction of motion within an angle $1/\gamma$, where, γ is lorentz factor[65]. The Lorentz factor is defined as

$$\gamma = \frac{1}{\sqrt{\left[1 - \left(\frac{v}{c}\right)^2\right]}} = \frac{E}{E_0}$$

The electron beam at Indus-2 has energy (E) 2.5 GeV. The rest mass of electron (E_0) is ~ 0.5 MeV. Therefore, the emitted radiation is collimated into 0.2 milliradian cone (γ = 5000). Because of less divergence, the resolution of XRD patterns is drastically improved than that of lab source. The synchrotron light is linearly polarized in the orbital of plane. The emitted radiation from the bending magnets is in the form of pulses. These pulses have pulse width typically of the order of picosecond and are separated by longer interval, typically of the order of nanosecond. This characteristic of SR may find advantageous in time resolved studies.

Electron energy	2.5 Gev
Critical energy (bending Magnet) at 2.5 GeV	6.24 keV (correspond to critical wavelength 1.986 Å)
Beam emittance-horizontal	5.81E-08 met. rad
Beam emittance-vertical	5.81E-09 met. rad
Dipole magnetic field	1.5 Tesla
Beam life time	24 Hrs
Power loss	186.6 kW
Maximum current	200 mA
Circumference	172.47 met.
Revolution frequency	1.738 MHz
RF frequency	505.812 MHz

Table 2.1 Parameters for Indus-2.

2.2 Description of ECXRD beamline

The emitted radiation from Indus-2 is used in different experimental techniques through appropriate beamlines. Extreme Conditions X-ray Diffraction (ECXRD) beamline is one such beamline which is installed at bending magnet beam port number 11 at Indus-2[66]. This beamline can be operated in two modes, *i.e.* angle dispersive X-ray diffraction (ADXRD) and energy dispersive X-ray diffraction (EDXRD)[67-70]. In the EDXRD variant, white X-ray beam from the bending magnet incidents on the sample, and the diffraction data is collected at a fixed angle (θ). In the ADXRD method, a monochromatic beam of x-rays from a channel cut monochromator falls on the sample and the diffraction pattern is collected as a function of angle (θ). Schematic diagrams of both the modes are shown in Figure 2. 2. Both the techniques have their own merits. The diffraction study at EDXRD mode is advantageous in the case of constrained geometries and depth resolved studies, while ADXRD mode provides diffraction data of high resolution. The detailed comparisons of both the variants are given in Table 2.2.

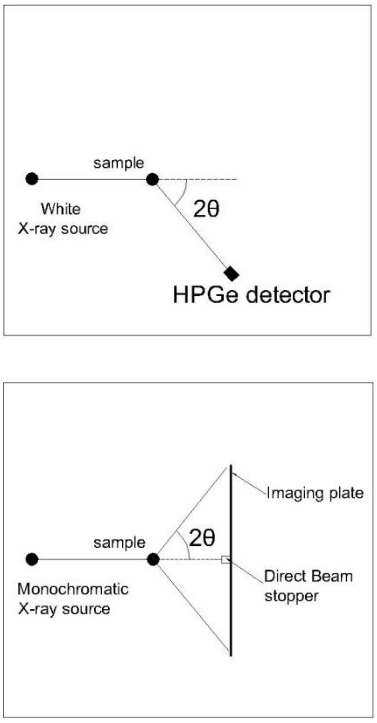

$E_{hkl} = hc/\lambda = hc/2d_{hkl}\sin\theta$ (for n = 1)

where, collection angle (θ) is fixed

Energy dispersive x-ray diffraction

$2d_{hkl}\sin\theta_{hkl} = n\lambda$

where, λ is fixed

Angle dispersive x-ray diffraction

Figure 2.2 ADXRD and EDXRD variants of ECXRD beamline.

The schematic diagram of ECXRD beamline is shown in Figure 2.3[71]. The synchrotron radiation is transported from storage ring to Indus-2 experimental hall, beyond the concrete wall (biological shield) through the front-end optics[72]. The beryllium window (thickness 200 micron) of the front-end of the beamline, delivers white beam of size 1 mrad horizontal beam acceptance. As shown in Figure 2.3, the primary slit system is the first slit system after the front end of the beamline where white beam is delivered. Primary slit system is at ∼16000 mm from the tangent point of the source. As the vertical divergence of synchrotron radiation is 0.2 mrad, the vertical foot print of the beam at the position of primary slit is 3.2 mm. The profile of synchrotron radiation (SR) beam is Gaussian and high energy portion of x-rays are more concentrated in the central region.

	Energy dispersive mode	Angle dispersive mode
Source	Bending Magnet 1.5 Tesla	
Energy range	10-70 keV	Monochromatic tuneable (10 - 30) keV
Angular range for diffraction	± 25°	Depends on sample to detector distance, typically ± 45°
Q Range	1.3 to 15 Å^{-1} (for $2\theta = 25°$)	~ Up to 12 Å^{-1} at 30 keV
Detector resolution	145 eV at 5.9 keV 475 eV at 122 keV	Mar345 area detector having 0.1 x 0.1 mm^2 pixel
Resolution	2% (Geometrical)	4.7 x 10^{-4} @ 17 keV (calculated)
Spot size at sample (with KB mirror focusing)	~ 30 x 30 μm^2	~ 100 x 90 μm^2
Maximum flux at sample	10^{11} photons/sec (100 x 100 μm^2 spot size)	10^{10} photons/sec (1 x 1 mm^2 spot size)

Table 2.2 Comparison of ADXRD and EDXRD variants of ECXRD beamline.

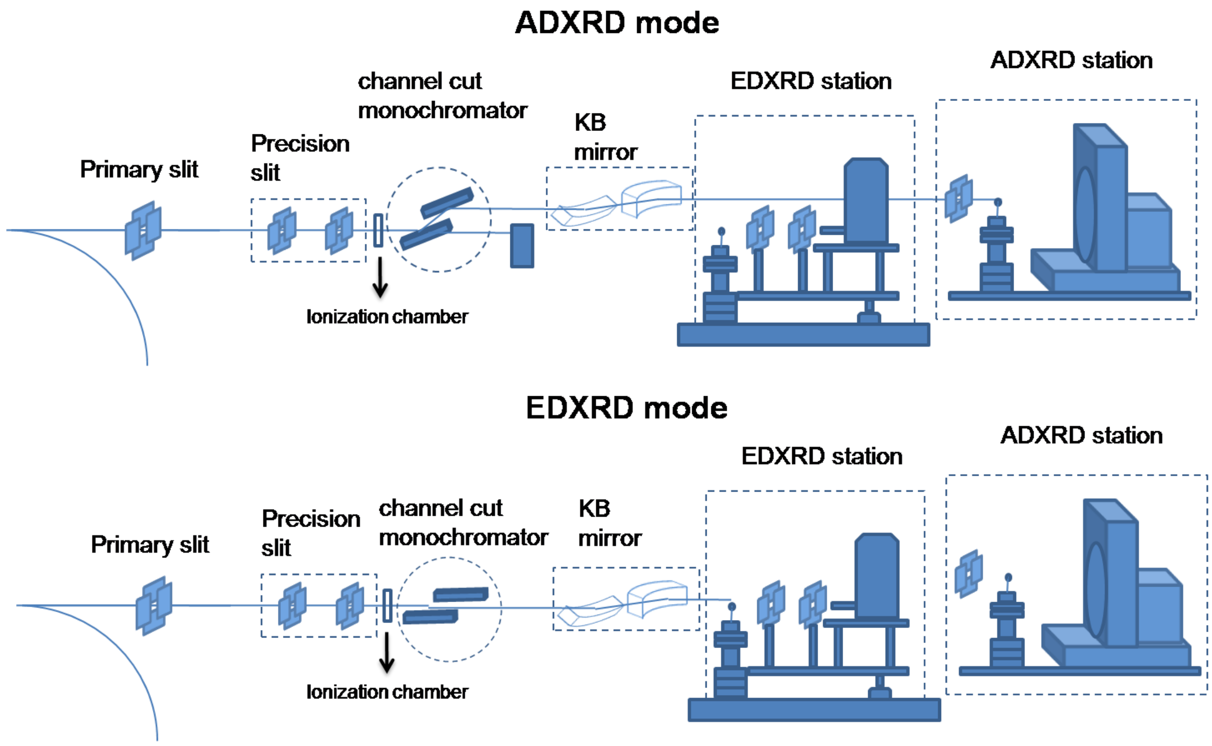

Figure 2.3 Schematic diagram of ECXRD beamline.

The primary slit is used to reduce the synchrotron radiation (SR) beam to a size of 200 µm x 200 µm, such that central region should be selected. The image of installed primary slit system is shown in Figure 2.4 (b). The slit system is made of four water cooled tungsten carbide slits which are housed in an evacuated chamber. The slit system is provided with two view ports. In one view port, a CCD camera has been installed which helps in viewing the slits of the system. The blades of primary slit system are coated with gadolinium oxy-sulphide which fluoresces in X-ray beam and helps in alignment of the slits with respect to SR beam. The movement of the slit system is controlled by four stepper motors. I have assembled the controller for primary slit system. The controller can be communicated with computer through Advantech make PCI 1240 card and the movement of slit system can be controlled by software program. The software program for the movement of its slits was written in visual basic (VB) 6.0[73] software language. VB 6.0 is an object-based, event driven and user friendly programming language which is widely used in graphical user interface

(GUI) applications. Due to high energy of synchrotron radiation, the blades of primary slit system get heated. Hence, it is necessary to monitor the temperature of the slit. To know the on-line temperature of the slits, a software program has been developed using ‘MOD-BUS’ protocol in visual basic 6.0 software language. The software program can communicate with temperature controller (Eurotherm 2416) which senses the temperature of slits through K-type thermocouples. The user interface of software program for primary slit system is shown in Figure 2.4 (a) & (c).

Top Slit Position (mm) 7.124 Temp (°C) 0.0
Bottom Slit Position (mm) 7.120 Temp (°C) 0.0
Left Slit Position (mm) -83.985 Temp (°C) 0.0
Right Slit Position (mm) -95.887 Temp (°C) 0.0
-179.872mm 14.244mm
0.000%

Figure 2.4 a) User interface of software program for Primary slit system. b) Image of slit system. c) Developed temperature measurement program for slit system.

Between the primary slit system and *Be* window of front end, a pneumatic controlled beam stopper (made of 6 mm thick Cu) is installed. After the primary slit, the beam travels in evacuated port (having vacuum ~10^{-7} torr) before the precision slit system for minimizing the beam loss. For achieving vacuum of the order of ~10^{-7} torr, a turbo molecular pump (along with rotary pump) near primary slit assembly has been installed and the pressure is monitored by a universal gauge (containing cold cathode and pirani gauges). A sputter ion pump will be installed at latter stage.

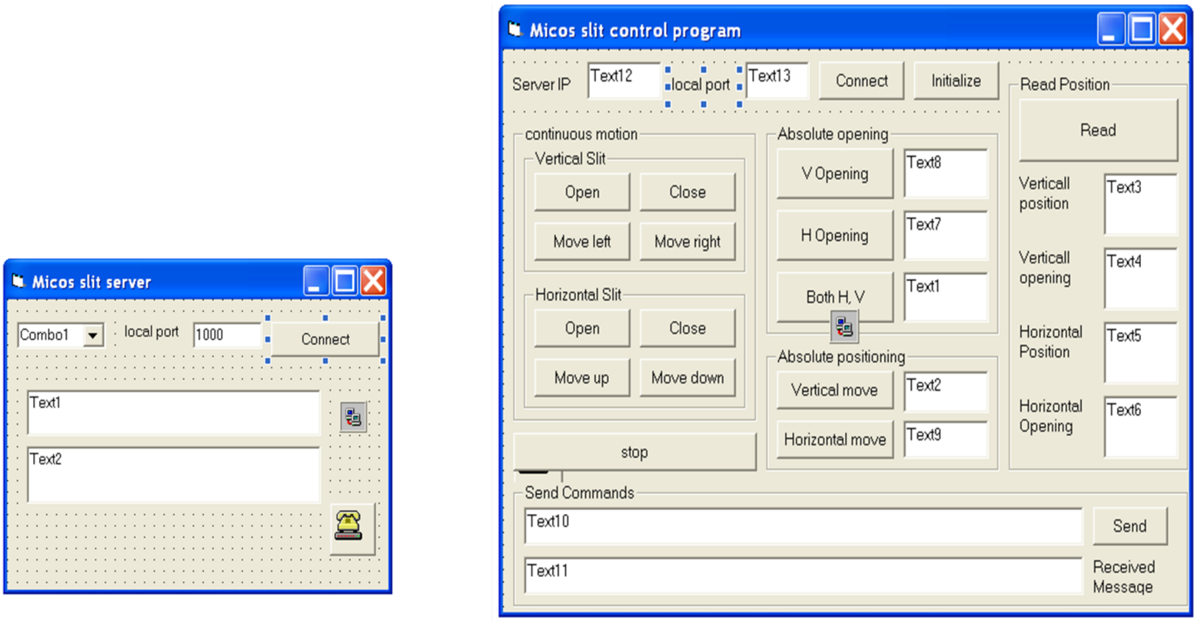

Figure 2.5 User interface of developed software program of precision slit system.

The precision slit system is the second slit system which is used to further reduce the beam size. For high pressure experiments employing diamond anvil cell (DAC)[74], the size of sample chamber is of the order of 100 μm. Therefore, Reduction of beam size to 100 μm is essential for good quality high pressure XRD data. This slit system comprises two separate slit assemblies, whose slits are made of tungsten carbide. The first slit assembly reduces the beam size from 200 μm x 200 μm to 100 μm x 100 μm. The second slit assembly is used to clean the beam diffracted from the edges of the blades of the first slit. The controller for this slit system can control four stepper motors, which are used to drive four slits. Using ‘Winsock’ control, a server-client based software program in Visual Basic 6.0 has been developed to operate the slits in a controlled manner. The user interface of software program is shown in Figure 2.5. The controller can be communicated with computer through RS-232 serial port. The software program can initialize all the four slits at their reference positions. The software program also has the provision to read current position of all the slits. The

'Absolute opening' frame of the software program has the provision for opening the horizontal slit and vertical slit separately as well as simultaneously. Software program can also move all the slits continuously. User can also send the commands by writing them in the text box.

After the precision slit system, an ionization chamber (Oxford make) has been installed for measurement of on-line relative intensity of coming X-ray beam. Air at atmospheric pressure has been used as ionizing medium. The ionization chamber is mounted on lab jack by which height of the ionization chamber can be adjusted. A server-client based software program in VB-6 has been developed to measure the intensity of synchrotron radiation beam. The controller for ionization chamber can be communicated with computer through RS-232 serial port. The user interface of software program is shown in Figure 2.6.

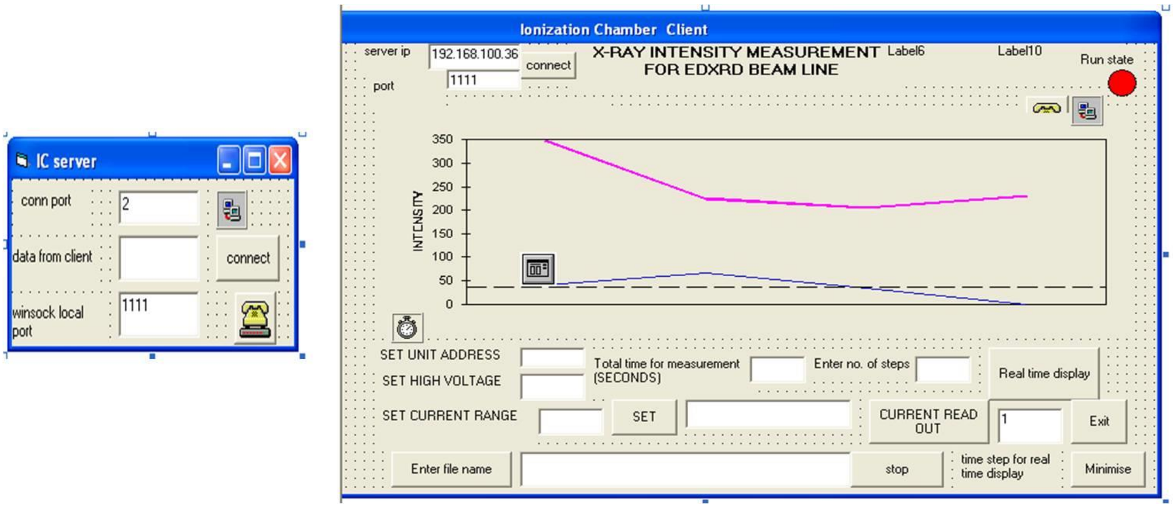

IC server

conn port: 2

winsock local port: 1111

Ionization Chamber Client

server ip: 192.168.100.36

port: 1111

X-RAY INTENSITY MEASUREMENT FOR EDXRD BEAM LINE

time step for real time display: 1

Figure 2.6 User interface of software program of ionization chamber.

The ionization chamber is capable to measure current from 100 fA to 0.1 mA in 6 ranges. User can set different parameters (voltage, current range, unit address) as per requirement. The 'MSChart' utility of VB-6 is used to draw real time graph of current produced in ionization chamber.

After the Ionization chamber, both the EDXRD and ADXRD variants of the beamline have different path for X-ray beam.

Energy dispersive X-ray diffraction (EDXRD) variant

For high pressure DAC based measurements small beam size at sample chamber is essential. If the size of probing X-ray beam is bigger than size of sample chamber, diffraction peaks from gasket material will also be present along with diffraction data of sample. The good quality of high pressure XRD data requires absence of diffraction peaks from gasket material. This can be achieved either by reducing beam size using slits or by focusing the X-ray beam at sample position. First method substantially reduces the flux. Therefore, we have incorporated focussing optics in our ECXRD beamline to collect good quality of high pressure XRD data.

The value of refractive index (n) is less than 1 for X-ray waves and normal refractive optics for focussing does not work. Generally for focussing X-ray waves, mirrors are used which are based on the principle of total external reflection. The refractive index of the material can be expressed in the following equation:

$$n_t = n - i\beta$$

$$n_t = 1 - \delta - i\beta$$

where, δ and β are the optical constants and responsible for the dispersive and absorptive properties of a material[75]. These parameters can be expressed in the following form:

$$\delta = \frac{r_0 Z \rho \lambda^2 N_A}{2piA}$$

$$\beta = \frac{\mu\lambda}{2pi}$$

where, r_0 is the classical electron radius, μ is the absorption coefficient, N_A is Avogadro number, Z is atomic number, A is atomic weight, ρ is mass density and λ is wavelength of X-ray beam. From the Snell's law of total external reflection (Figure 2.7), the real part of the refractive index can be expressed as

$$n = \frac{\sin(90 - \theta_C)}{\mathrm{Sin}(90)}$$

$$1 - \delta = \cos(\Theta_C)$$

Since δ<<1, the cos(θ_C) term can be expressed up to second order .

$$\Theta_C = \sqrt{(2\delta)}$$

For practical purposes, the critical angle (θ_C) of total external reflection in mirror can be expressed in the following way:

$$\Theta_C = 2.33\lambda(\text{Å})\sqrt{(Z\rho/A)}$$

Therefore, a material with high mass density ρ has higher value of critical angle. In case of our beamline, the focusing of the X-ray beam is done by the Kirkpatrick Baez (KB) mirror system[76]. Our KB mirror system consists of two separate mirrors which provide aberration free focusing on both horizontal and vertical directions. The mirrors are made from coating of Pt on Si substrate. Since, Pt has high electron density; coating of mirror with Pt provides large critical angle. The specification of the mirror system is shown in Table 2.3. The bendable mechanism of KB mirror system provides freedom of choosing focal plane. The schematic representation of KB mirror system is shown in Figure 2.7. The focussed beam spot size from the KB mirror system for EDXRD variant is ~ 30 µm X 30 µm. The focused beam falls on the sample which would sit on the 8-axes goniometer.

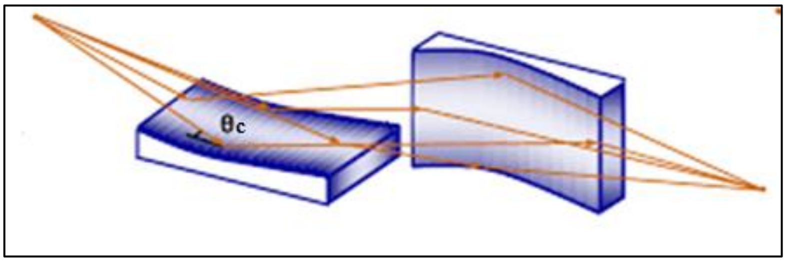

Figure 2.7 The schematic representation of KB mirror system.

Goniometer has provision for eight movements, *i.e.* two bottom *X* and *Y* translational motions, three *x, y, z* translational movements for sample stage, one θ stage for rotating the sample along z axis, one χ (chi) stage for rotating the sample along x axis and one 2θ stage for rotating detector arm. The image of goniometer is shown in Figure 2.8. The resolutions for linear and rotational axes are less than 1 micron and 0.005^0 respectively. The motorized stages have also encoders for the precise movement of the stages.

Mirror	**Horizontal focusing**	**Vertical focusing**
Length (mm)	250	250
Width (mm)	20	20
Incident angle (mrad)	1	1
Acceptance (micron)	250	250
Semi-major-axis of ellipse a (mm)	8880	8880
Semi-minor-axis of ellipse b (mm)	3.5945	2.9377
Slope error	< 1 micro radian	
Surface roughness	< 3 Å	

Table 2.3 Specification of the KB mirror system.

To describe the collection angle of scattered radiation, two slit system whose blades are made of tungsten are installed before detector on the 2θ arm of the goniometer. The pictorial view of installed collection slits is shown in Figure 2.8. I have developed a server-client based software program in Visual Basic 6.0 for collection slit assembly (made of JJ x-ray, Denmark). This slit system is controlled by computer through 'CAN-BUS' protocol. The controller for this slit system can drive four stepper motors. The motion of all the four slits of this slit system is governed by these stepper motors. The desired opening of the slits can be achieved by the software program. The software program has provision to move the slit at the reference position. The user interface of the software program is shown in Figure 2.9 (b & c).

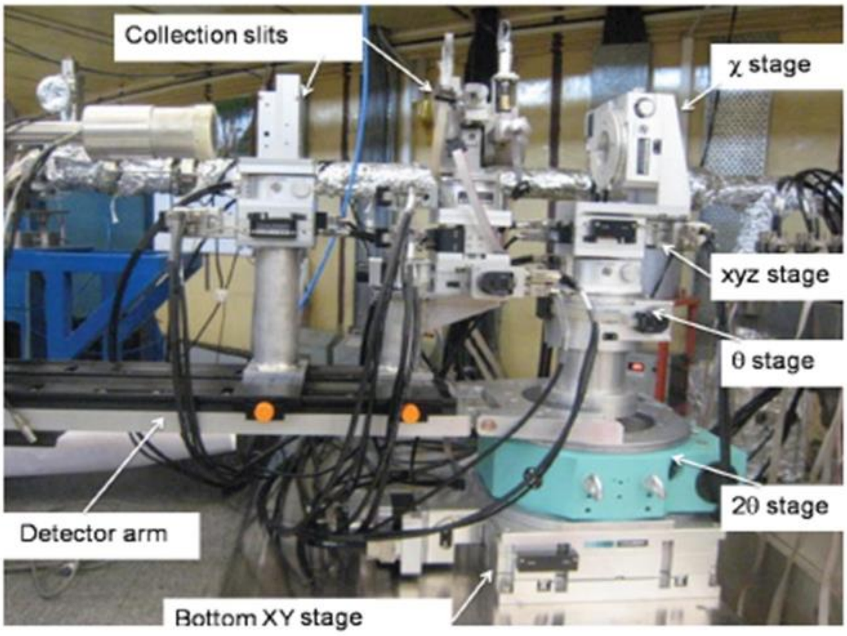

Figure 2.8 The image of goniometer installed at ECXRD beamline.

The scattered radiation from the sample is analyzed by energy sensitive high purity germanium (HPGe) detector (Canberra made model number GL0110). The detector is installed on the 2θ arm of the goniometer. For calibration of HPGe detector, Am-241 radiation source was used.

The resolution of the diffraction peak is defined as ratio of FWHM (full width half maximum) of the peak to the energy of the photon. In energy dispersive X-ray diffraction, the FWHM of diffraction peak depends on following factors:

- The resolution of the detector (ΔE_{ssd}).
- Spread in angle ($\Delta\theta$), due to the finite opening of the slits.
- Spread in the lattice parameters (Δd_l), due to pressure broadening.
- Spread in the lattice parameters (Δd_s), due to symmetrical strain broadening.
- Broadening due to particle size (Δd_p).

Thus net FWHM of the diffraction peak is given as

$$(\Delta E_{net)})^2 = (\Delta E_{ssd)})^2 + (E \cot\theta \, \Delta\theta)^2 + (E/d)^2 . [\, \Delta d_l{}^2 + \Delta d_s{}^2 + \Delta d_p{}^2]$$

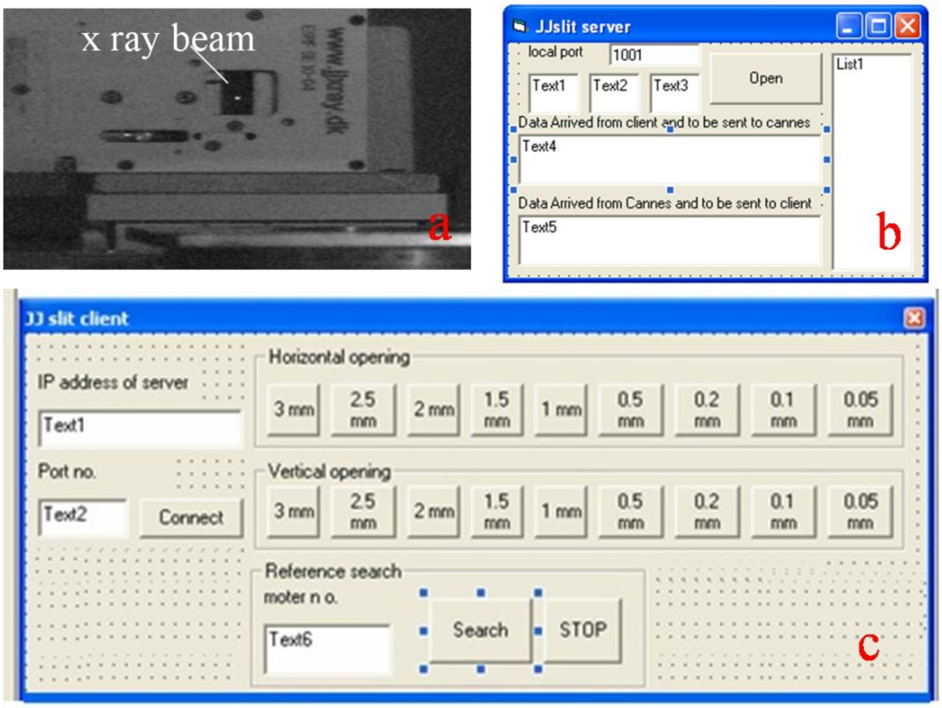

Figure 2.9 a) X-ray beam at collection slit. b) Server side user interface of software program. c) Client side user interface of software program.

The resolution of detector is the deciding factor for overall resolution of the diffraction peak in EDXRD variant. Our HPGe detector has resolution ≤ 130 eV FWHM @ 5.9 keV and ≤ 475 eV FWHM @ 122 keV. The pictorial view of EDXRD variant is shown in Fig. 2.10 (a).

Angle dispersive X-ray diffraction (ADXRD) variant

For ADXRD mode, selection of a particular energy from the synchrotron radiation beam is essential. This can be achieved by diffracting the white beam from appropriate crystal. The crystal should have following properties

- The crystals must be mechanically strong.
- The crystals should have suitable interplanar distances (d), so that the desired energy can be obtained.

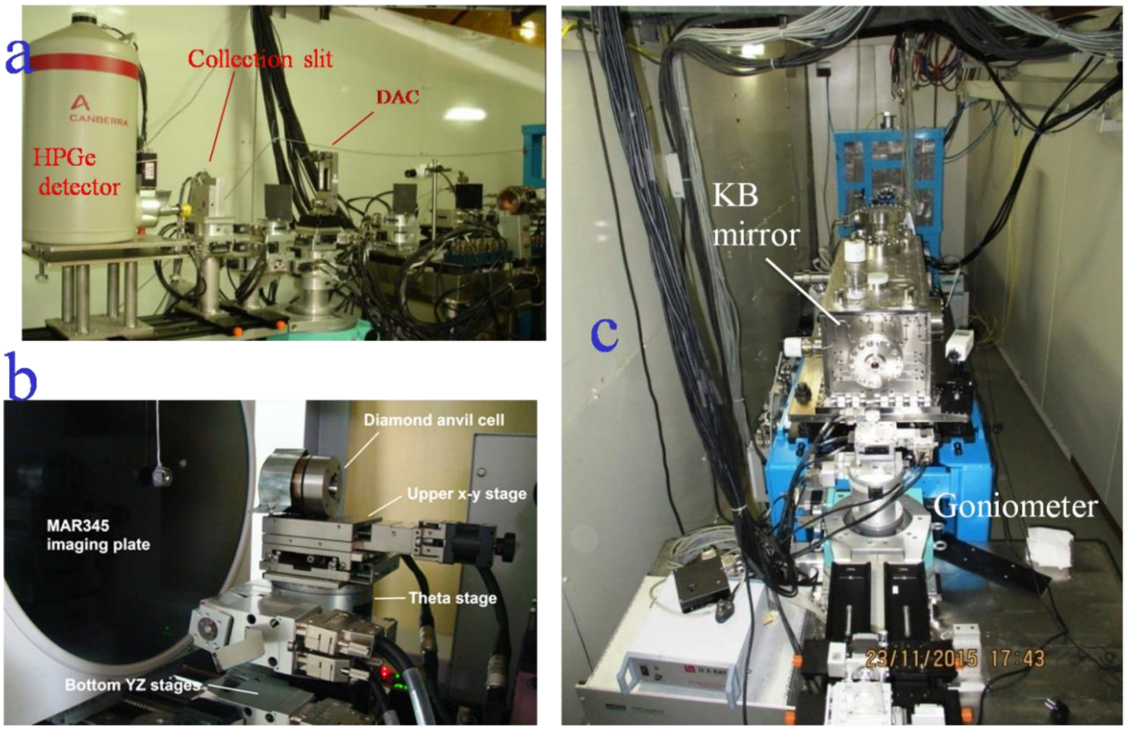

Figure 2.10 a) Image of EDXRD variant. b) Image of ADXRD variant. c) Beamline-11 shielding hutch.

- The structure factor corresponding to the interplanar spacing (d) must be as large as possible. This is required for intense reflection.
- The mosaicity of the crystal must be of suitable magnitude.
- The absorption of the material should be low.
- The crystals should have a small coefficient of thermal expansion so that the wavelength is essentially unaffected by any fluctuations in ambient temperature.

Silicon is the ideal material which fulfils the above requirements. Silicon crystal has cubic structure with a unit cell size equal to 5.4309 Å. The largest d spacing is from the (111) plane, *i.e.* 3.136 Å. Since, Si (111) has higher reflectivity compared to Si (220) with reasonable good resolution. Therefore, we have installed Si (111) channel cut monochromator after the ionization chamber to monochromatize the white beam in ECXRD beamline. The channel cut monochromator provides easy switchability between the two variants (EDXRD and ADXRD) of the beamline. The monochromator is mounted on motorized χ rotation stage and the energy of monochromatic x-rays can be selected by rotating the χ stage to appropriate angle. The image of installed channel cut monochromator is shown in Figure 2.11. The channel cut monochromator has the advantage over single crystal monochromator that shift in X-ray beam can be minimized for a selected energy range. However, there is a small loss in the intensity due to double reflections. In used channel cut monochromator, the length of the crystal is ~ 140 mm and gap between the crystals is ~5mm. With this optimum size, the vertical shift of the beam for energy 8 keV to 30 keV is within ~ 250 micron. This can be easily managed with the motorized stages of detector. The monochromatic beam is further focused by KB mirror system. The focussed beam spot size from the KB mirror system is ~ 100 µm X 90 µm in ADXRD variant. The focused beam is colliminated by a pair of slits before falling on the sample. The sample stage consists five types of motions (*X, Y, x, y,* and *z)* as shown in Figure 2.10 (b). The diffraction data from the sample is collected on area detector (MAR345). Due to absence of energy sensitive detector, the resolution in ADXRD mode is better than that of EDXRD mode. In angle dispersive X-ray diffraction, the overall resolution of diffraction peak depends on geometrical resolution of the setup and spectral resolution of X-ray beam. Geometrical resolution depends upon the pixel size of area detector (*i.e.* 100 µm X 100 µm in our Mar345 detector), slit size used before detector and sample to detector distance. It can be improved by increasing the sample to detector distance. However, with increase in sample to detector distance, the intensity of diffraction data decreases. The geometrical resolution can be expressed by the following equation:

$$\frac{\Delta\lambda}{\lambda} = \Delta\Theta_{\mathrm{B}} \cot \Theta_{\mathrm{B}}$$

where, θ_B is the Bragg's angle of diffraction.

The spectral resolution of X-ray beam depends on the divergence of SR beam (δ_{SR}) and Darwin width of the crystal (ω_D). The spectral resolution can be expressed by following equation:

$$\frac{\Delta\lambda}{\lambda} = (\delta_{SR} + \omega_{\mathrm{D}}) \cot \Theta_{\mathrm{B}}$$

Resolution of the diffracted pattern can be improved by reducing the divergence of SR beam (δ_{SR}). This can be achieved by reducing the slit width. However, reduction in slit width will reduce intensity of SR beam.

According to dynamical diffraction theory, a finite width called Darwin width (ω_D), is presented even for a perfect crystal. This arises due to the multiple diffraction from the finite size crystal. Analytical formula of the Darwin width[77] is given by the dynamical theory of diffraction as shown below:

$$\omega_D = 2.12 \frac{\left(\frac{e^2}{mc^2}\right) N\lambda^2 |F|}{\pi \operatorname{Sin} 2\theta} \frac{(1 + \cos 2\theta)}{2}$$

where, N is the number of atoms per unit cell, e & m are the charge and mass of electron respectively, 2θ is the diffraction angle and F is the structure factor.

The Darwin width is smaller for the material having smaller structure factor. This can be ascribed due to participation of more number of planes in the diffraction. However, with smaller structure factor the intensity of diffraction peaks reduce. The Darwin width is smaller for high energy X-ray beam. However, the cot θ_B term in spectral resolution increases with energy.

2.3 Shielding of beamline

Due to high radiation field, all the components of the beamline should be properly radiation shielded. Mainly three types of radiation hazards can occur, *i.e.* exposure to x-ray, neutron or ozone.

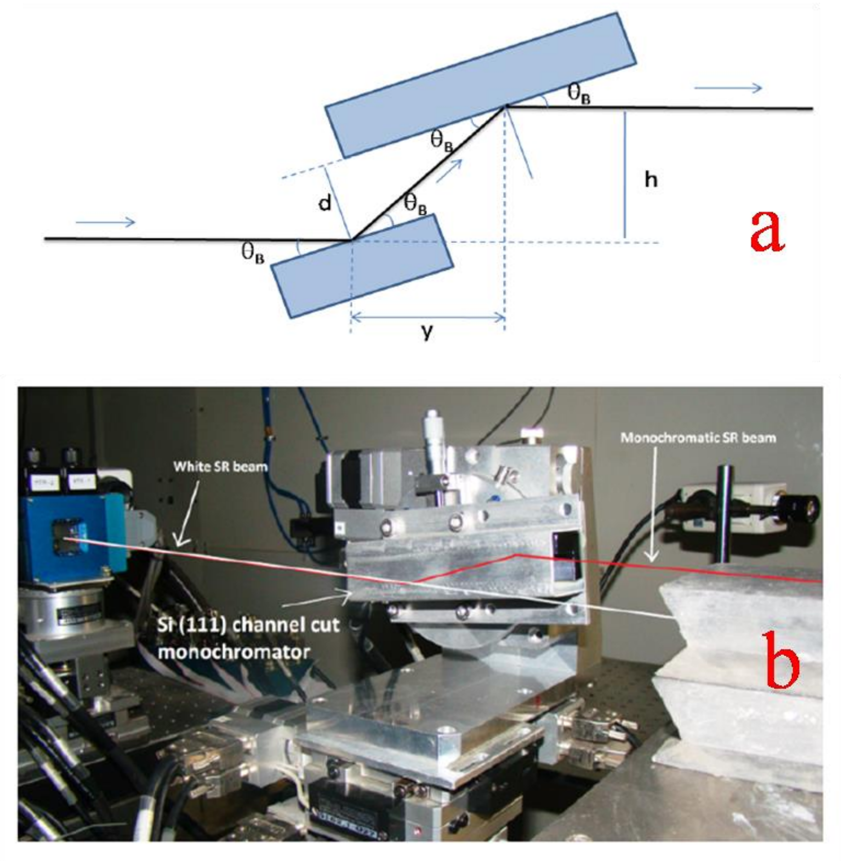

Figure 2.11 a) Schematic diagram of channel cut monochromator. b) Image of Si (111) channel cut monochromator installed at ECXRD beamline, Indus-2.

Further exposure to X-ray radiation can be classified into two categories, *i.e.* due to synchrotron radiation (SR) and bremsstrahlung radiation (BR). Beyond 25 keV, the intensity of SR reduces drastically (Figure 2.1).To prevent the exposure from SR, the whole ECXRD beamline is enclosed in a shielding hutch which is made of *Pb* (thickness 3 mm) sandwiched between *MS* plates (thickness 1.5 mm)[78]. The image of the shielding hutch is shown in Figure 2.10 (c). The door of shielding hutch is interlocked with the synchrotron radiation detector and can not be opened if the radiation level is higher than the allowed permissible level. Bremsstrahlung radiation (BR) is produced when the accelerated charged particles interacted with the matter. The energy of BR ranges from few keV to the maximum energy of electrons (*i.e.* 2.5 GeV). The BR radiation is mostly limited in the forward direction within 15^0 cone with vertex at scattering point. Most of the BR is stopped by 1.5 meter thick concrete wall around the synchrotron ring. However, it can leak from the opening provided for the SR. For the prevention of BR, two local shielding are provided inside the shielding hutch. First shielding of *Pb* blocks, having dimension 100 mm (thickness) x 600 mm x 600 mm, is incorporated near the primary slit system which is first scattering component of the beamline. Second shielding of 100 mm thick *Pb* blocks (area 1000 x 1000 mm^2) is placed at the end of beamline[78].

Ozone gas can be formed when the radiation reacts with oxygen in air. To minimize the ozone concentration, a blower has been incorporated in the shielding hutch of the beamline. Neutrons can also be produced when the BR is stopped by some solid component of the beamline. However the equivalent neutron dose is ~ 10^{-13} mrem/hour. Hence, no separate shielding is required for that. The neutron bags are continuously being used to measure the dose.

2.4 Alignment of the sample

Due to high radiation, all the components of our ECXRD beamline are placed inside the shielding hutch and are remotely controlled. The sample should be aligned in the path of X-ray beam to collect good quality of XRD pattern. In manual alignment process, a fluorescent screen or X-ray camera is placed after the sample and the sample is aligned by visually observing the image. I have developed software programs in VB 6.0 software language to align the sample in the ambient and high pressure conditions.

Sample alignment at ambient conditions

The intensity of incoming synchrotron radiation beam can be measured with the help of X-ray photo diode. When SR beam falls on the photodiode, a current signal is generated. Using picoammeter (Keithley make), this current signal can be measured. A server-client based software program was developed using ‘Winsock’ control for measuring online current value of photodiode. The picoammeter is connected to computer by general purpose interface bus

(GPIB) card. By connecting the server to picoammeter, it is initialized and the server becomes ready to listen client at the mentioned port number. The software program has the provision for displaying the value of picoammeter's current in real time for desired time step. By monitoring the current value, user can align the sample in the path of X-ray beam which is mounted on the computer controlled motorized stages.

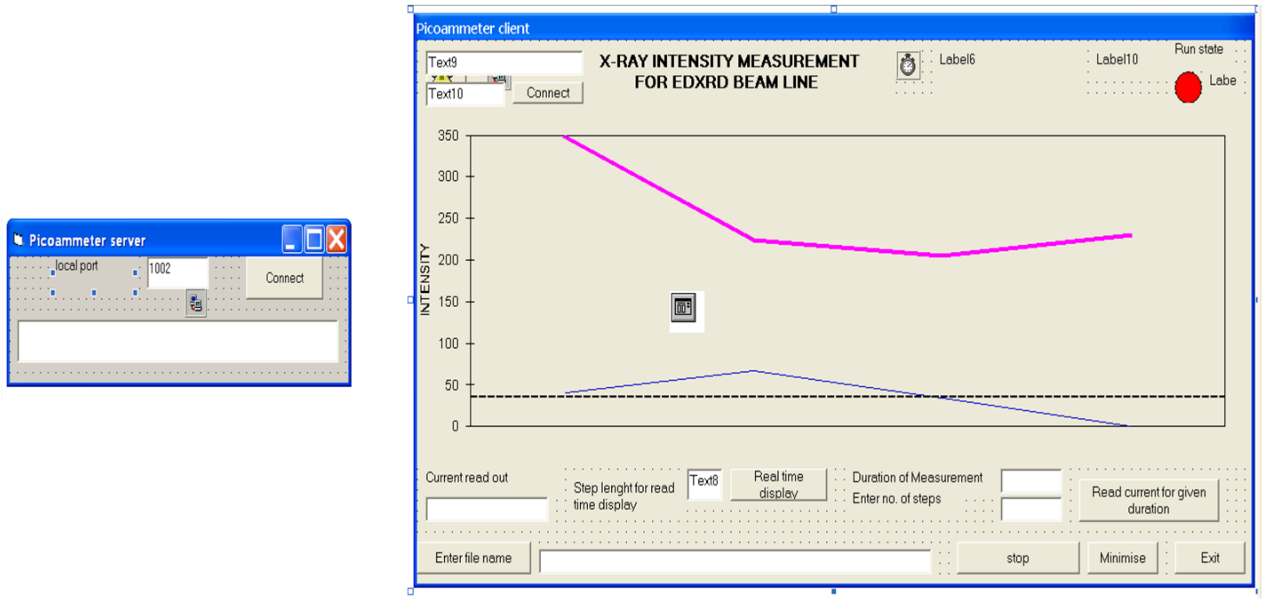

Figure 2.12 User interface of software program for measuring the photo diode current by picoammeter.

Sample alignment at high pressure inside DAC

The use of diamond anvil cell (DAC) is the most versatile and well established technique for generating static high pressure. The typical diameter of sample chamber of DAC is less than 100 μm. The manual alignment process of sample inside DAC in the path of X-ray beam is cumbersome and time consuming. In addition to this, in case of manual alignment, the sample may not be placed in the vicinity of the most intense position of X-ray beam. This results in poor X-ray diffraction signal and hence the manual alignment of DAC needs to be automated. The alignment process of DAC is automated by developing a 'Scanning Program' in Microsoft Visual Basic 6.0 software language. The automation process involves goniometer sample stages (Huber make), picoammeter (Keithley make) and silicon X-ray photo diode. The functional layout of different hardware components is shown in Figure 2.13 (a). The flow of instructions of ‘Scanning Program’ is shown in Figure 2.13 (b).

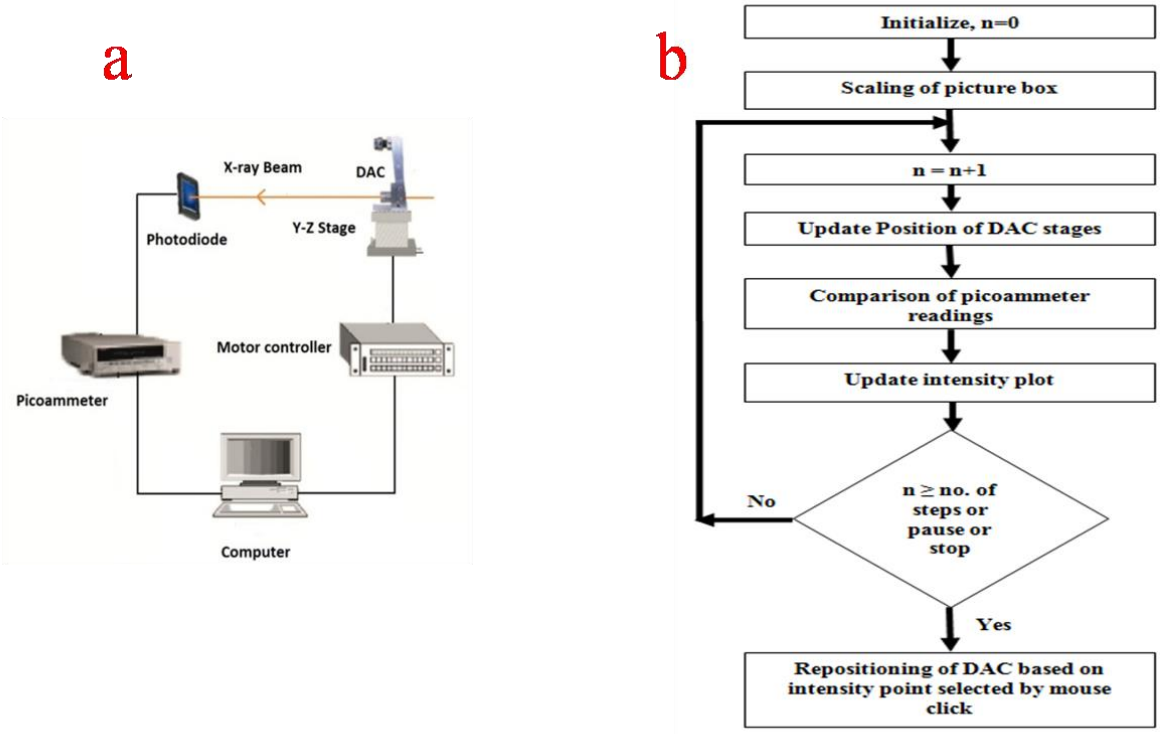

Figure 2.13 (a) Layout of different hardware components used in ‘Scanning Program’.

(b) Flow of instructions of software Program.

DAC is mounted on sample stage of goniometer. The existing software program for controlling sample stages of goniometer was in Visual Basic 6.0 as shown in Figure 2.14 (a). Several upgradations in this software have been carried out along with adding a ‘Scanning Program’. The Graphical User Interface (GUI) of the ‘Scanning Program’ is shown in Figure 2.14 (b). The ‘Scanning Program’ is interfaced with the picoammeter using GPIB (General Purpose Interface Bus) protocol. The software and hardware components are initialized at the beginning. The step length and the number of steps (maximum consecutive steps in one direction) can be selected by entering the values in ‘Scanning Parameter’ frame as shown in Figure 2.14 (b). Based on these parameters, the picture box of ‘Scanning Program’ is scaled and the program scans the sample (inside DAC) in *YZ* plane (perpendicular to synchrotron radiation beam). The schematic representation of movement pattern of DAC is shown in Figure 2.15.

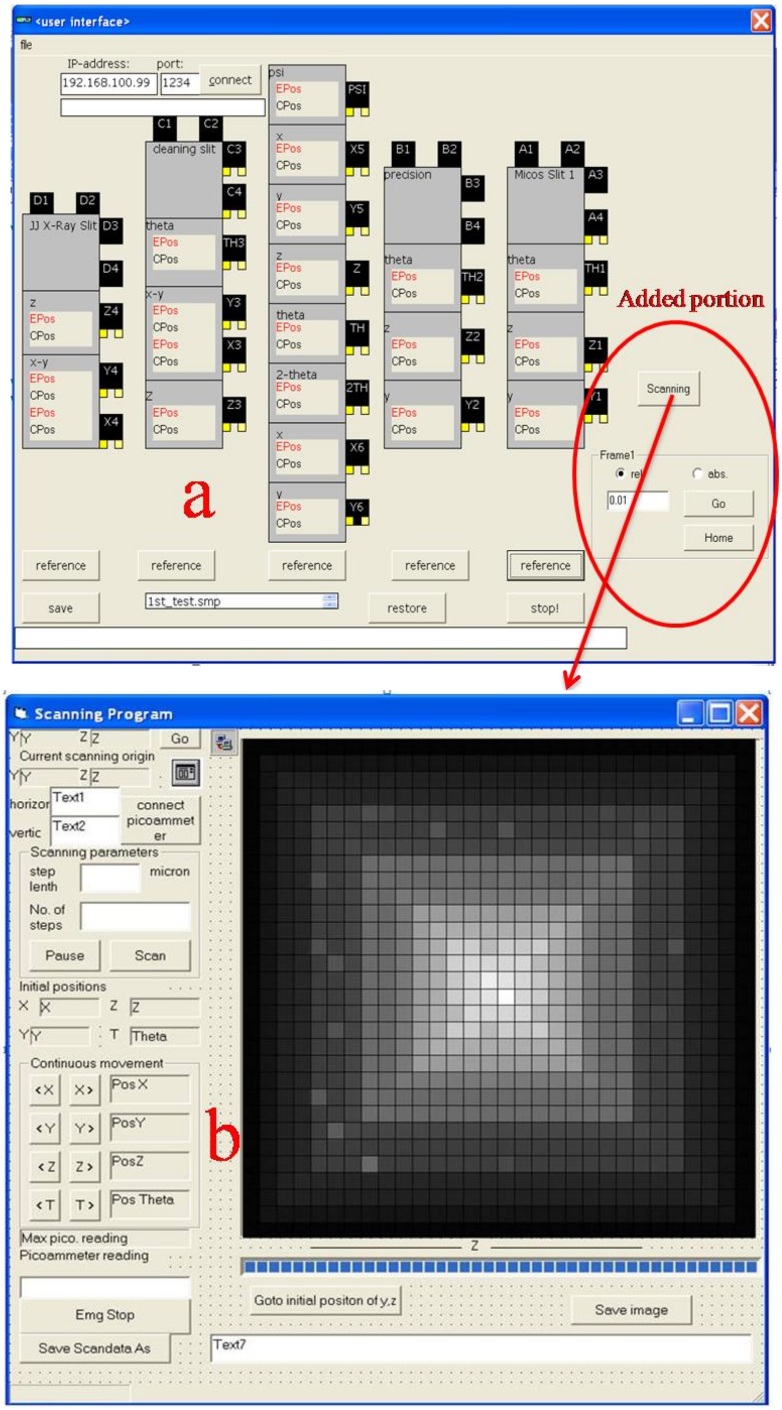

IP-address: 192.168.100.99
port: 1234
1st_test.smp
0.01

Figure 2.14 a) Existing software for goniometer. b) Added Graphical User Interface (GUI) of 'Scanning Program'. The brightest portion in picture box corresponds to desired alignment position of DAC.

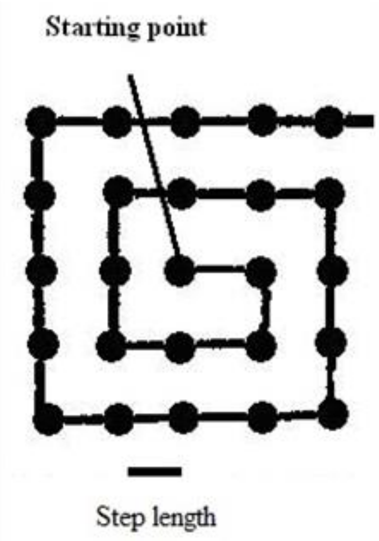

Figure 2.15 Movement pattern of DAC.

The beam transmission through the sample is monitored using silicon photo diode (through Keithley picoammeter) after each step. The program sketches the ‘square spiral pattern’ and this pattern represents the pictorial view of the movement of stages (*YZ*) of DAC. The colour intensity of each square corresponds to the value of the picoammeter current. After each movement of sample stage, the software program refreshes the colours of all preceding square boxes. The whitest portion of the ‘square spiral pattern’ represents the maximum value of picoammeter current while the darkest portion represents minimum value. By selecting the desired square box (using mouse click), corresponding positions of DAC stages (*Y* and *Z*) are displayed on the label boxes and the user can move the stages to that position. The maximum error in the aligned positions can be ± step length.

To conclude, in this chapter, I have presented different developmental works related to ECXRD beamline at Indus-2 synchrotron radiation source. The beamline is operational. The high pressure studies are being routinely carried out at ECXRD beamline.

Chapter 3: High pressure studies on α-cristobalite form of $Al_{0.5}Ga_{0.5}PO_4$

3.1 Introduction

SiO_2 is the most abundant material of the Earth's crust and mantle[79]. It exists in several polymorphs, such as quartz, tridymite, cristobalite, stishovite and coesite as shown in Figure 3.1[80]. Cristobalite is the high temperature polymorph of the silica which is found in two structures, *i.e.* low temperature (α) cristobalite, high temperature (β) cristobalite[81, 82]. The α-cristobalites can remain stable at ambient conditions in meta-stable form and find in volcanic rocks. The non-hydrostatic stresses play a crucial role in high pressure behaviour of α-cristobalites. Depending upon the degree of hydrostaticity of the applied pressure, α-SiO_2 may amorphize or undergo several crystal to crystal phase transitions[83-85]. $AlPO_4$, $GaPO_4$ and its solid solutions are isoelectronic analogous of silica and form isostructural compounds[86-88]. The studies of structural variations of these compounds under different thermodynamic conditions have received much attention as they provide models for SiO_2. Apart from its geological importance, these compounds have various technological applications. For example, $AlPO_4$ is used as binder for silica fibres in thermal power plant[89], protective coating on *C*-*C* composites in aircraft[90] and piezoelectric resonators[91]. The structural distortion in system $Al_{1-x}Ga_xPO_4$ varies linearly as a function of *Ga* composition (x), which provides the opportunity to tune its piezoelectric properties[92]. Fabrication of piezoelectric devices involves compaction of powder where individual grains experiences different stress conditions. It is essential to understand the behaviour of a material under these stress conditions. Previous high pressure investigations on α-cristobalite form of $AlPO_4$ show that its high pressure behaviour significantly depends on the nature of pressure conditions. Under non-hydrostatic pressure conditions, α-$AlPO_4$ transforms to monoclinic phase at 4 GPa which on further compression to 11 GPa transforms to $VCrO_4$ type orthorhombic *Cmcm* phase[53].

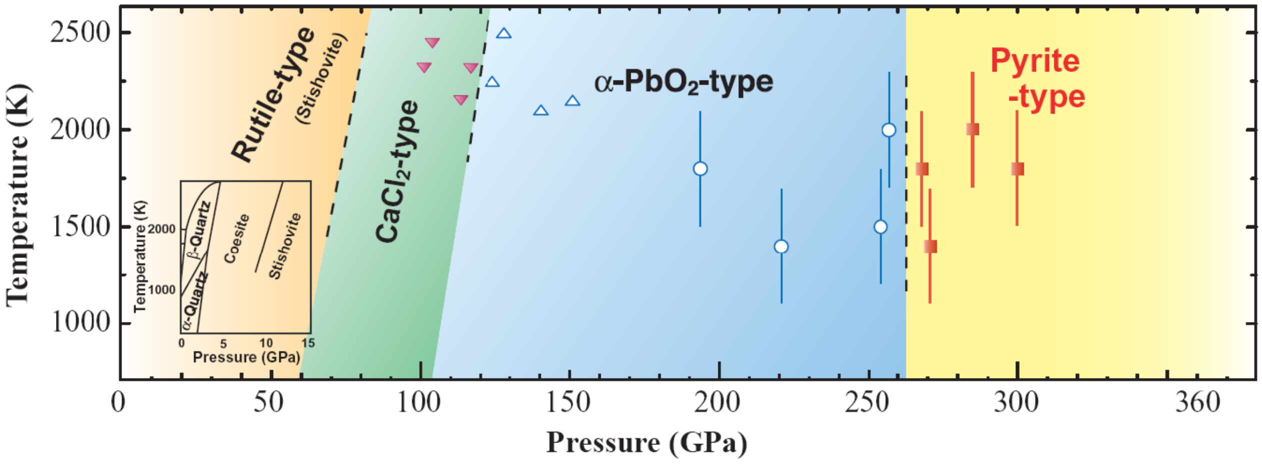

Figure 3.1 Phase diagram of SiO_2.

In contrast to non-hydrostatic behaviour, under hydrostatic conditions using N_2 as pressure transmitting medium (PTM), α-$AlPO_4$ transforms directly to the *Cmcm* phase. However, in case of $GaPO_4$, its α-cristobalite phase transforms to *Cmcm* phase *via.* intermediate monoclinic phase under hydrostatic conditions[54]. The intermediate phases observed in α-$AlPO_4$ (silicone oil as PTM) and α-$GaPO_4$ (Methanol-Ethanol as PTM) are different. In this context, the high pressure structural behaviour of solid solution of α-cristobalite forms of $AlPO_4$ and $GaPO_4$ under different pressure conditions can exhibit new phase with different sequence of transformation. With this motivation, α-$Al_{0.5}Ga_{0.5}PO_4$ has been studied using synchrotron based in-situ high pressure angle dispersive X-ray diffraction (XRD) under both hydrostatic and non-hydrostatic pressure conditions.

Following is the outline of the chapter. The next section (*i.e.*, 3.2) describes the preparation and characterization of the sample. The detailed methodology used in the experiment is presented in section 3.3. In the next section (*i.e.*, 3.4) experimental investigations of hydrostatic pressure conditions are presented. In the section 3.5, experimental investigations of non-hydrostatic pressure conditions are discussed.

3.2 Sample preparation and characterization

AR (Analytical Reagent) grade powders of aluminium chloride and gallium chloride in stoichiometric amounts were used as starting reagents. The amorphous precipitate of $Al_{0.5}Ga_{0.5}PO_4$ was obtained by adding NH_4OH to the aqueous solutions of aluminium chloride, gallium chloride and H_3PO_4. The precipitate was dried at about 175 ^{0}C and then annealed at 1300 ^{0}C for about 24 hours to get powdered sample of α-cristobalite form of $Al_{0.5}Ga_{0.5}PO_4$. The detailed method of preparation of the sample is given in the reference[93]. The lattice parameters of α-$Al_{0.5}Ga_{0.5}PO_4$ under ambient conditions, which were obtained by Rietveld refinement[58] are a = 7.0247(10) Å, b = 7.0315(8) Å, c = 6.9237(12) Å. The lattice parameters match fairly well with the earlier reported values a = 7.0295(12) Å, b = 7.0173(11) Å, c = 6.9217(5) Å[93]. The structure of α-$Al_{0.5}Ga_{0.5}PO_4$ at ambient conditions is shown in Figure 3.2. The α-$Al_{0.5}Ga_{0.5}PO_4$ has base centred orthorhombic structure (space group: $C222_1$) with four formula units in the unit cell. The compound is formed from corner linked AlO_4 or GaO_4 and PO_4 tetrahedra. The Rietveld refined X-ray diffraction pattern of α-$Al_{0.5}Ga_{0.5}PO_4$ at ambient conditions is shown in Figure 3.3. The refined atomic coordinates of ambient phase are shown in Table 3.1 which also match fairly well with earlier reported experimental values[93].

3.3 Experimental details

High pressure X-ray diffraction experiments were carried out at Extreme Conditions Beamline (ECB P2.02) at PETRA-III, DESY, Hamburg, Germany using a symmetric type diamond anvil cell (DAC) with perforated diamond anvils on the downstream side. These anvils reduce the relative contribution of Compton scattering from the diamond anvils which resulted in better signal to noise ratio during the high pressure measurements[94]. Powdered sample of α-$Al_{0.5}Ga_{0.5}PO_4$ and a tiny chip of ruby were loaded in a gasket hole (diameter ~ 0.2 mm) drilled in a pre-indented rhenium gasket.

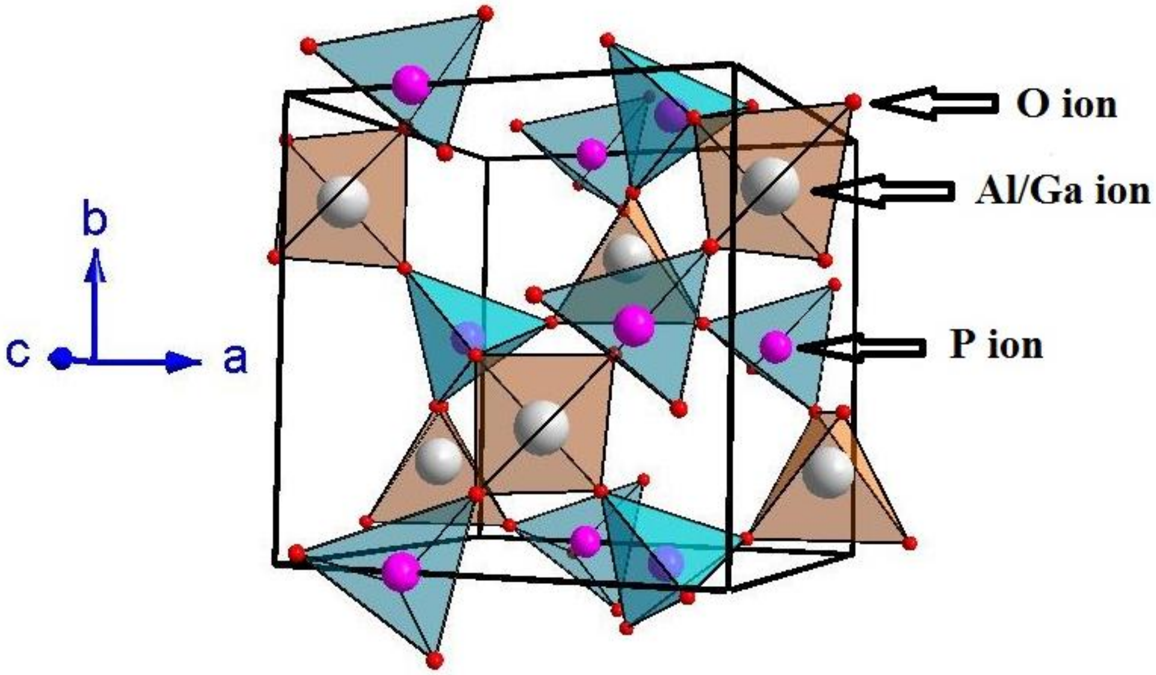

Figure 3.2 Pictorial representation of ambient C222$_1$ phase of $Al_{0.5}Ga_{0.5}PO_4$.

Atom	Wyckoff notation	X	Y	Z
Al / Ga	4(b)	0	0.196(3)	0.25
P	4(a)	0.310(5)	0	0
O(1)	8(c)	0.178(2)	0.050(3)	0.200(2)
O(2)	8(c)	0.431(2)	0.161(3)	0.918(1)

Table 3.1 Experimentally obtained atomic coordinates of orthorhombic C222$_1$ phase of $Al_{0.5}Ga_{0.5}PO_4$ at ambient pressure having lattice parameters: $a = 7.0247(10)$ Å, $b = 7.0315(8)$ Å, $c = 6.9237(12)$ Å.

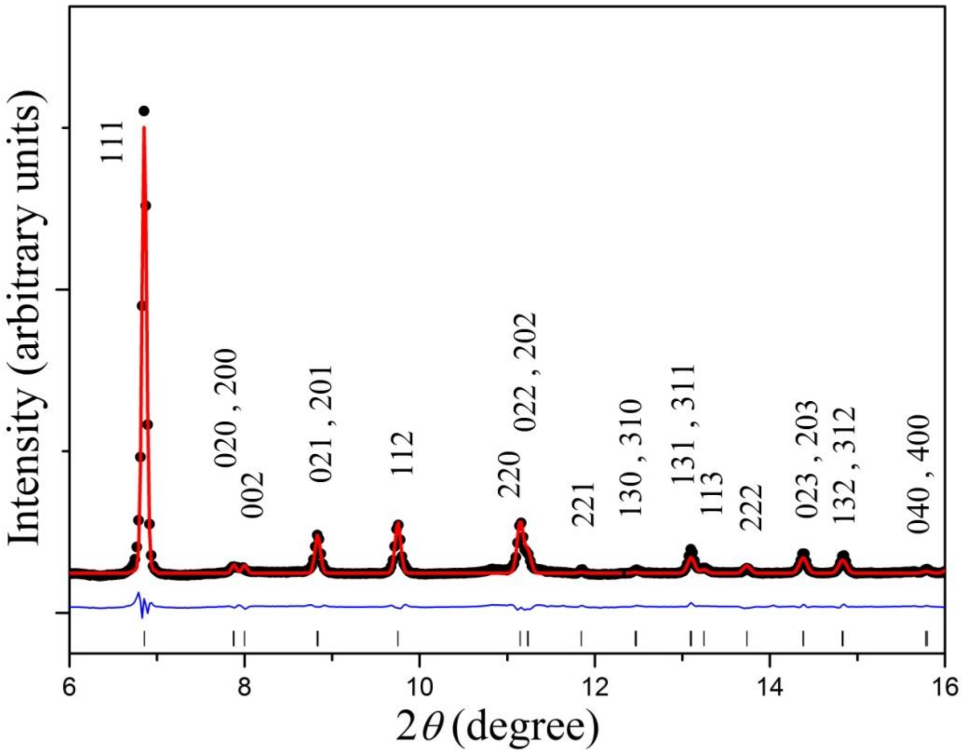

Figure 3.3 Rietveld refined X-ray diffraction pattern of $C222_1$ *phase of* $Al_{0.5}Ga_{0.5}PO_4$ *at ambient conditions. The observed data points are shown by. black symbols. The calculated data is represented by red line. Blue line shows the difference between observed and calculated data. The goodness of fit parameters are* $wRp = 0.01$, $Rp = 0.01$ *and* $R(F^2) = 0.41$.

Two sets of experiments were carried out on α-$Al_{0.5}Ga_{0.5}PO_4$ up to 19 GPa and 37.5 GPa respectively using x-rays of wavelength 0.4828 Å. In the first experiment, neon was used as a pressure transmitting medium (PTM). Neon remains hydrostatic up to 15 GPa and quasi hydrostatic up to highest pressure in the experiment, *i.e.* 19 GPa[36]. The second experiment was performed without any PTM. In both of these experiments, pressure inside the sample chamber was monitored by the ruby fluorescence method[45]. The errors in the determination of pressure using ruby fluorescence method was within 0.1 GPa. The diffraction images were collected using the flat panel detector XRD1621 from Perkin Elmer. After masking the unwanted portion of diffraction images, the images were converted into one dimensional diffraction patterns with the help of FIT2D software[56]. For measuring sample to detector distance, diffraction pattern of LaB_6 inside the DAC is being used. The X-ray diffraction patterns are refined by the Rietveld method using the software package GSAS[58].

3.4 High pressure phase under hydrostatic conditions

Diffraction patterns at a few selective hydrostatic pressures using neon as pressure transmitting medium are shown in Figure 3.4. With the increase in pressure, the diffraction peaks shift towards higher 2θ values as expected due to lattice contraction, albeit without appearance of any additional peaks up to 3.9 GPa pressure. On further compression to 4.9 GPa, several additional peaks are observed at various 2θ values as indicated with arrows in Figure 3.4. All these new diffraction peaks could be assigned to the orthorhombic *Cmcm* phase. In this phase *Al* or *Ga* becomes six coordinated with respect to the oxygen atoms while phosphorous continues to be four coordinated. More precisely, this structure can be described as formed by edge sharing Al/GaO_6 octahedra which are connected with PO_4 tetrahedra through vertices (Figure 3.5). The refined atomic coordinates of orthorhombic *Cmcm* phase are shown in Table 3.2.

This phase may considered an intermediate bridging phase between four fold and six fold structures, stabilized by the difficulty of breaking the energetic PO_4 bonds. The fact that ambient and high pressure phases coexist, suggests that the transition to high pressure phase is of first order in nature. On further increase in pressure, intensities of these new diffraction peaks of *Cmcm* phase increase relative to that of ambient phase. The Rietveld refined XRD pattern at 8.6 GPa is shown in Figure 3.6. The compressions in lattice parameters of the orthorhombic $C222_1$ and *Cmcm* phases are anisotropic with both the *b/a* and *c/a* ratios decrease under high pressure (Figure 3.7).

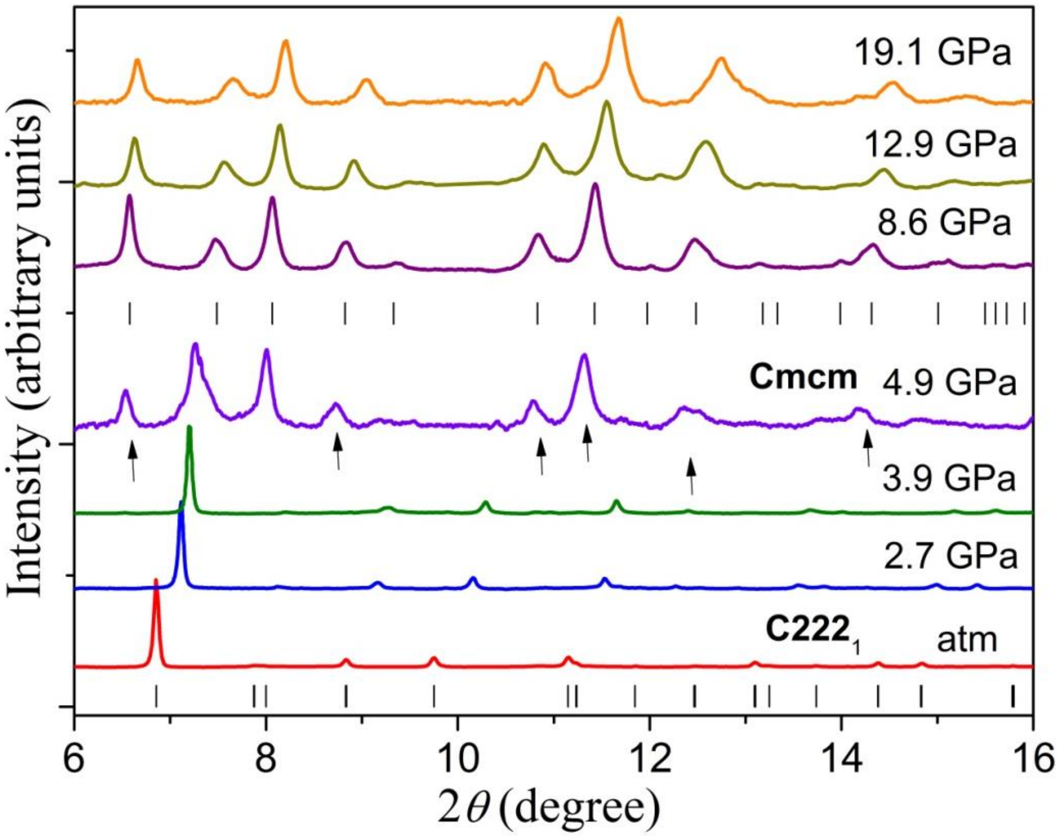

Figure 3.4 X-ray diffraction patterns of $Al_{0.5}Ga_{0.5}PO_4$ *at few selective pressures under hydrostatic conditions. The calculated positions of diffraction peaks for ambient phase and high pressure phases are shown by vertical lines.*

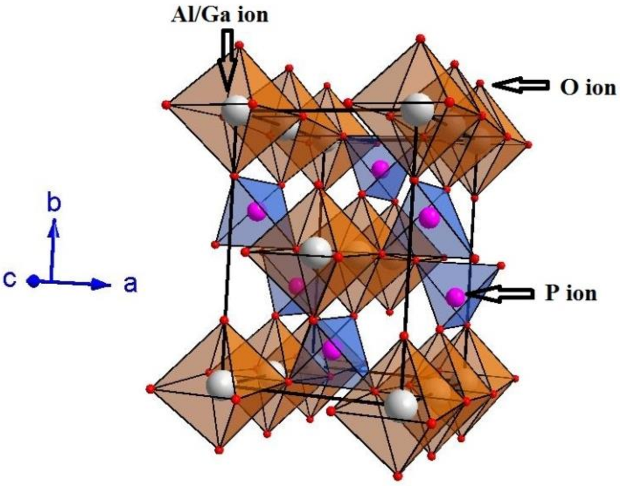

Figure 3.5 The pictorial representation of Cmcm phase of $Al_{0.5}Ga_{0.5}PO_4$*.*

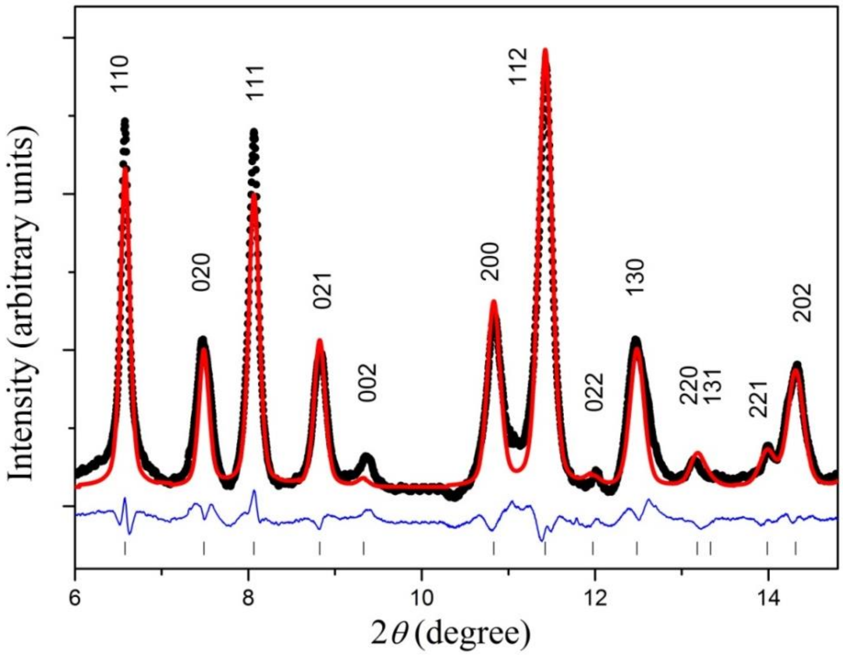

Figure 3.6 Rietveld refined X-ray diffraction patterns of $Al_{0.5}Ga_{0.5}PO_4$ *under hydrostatic pressure conditions (8.6 GPa) using neon as pressure transmitting medium. Vertical lines show the calculated positions of diffraction peaks for high pressure Cmcm phase. The observed data points are shown via. black symbols. The calculated data is represented by red line. Blue line shows the difference between observed and calculated data. The goodness of fit parameters are wRp = 0.01, Rp = 0.01 and* $R(F^2) = 0.20$.

Atom	Wyckoff notation	X	Y	Z
Al / Ga	4(a)	0	0	0
P	4(c)	0	0.352(3)	0.25
O(1)	8(f)	0	0.763(4)	0.979(5)
O(2)	8(g)	0.245(2)	0.994(5)	0.25

Table 3.2 Experimentally obtained atomic coordinates of orthorhombic Cmcm phase of $Al_{0.5}Ga_{0.5}PO_4$ *at 8.6 GPa having lattice parameters: a = 5.1154(4) Å, b = 7.3933(6) Å, c = 5.9353(4) Å.*

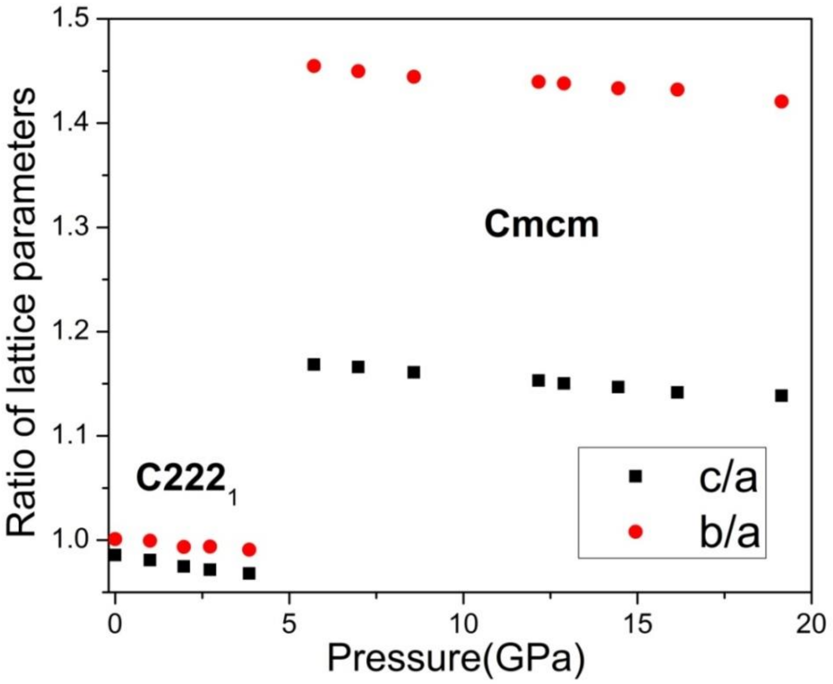

Figure 3.7 Ratio of lattice parameters of $Al_{0.5}Ga_{0.5}PO_4$ *under hydrostatic pressure conditions.*

The value of bulk modulus was determined by fitting the third order Birch Murnaghan equation of state[41] to measured pressure-volume data using EOSFit7 software (Figure 3.8)[95]. The bulk modulus for orthorhombic *Cmcm* phase is 126(4) GPa while that of orthorhombic $C222_1$ phase is 19(2) GPa. The large difference in values of bulk modulus of $C222_1$ and *Cmcm* phases of $Al_{0.5}Ga_{0.5}PO_4$ is attributed to open structure of cristobalites. This is also corroborated by the fact that the change in volume across this phase transition is found to be ~19%. The phase transition pressure ($C222_1$ to *Cmcm*) of α-$Al_{0.5}Ga_{0.5}PO_4$ is at 4.9 GPa, which takes place at lower pressures than that of α-$AlPO_4$ (8 GPa) [53] and higher pressure than that of α-$GaPO_4$ (4 GPa) [54]. The comparisons of bulk modulus and its pressure derivative of α-$Al_{0.5}Ga_{0.5}PO_4$ with that of α-$AlPO_4$ and α-$GaPO_4$ are shown in Table 3.3. The compressibility of α-$AlPO_4$ and α-$GaPO_4$[96] depend on the angles Al-O-P (143^0) and Ga-O-P (135^0) respectively[79]. Due to lower Ga-O-P bond angle and bigger size of *Ga* ion, the formation of six coordinated gallium (*i.e. Cmcm* phase) is easier in $GaPO_4$ in comparison to $AlPO_4$. Since, α-$Al_{0.5}Ga_{0.5}PO_4$ contains equal fraction of *Al* and *Ga* ions, the value of its compressibility is nearly average of α-$AlPO_4$ and α-$GaPO_4$.

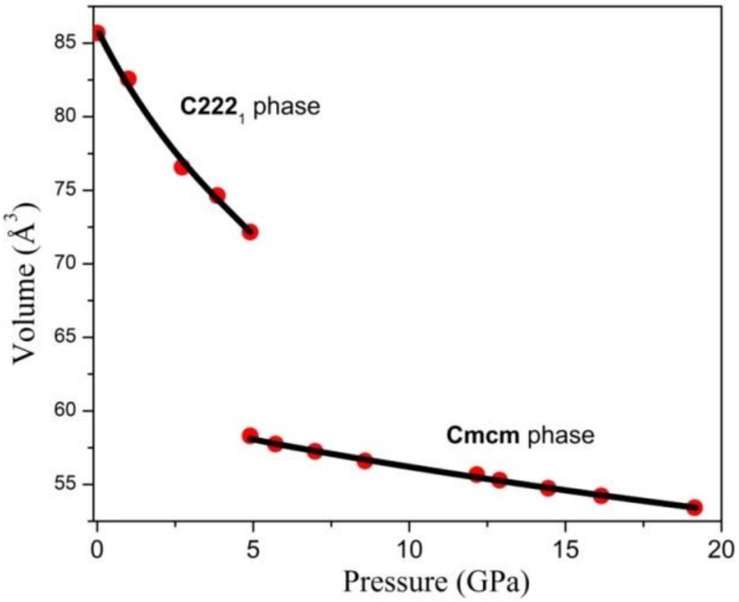

Figure 3.8 Measured volumes per formula unit with pressure of $Al_{0.5}Ga_{0.5}PO_4$ under hydrostatic pressure conditions are shown by solid symbol and fitting to third order Birch Murnaghan equation of state are shown by solid line (black). The errors in volumes are well within the size of symbols.

Substance	**Bulk Modulus** **B_0 (GPa)**		**Pressure Derivative of bulk modulus (B')**	
	$C222_1$	***Cmcm***	***$C222_1$***	***Cmcm***
$AlPO_4$	24(3)	118(7)	6(1)	4(fix)
$GaPO_4$	12(2)	144(6)	11.5(3.5)	5.2(0.4)
$Al_{0.5}Ga_{0.5}PO_4$	19 (2)	126(4)	3.3(1.4)	4

Table 3.3 Bulk modulus B and it's pressure derivative B' of $Al_{0.5}Ga_{0.5}PO_4$ compared with iso-structural compounds.

3.5 High pressure phase under non-hydrostatic conditions

X-ray diffraction patterns of α-$Al_{0.5}Ga_{0.5}PO_4$ under non-hydrostatic pressure conditions are shown in Figure 3.9. At very low pressure (0.6 GPa), diffraction peaks show broadening due to internal heterogeneous stress developed in the sample and few new peaks arise at different 2θ values (9.59, 11.05 etc.). At 4.4 GPa, several additional diffraction lines are observed at various values of 2θ.

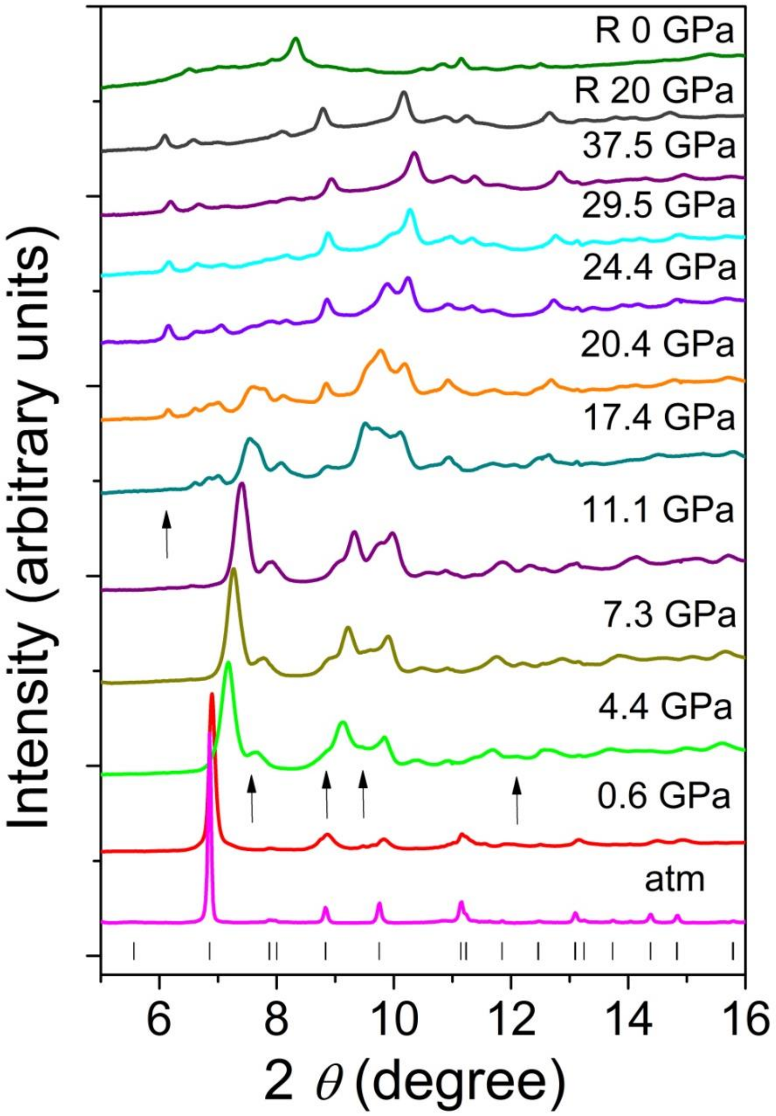

Figure 3.9 X-ray diffraction patterns of $Al_{0.5}Ga_{0.5}PO_4$ at few selective pressures under non-hydrostatic conditions. Vertical lines show the calculated positions of diffraction peaks for ambient phase.

On further increase in pressure, the relative intensity of diffraction peaks of orthorhombic $C222_1$ phase decrease while those of new phase increase. The signature of the ambient $C222_1$ phase is present at least up to 20.4 GPa.

The fact that ambient orthorhombic $C222_1$ and high pressure phases coexist, suggests that the transition to high pressure phase is of first order in nature. Due to non-hydrostatic pressure conditions, increase in the sample pressure leads to non-uniform stresses in the sample chamber which lead to broadening of all the diffraction peaks. Several reported structures of $AlPO_4$, $GaPO_4$ and $InPO_4$, such as $CrVO_4$ type orthorhombic *Cmcm* phase, $CaCl_2$ type monoclinic phase (space group $P2/m$), scheelite, zircon type's tetragonal structures and recently proposed $Pmn2_1$ type orthorhombic structure by Angot *et al.* (obtained above 10 GPa from α-quartz form of $Al_{0.3}Ga_{0.7}PO_4$)[97] were tried for refining the non-hydrostatic pressure XRD data of $Al_{0.5}Ga_{0.5}PO_4$. However, none of these could satisfactorily refine the diffraction patterns, suggesting that our observed phase is different from high pressure phases of these isoelectronic compounds. Using Crysfire indexing software[98] and Le Bail refinement, the new peaks emerging under non-hydrostatic conditions, could be best indexed with a monoclinic $P2_1$ phase with lattice parameters comparable to a monoclinic phase predicted earlier for $GaPO_4$ using molecular dynamics simulations[99]. The predicted monoclinic phase contains layers of six coordinated Al/Ga ions separated by less dense five coordinated Al/Ga ions. The unit cell of this $P2_1$ phase contains six formula units. The unit cell has three types of *Al/Ga* sites; one *Al/Ga* ion has five coordinations with oxygen atoms while other two *Al/Ga* have six coordinations. The phosphorous atom remains four coordinated. The Pictorial representation of $P2_1$ phase is shown in Figure 3.10. Using fractional coordinates of this $P2_1$ phase[99], the XRD data could be Rietveld refined satisfactorily up to 7.3GPa with wRp < 0.03. The Rietveld refined diffraction patterns at 7.3 GPa pressures is shown in Figure 3.11.

At higher pressures, Rietveld refinement could not be performed due to very broad overlapping diffraction peaks, though XRD data has been analysed with Le Bail refinement up to 14.3 GPa to obtain evolution of lattice parameters with pressure. The comparison of ratio of lattice parameters of the $C222_1$ phase under hydrostatic and non-hydrostatic pressure conditions is shown in Figure 3.12. Due to the generation of deviatoric stresses, the compression in lattice parameters is higher in non-hydrostatic case.

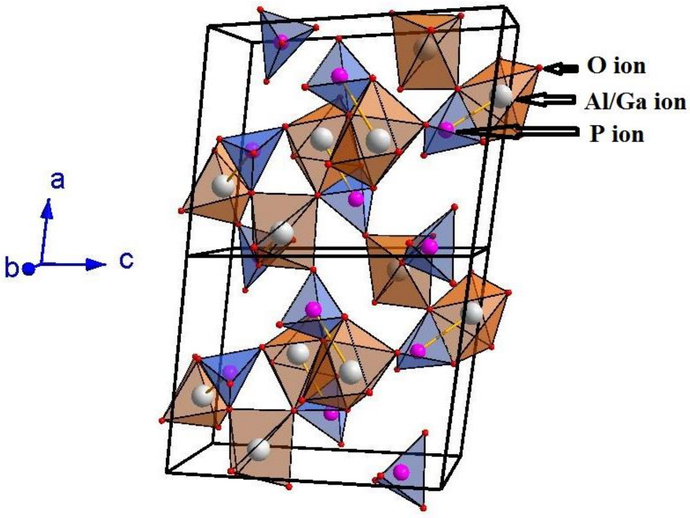

Figure 3.10 The pictorial representation of $P2_1$ *phase of* $Al_{0.5}Ga_{0.5}PO_4$*.*

I have determined the value of bulk modulus by fitting the Birch Murnaghan equation of state (third order for $C222_1$ and second order for $P2_1$ phases) to measured pressure-volume data of non-hydrostatic conditions (Figure 3.13) using EOSFit7 software. The bulk modulus for orthorhombic $C222_1$ phase of $Al_{0.5}Ga_{0.5}PO_4$ under non-hydrostatic pressure conditions was determined to be 22(4) GPa which matches fairly well with that of our hydrostatic case *i.e.* 19(2) GPa. The bulk modulus for monoclinic $P2_1$ phase of $Al_{0.5}Ga_{0.5}PO_4$ under non-hydrostatic pressure conditions was found to be 41(4) GPa.

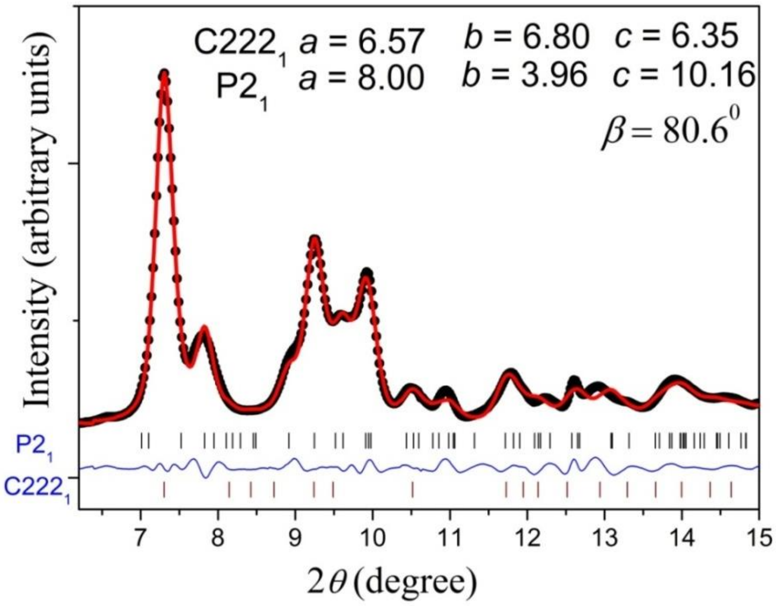

Figure 3.11 Rietveld refined X-ray diffraction patterns of $Al_{0.5}Ga_{0.5}PO_4$ at 7.3 GPa under non-hydrostatic pressure conditions. The observed data points are shown via. black symbols. The calculated data is represented by red line. Blue line shows the difference between 'observed-calculated' data. The goodness of fit parameters are wRp = 0.03, Rp = 0.02 and $R(F^2)$ = 0.11. Weight fractions of monoclinic P2$_1$ and orthorhombic C222$_1$ phases are ~70% and 30% respectively.

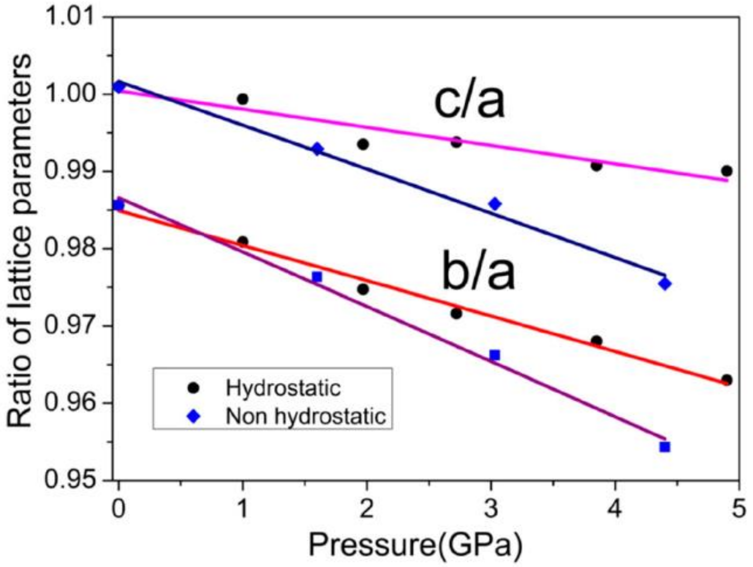

Figure 3.12 Ratio of lattice parameters of C222$_1$ phase of $Al_{0.5}Ga_{0.5}PO4$ under hydrostatic and non-hydrostatic pressure conditions.

The first order pressure derivative of bulk modulus (B') for *$C222_1$* and *$P2_1$* phases were 7.0 ± 2.1 and 4 respectively. Our studies show that non-hydrostatic stress conditions can radically alter the compression behaviour of α-cristobalite form of $Al_{0.5}Ga_{0.5}PO_4$. The emergence of exotic behaviour of SiO_2 polymorph due to non-hydrostatic stress has already been reported in several studies. Ĉernok *et. al* have stated that under quasi-hydrostatic pressure conditions, α-cristobalite form of SiO_2 transformed to a monoclinic polymorph built out of silicon octahedral at ~ 11 GPa, which is not observed under hydrostatic pressure conditions up to 15 GPa[100]. In another study, Badro *et. al* have shown that under deviatoric stress with stress tensors: $\sigma_{xx} = 20$ GPa, $\sigma_{yy} = 20$ GPa, $\sigma_{zz} = 27$ GPa, α-quartz form of SiO_2 transformed to five coordinated Si polymorph[101].

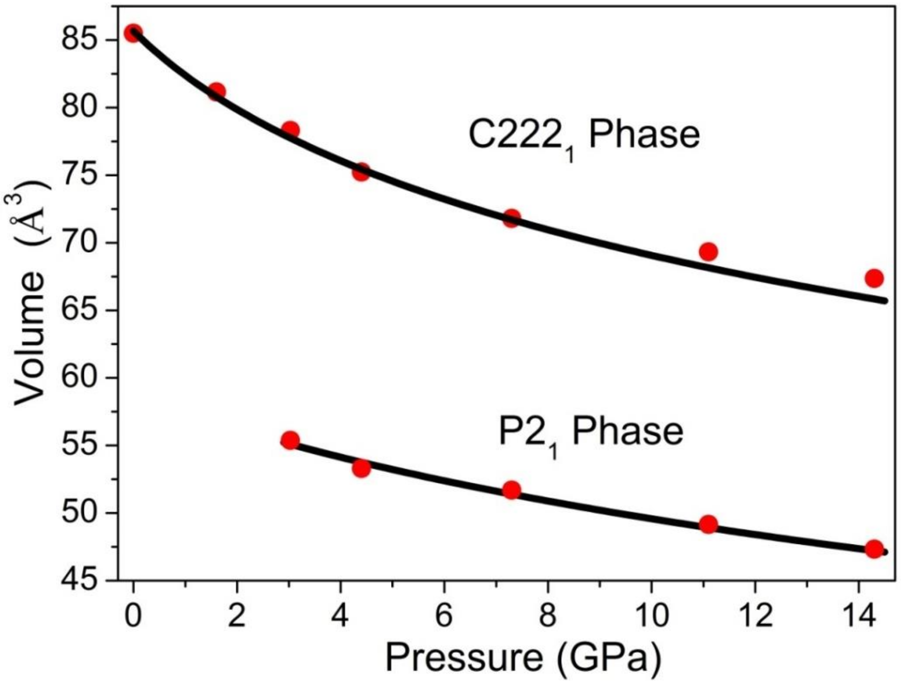

Figure 3.13 Measured volumes per formula unit with pressure of $Al_{0.5}Ga_{0.5}PO_4$ under non-hydrostatic pressure conditions are shown by solid symbol and fitting to Birch Murnaghan equation of state (third order for $C222_1$ and *second order for $P2_1$ phases) are shown by solid line (black). The errors in volumes are well within the size of symbols.*

In order to verify high pressure structural stability regime of monoclinic $P2_1$, orthorhombic $C222_1$ and $Cmcm$ phases, we have performed density functional theory (DFT) based first principle calculations within generalized gradient approximation (GGA) method on $AlPO_4$ and $GaPO_4$. The density functional theory based calculations have been performed with *Vienna ab initio* simulation package (VASP) within the frame work of the projector augmented wave (PAW) approach[102, 103]. The generalized gradient approximation method[104] was used for exchange-correlation part of the total energy. The energy cutoff of plane waves was set to 600 eV. The *k* mesh of 18 × 18 × 9 Monkhorst-Pack[105] scheme was used. The convergence criteria was set to be 10^{-6} eV in the self consistent field (SCF) cycle. The structures have been optimized by minimizing the forces on each atom in such a way that the total force on it remains below 10^{-2} eV/Å.

In order to find relative structural stability of $C222_1$, $Cmcm$ and $P2_1$ phases of $AlPO_4$ and $GaPO_4$ under pressure, total energy has been calculated after variable cell structural relaxation calculations at various volumes. The relative enthalpies of $Cmcm$ and $P2_1$ phases of $AlPO_4$ and $GaPO_4$ are shown in Figure 3.14. In case of $AlPO_4$, compared to ambient orthorhombic $C222_1$ phase, the monoclinic $P2_1$ phase becomes stable in the pressure range (0.6 GPa - 5.3 GPa). At higher pressure *i.e.* above 5.3 GPa orthorhombic $Cmcm$ phase becomes stable. In the previous high pressure study on $AlPO_4$, the authors observed intermediate monoclinic phase under non-hydrostatic conditions[53]. Under hydrostatic conditions, the monoclinic phase might be kinetically hindered. Whereas, in case of $GaPO_4$, using Methanol-Ethanol as pressure transmitting medium, Ming *et al.* have found intermediate monoclinic phase in the phase transition from ambient $C222_1$ phase to $Cmcm$ phase[54]. This can be due to small non-hydrostatic stresses generated in experiments. The studies on $AlPO_4$ and $GaPO_4$ show that non-hydrostatic conditions play an important role in stabilizing monoclinic phase.

In the present high pressure studies on α-$Al_{0.5}Ga_{0.5}PO_4$ under non-hydrostatic conditions, we have not observed *Cmcm* phase up to 37.5 GPa. The α-$Al_{0.5}Ga_{0.5}PO_4$ is equimolar solution of α-$AlPO_4$ and α-$GaPO_4$. The differences in the enthalpies of *Cmcm* and $P2_1$ phases of $AlPO_4$ and $GaPO_4$ are small near the phase transition zone.

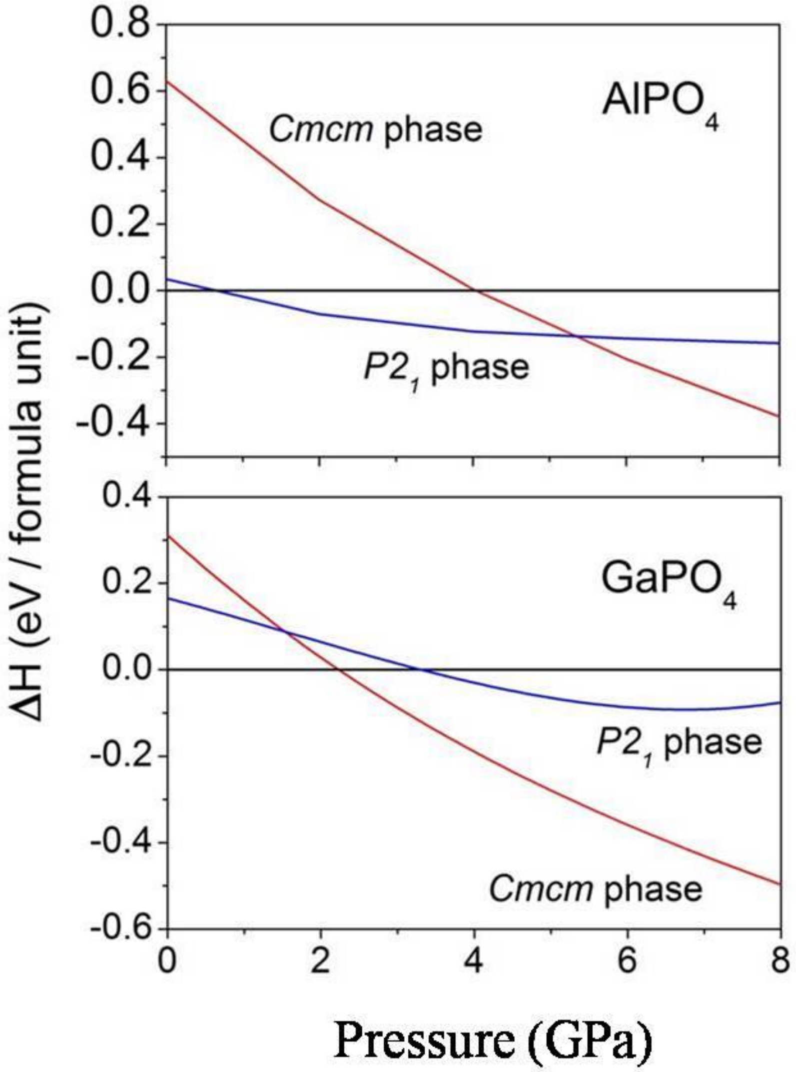

Figure 3.14 Simulated enthalpies of Cmcm and $P2_1$ *phases relative to ambient* $C222_1$ *phase of* $AlPO_4$ *and* $GaPO_4$*.*

Due to internal heterogeneous stresses and non-hydrosttic conditions, ambient $C222_1$ phase of α-$Al_{0.5}Ga_{0.5}PO_4$ may transform to $P2_1$ phase and further transformation of $P2_1$ phase to *Cmcm* phase may not be possible up to 37.5 GPa.

To conclude, In this chapter, I have shown that the non-hydrostatic stress plays an important role in the high pressure polymorphism of α–cristobalites. The studies presented in this chapter added much interest from the point of view of synthesizing new crystalline phases under non-hydrostatic conditions.

Chapter 4: Preparation and high pressure studies on $InPO_4$

4.1 Introduction

Indium phosphate ($InPO_4$) has been received substantial attention because of its applications in electronic, optoelectronics and telecommunications industries[106]. $InPO_4$ may also be formed on the oxidized surface of Indium phosphide based semiconductors. The physical properties of the material depend on the structure. Therefore, the understanding of structural behaviour of $InPO_4$ may help to fabricate better electronics components. At ambient conditions, $InPO_4$ crystallizes in the orthorhombic *Cmcm* phase ($CrVO_4$ type structure). This phase is the high pressure phase of α-cristobalite form of $Al_{0.5}Ga_{0.5}PO_4$, $AlPO_4$ and $GaPO_4$[53, 54, 107] which are isoelectronic analogous of silica[86, 108]. Therefore, the studies of structural variations of $InPO_4$ under different thermodynamic conditions may also be useful in the field of Earth science. Due to bigger atomic size of *In* atom compared to Al or Ga, the chemical pressure induced in the structure which leads to stabilize *Cmcm* phase of $InPO_4$ even at ambient conditions. In this phase, *In* is found in six coordination with respect to the oxygen atoms while phosphorous is in four coordination. More precisely, this structure can be described as formed by edge sharing InO_6 octahedra which are connected with PO_4 tetrahedra through vertices as shown in Figure 4.1.

The *Cmcm* phase may be thought of as an intermediate phase, between fourfold (P^{5+} ion) and six fold (In^{3+} ion) structures, stabilized by the resistance to the breaking of the strong PO_4 bonds. In all the phosphates of group 3A elements, such as $AlPO_4$, $GaPO_4$, $InPO_4$, $TlPO_4$, the observation of six coordinated phosphorous is rare. Till date only six coordinated phosphorous is reported for $AlPO_4$. P-Porres et al. have shown that α-quartz form of $AlPO_4$ transforms to *Cmcm* phase under pressure. On further compression to 46 GPa, the *Cmcm* phase transforms to a monoclinic $CaCl_2$ type of phase, where the phosphorous atoms become six coordinated[52]. As $InPO_4$ is already in *Cmcm* phase at ambient conditions, it may be possible to realize six coordinated phosphorous at much lower pressure compared to $AlPO_4$. With this motivation, high pressure structural investigations have been carried out on $InPO_4$ using synchrotron based angle dispersive X-ray diffraction (XRD) and Raman scattering methods.

Following is the outline of the chapter. In the next section 4.2, the preparation methodology of sample is presented. The details of experimental studies are shown in section 4.3. High pressure Raman studies are presented in section 4.4 and section 4.5 describes the high pressure X-ray diffraction investigations.

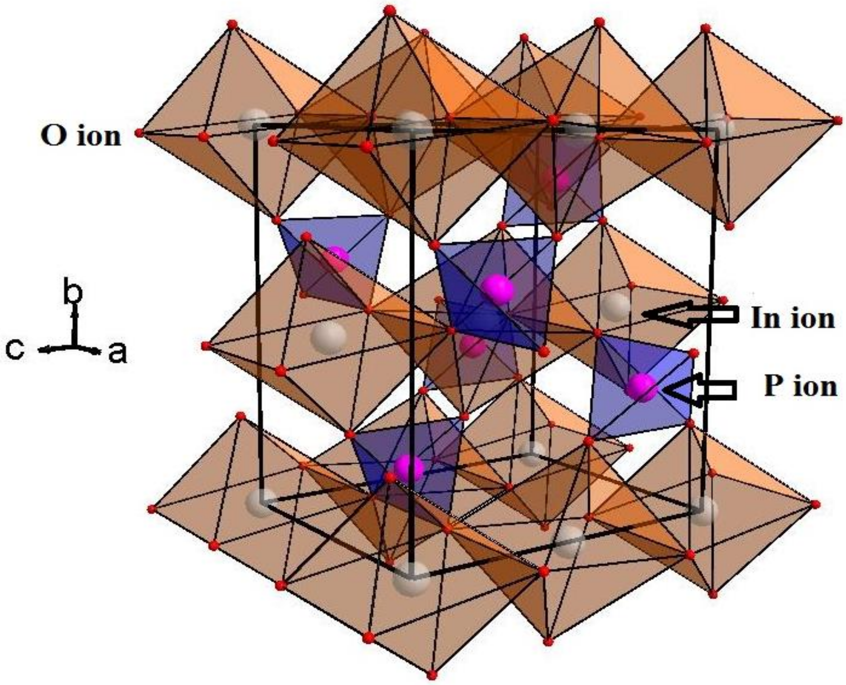

Figure 4.1 The pictorial representation of ambient Cmcm phase of $InPO_4$.

4.2 Sample preparation

The powdered form of $InPO_4$ has been synthesized by following methods:

Solid state reaction method

Analytical Reagent (AR) grade powders of In_2O_3 and $(NH4)_2HPO_4$ in stoichiometric amounts were used as starting reagents. Reactants of suitable weights were homogenised by grinding, pelletized and heated at 400 ^{0}C for 24 hours in order to remove NH_3 and H_2O. Next the mixtures were calcined in the following three stages: 850 ^{0}C (24 h), 900 ^{0}C (24 h), 950 ^{0}C (24 h). In all the stages, the heating and cooling rate were kept to 6 ^{o}C per minute. In the third stage of heating (*i.e.* 950 ^{0}C), the powdered form of $InPO_4$ is obtained which can be described by following equation:

$$\boxed{2\,(NH4)_2HPO_4 + In_2O_3 \Longrightarrow 4\,NH_3 \Uparrow + 2\,InPO_4 + 3\,H_2O \Uparrow}$$

The detailed method of preparation of the sample is given in the reference[109]. However, our XRD pattern shows that ~ 4% In_2O_3 is still present as shown in Figure 4.2. It seems that at temperature 950 ^{0}C $InPO_4$ decomposes to In_2O_3.

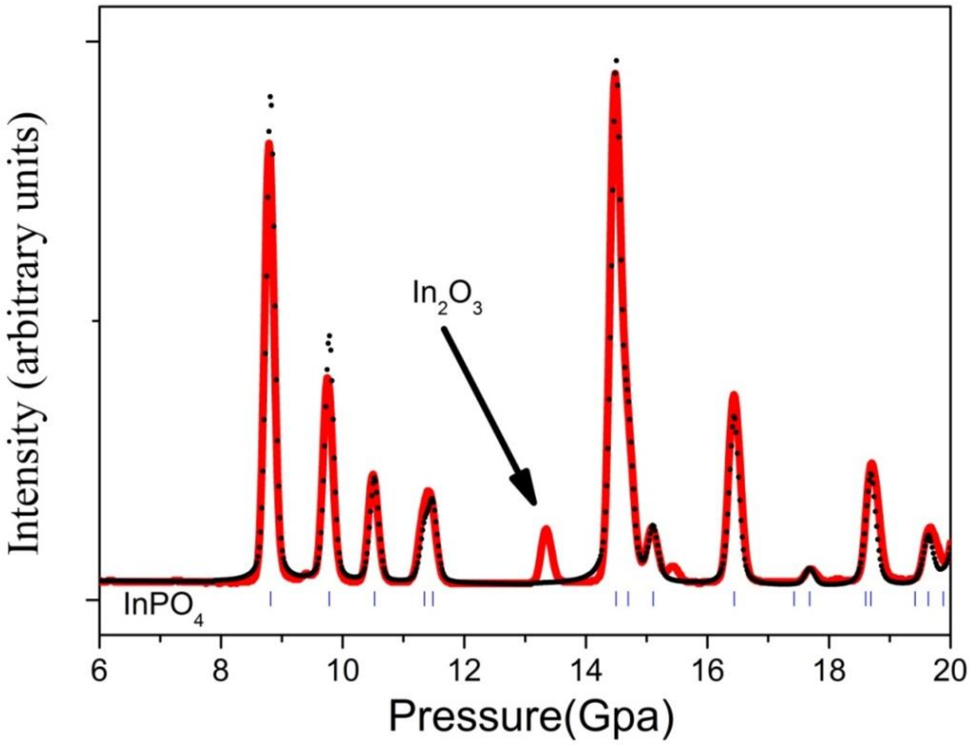

Figure 4.2 Rietveld refined X-ray diffraction pattern ($\lambda = 0.6783$ Å) of Cmcm phase of $InPO_4$ at ambient conditions. The observed data points are shown via. black symbols. The calculated data is represented by red line. The goodness of fit parameters are wRp = 0.05, Rp = 0.02 and $R(F^2) = 0.89$.

Co-precipitation method

In order to synthesize pure $InPO_4$, *i.e.* without In_2O_3, co-precipitation method has been used. Indium chloride solution is obtained by dissolving In_2O_3 powder (Analytical Reagent grade) in concentrated HCl. Then appropriate amount of H_3PO_4 (85 wt%) was added. As the reaction required basic medium, few drops of NH_4OH (25 wt%) have been added to the continuously stirred solution. A white precipitate was formed, which was separated by filtration. The precipitate was washed three times with distilled water and two times with ethanol. After drying at 100 ^{0}C for 10 hours, the precipitate was calcined in box furnace at 400 ^{0}C for 24 hours in order to remove NH_3 and H_2O. Further the precipitate was calcined at 825 ^{0}C (24 hours) to obtain $InPO_4$ which can be described by following equation:

$$2H_3PO_4 + 2InCl_3 \xrightarrow[NH_4OH]{825\ ^0C} 2\ InPO_4 + 6HCl$$

Phase purity of the ensuing powder was determined by X-ray diffraction (XRD) at ambient conditions, before using the same for high pressure Raman and XRD measurements.

4.3 Experimental details

Raman spectroscopic measurements were carried out on a Jobin Yvon triple-stage T64000 Raman spectrometer in back scattering geometry. Coherent make Ar^+ ion laser (488 nm) was used for excitation of Raman modes. Raman scattered signal is collected by 20x objective lens (Olympus, Japan) and analyzed by triple-stage spectrograph in subtractive geometry with a Peltier cooled charge-coupled device detector (Synapse). Raman modes are recorded in the range of 100 to 1250 cm^{-1} with 1800 grooves per mm grating providing the resolution of ~ 3 cm^{-1}.

High pressure angle dispersive X-ray diffraction (XRD) experiments were carried out on Extreme Conditions X-ray Diffraction (ECXRD) beamline at Indus-2 (synchrotron radiation source, India)[66], using a Mao Bell type diamond anvil cell (DAC)[1]. The used wavelength of x-rays was 0.6125 Å and the diffraction data were collected using MAR345 image plate area detector. Ruby ball was used to monitor the applied pressure during the XRD and Raman scattering experiments[45]. The errors in the determination of pressure using ruby fluorescence method was below 0.1 GPa. In both the Raman scattering and X-ray diffraction experiments, the hydrostatic pressure conditions inside the sample chamber is maintained using a mixture of methanol and ethanol (4:1) as a pressure transmitting medium (PTM). The PTM remains hydrostatic up to nearly 10 GPa[36]. The powdered sample along with ruby ball and pressure transmitting medium (Methanol-ethanol) were loaded in a gasket hole of diameter ~ 0.2 mm which was drilled in a pre-indented tungsten gasket. The wavelength and the 'sample to detector distance' were refined by diffraction pattern of standards CeO_2 and LaB_6. Two dimensional diffraction data were converted into one dimensional diffraction profiles with the help of FIT2D software[56]. The diffraction patterns were analyzed using Rietveld refinement method as implemented in GSAS software[58].

The Rietveld refined X-ray diffraction pattern of $InPO_4$ at ambient conditions is shown in Figure 4.3. The lattice parameters of $InPO_4$ under ambient conditions obtained by Rietveld refinement[58] are a = 5.3212(10) Å, b = 8.0096(8) Å and c = 6.7955(12) Å. These match fairly well with the earlier reported values a = 5.3355 Å, b = 8.0454 Å, c = 6.8255 Å[110]. The structure of $InPO_4$ at ambient conditions is shown in Figure 4.1. $InPO_4$ has *C*-centred orthorhombic structure (space group: *Cmcm*) with four formula units in the unit cell. The refined atomic coordinates of ambient phase (Table 4.1) also match fairly well with earlier reported values[110].

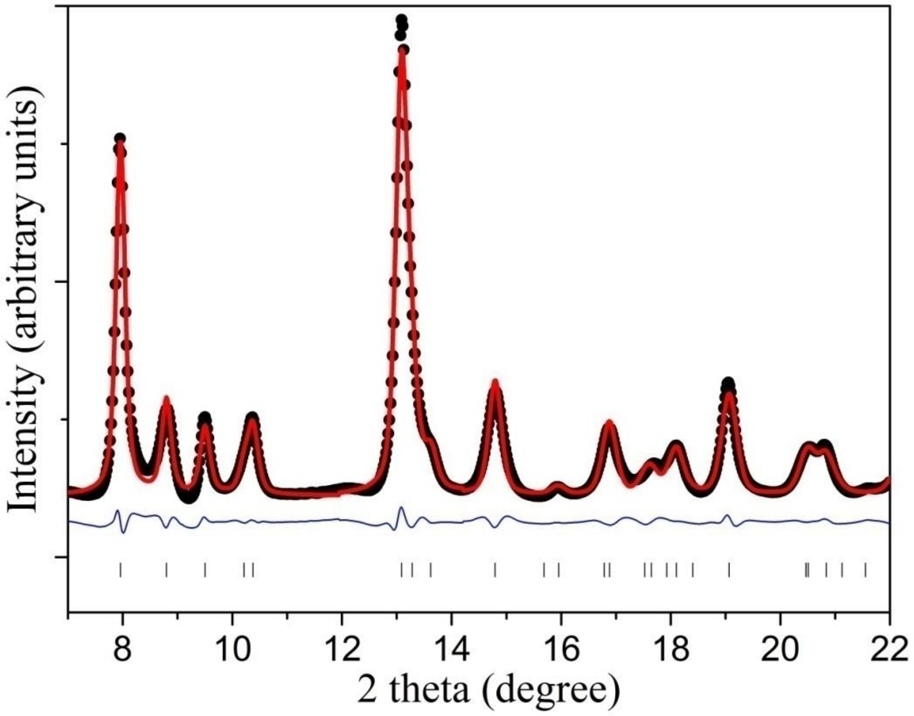

Figure 4.3 Rietveld refined X-ray diffraction ($\lambda = 0.6125$ Å) pattern of Cmcm phase of $InPO_4$ at ambient conditions. The observed data points are shown via. black symbols. The calculated data is represented by red line. Blue line shows the difference between observed and calculated data. Indexing of Cmcm phase is shown by vertical lines. The goodness of fit parameters are wRp = 0.03, Rp = 0.04 and $R(F^2) = 0.61$.

Atom	Wyckoff notation	X	Y	Z
In	4(a)	0	0	0
P	4(c)	0	0.3407(15)	0.25
O(1)	8(g)	0.2162(20)	0.4676(22)	0.25
O(2)	8(f)	0.431(2)	0.2392(20)	0.0603(20)

Table 4.1 Experimentally obtained atomic coordinates of orthorhombic Cmcm phase of $InPO_4$ at ambient pressure.

4.4 High pressure Raman studies

The unit cell of ambient *Cmcm* phase of $InPO_4$ contains four formula units. The analysis from group theory showed that it has total 36 Γ point phonon modes[110].

$$\Gamma_{Total} = 5\ A_g + 4\ B_{1g} + 6\ B_{1u} + 3\ A_u + 2B_{2g} + 7\ B_{2u} + 4\ B_{3g} + 5\ B_{3u}$$

Out of these 36 modes, 15 modes are Raman active.

$$\Gamma_{Raman} = 5\ A_g + 4\ B_{1g} + 2B_{2g} + 4\ B_{3g}$$

Total IR active modes are also 15.

$$\Gamma_{IR} = 5\ B_{1u} + 6\ B_{2u} + 4\ B_{3u}$$

In the orthorhombic *Cmcm* phase of $InPO_4$, InO_6 octahedra are connected with PO_4 tetrahedra through vertices. The nature of *P–O* and *In–O* bondings is significantly different in character. The value of electro negativity is 2.187 for the P^{5+} cation and 1.436 for In^{3+} cation[111]. Therefore *P–O* bonds demonstrate covalent characters, whereas the *In–O* bonds are predominately of ionic character. The intensities of vibrational modes of PO_4 tetrahedra are sufficiently higher in comparison to that of InO_6 octahedra. Hence, Raman modes of $InPO_4$ can be interpreted in terms of vibrational frequencies of PO_4 tetrahedra. T_d symmetry of $(PO_4)^{3-}$ ion in free space is reduced at the crystal site. The internal vibrations of PO_4 tetrahedron at the crystal site can be depicted as shown in Table 4.2.

Raman spectroscopic studies on Orthorhombic *Cmcm* phase of $InPO_4$ were performed up to 21.6 GPa. Out of fifteen Raman active modes, only ten modes are observed in the recorded spectrum at ambient conditions (Figure 4.4). The Raman modes are observed at 164, 240, 424, 471, 548, 633, 905, 948, 1047 and 1161 cm^{-1} (named as P_1, $P_{2.....}$ P_{10} respectively) as shown in Figure 4.4. These modes match well with the earlier reported experimental values (175, 243, 416, 429, 548, 908, 950, 1048, 1164 cm^{-1})[112, 113]. There is a small difference in some of the observed Raman modes with earlier reported values. This could be because previous Raman modes were studied by Rojas-L´opez et al. from thin film sample[113].

$(PO_4)^{3-}$ (T_d)		Orthorhombic (*Cmcm*)		Tetragonal ($I4_1/amd$)		Tetragonal ($I4_1/a$)
	Site Group C_{2v}	Factor Group D_{2h}	Site Group D_{2d}	Factor Group D_{4h}	Site Group S_4	Factor Group C_{4h}
A_1 (υ_1)	$A_1 \rightarrow$	A_g+B_{2u}	$A_1 \rightarrow$	$A_{1g}+B_{2u}$	$A \rightarrow$	A_g+B_u
E (υ_2)	$A_1+A_2 \rightarrow$	$A_g+B_{2g}+A_u+B_{2u}$	$A_1+B_1 \rightarrow$	$A_{1g}+B_{2g}+A_{1u}+B_{2u}$	$A+B \rightarrow$	$A_g+B_g+A_u+B_u$
F_2 (υ_3 & υ_4)	$A_1+B_1+B_2 \rightarrow$	$A_g+B_{1g}+B_{3g}+B_{1u}+B_{2u}+B_{3u}$	$B_2+E \rightarrow$	$B_{1g}+E_g+A_{2u}+E_u$	$B+E \rightarrow$	$B_g+E_g+A_u+E_u$

Table 4.2 Internal modes of PO_4 ion in different structures.

Lopez-Moreno and D Errandonea[110] have assigned all the modes as internal and external modes of (PO_4) tetrahedron. All the modes observed above 400 cm^{-1} correspond to the internal vibrations of (PO_4) molecule. The Raman modes observed in the range 400 to 650 cm^{-1} represent the bending of *O-P-O* vibrations. The mode P_4 represents symmetric bending vibration. Most intense peak centred at 548 cm^{-1} (P_5) is A_g mode. The modes P_5 and P_6 (633 cm^{-1}) correspond to asymmetric bending of PO_4 tetrahedra. The modes P_7, P_8 and P_{10} are correspond to asymmetric stretching while mode P_9 represents the symmetric stretching of PO_4 tetrahedra[110]. Raman spectra of *Cmcm* phase of $InPO_4$ at a few selective pressures are shown in Figure 4.5. With increase in pressure, all the Raman modes monotonously shifted to higher wavenumbers up to 10.8 GPa suggesting the persistence of the ambient orthorhombic phase up to 10.8 GPa. The shift in Raman frequencies with pressure is shown in Figure 4.6 and same has been depicted in Table 4.3.

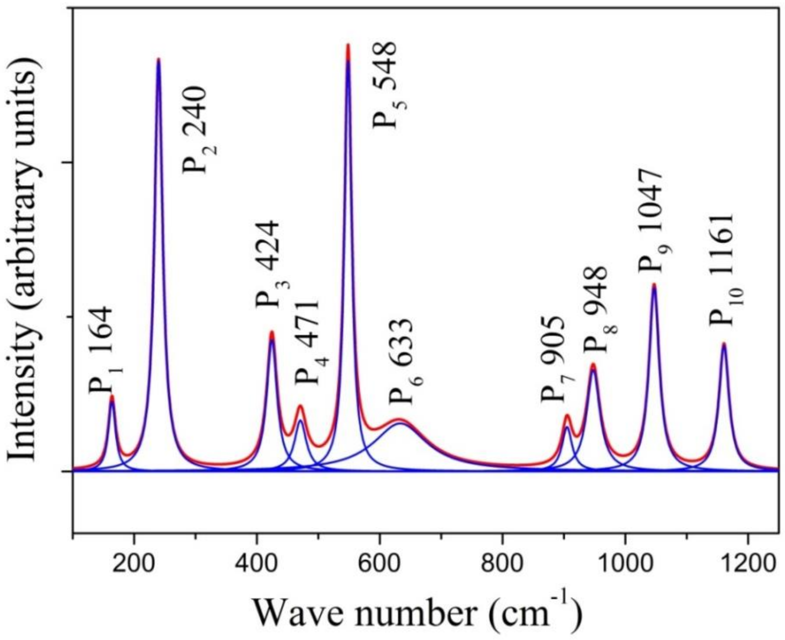

Figure 4.4 Raman spectrum of Cmcm phase of $InPO_4$ at ambient conditions. The observed data is represented by red line. Individual fitted peaks (blue colour) are denoted by symbol P along with their frequency values.

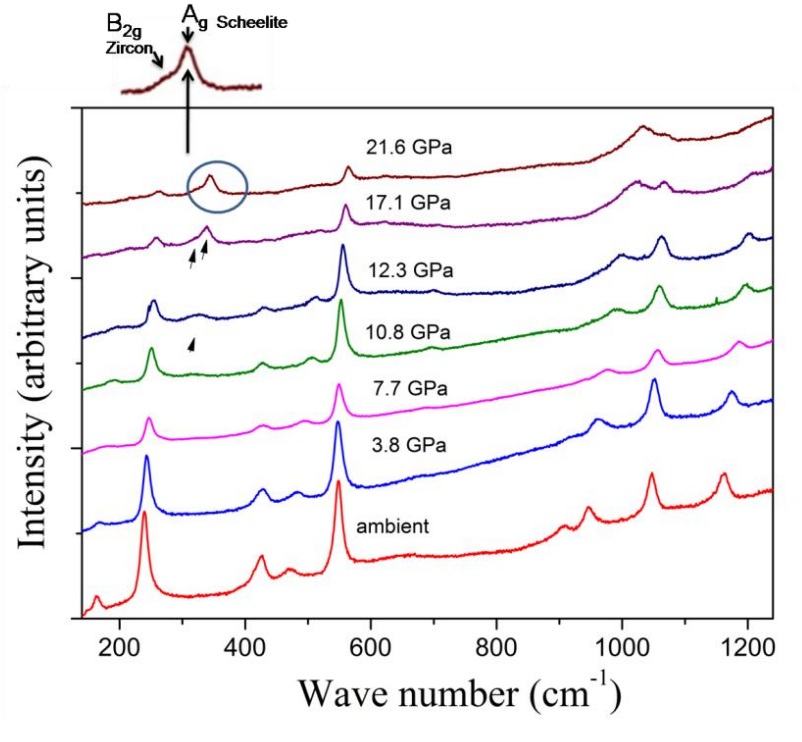

Figure 4.5 Raman spectra of $InPO_4$ at a few selective pressures. The new peaks emerging at high pressure is represented by arrow. The inset show the most intense peak contribution from zircon ($I4_1/amd$) and scheelite ($I4_1/a$) type tetragonal phases.

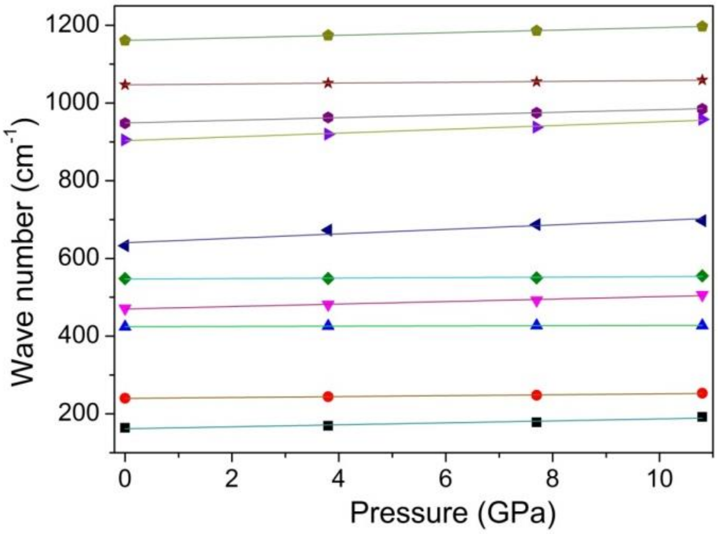

Figure 4.6 Variations in Raman frequencies of Cmcm phase of InPO$_4$ with pressures.

υ (cm^{-1}) **Exp.**	**Mode**	**d υ/dp (Exp.) (cm^{-1}/GPa)**	**υ (cm^{-1})** **Theory**	**d υ/dp (Theory) (cm^{-1}/GPa)**
164	B_{1g}	2.53	181.03	0.03
240	A_g	1.18	234.27	4.37
424	A_g	0.30	407.40	0.45
471	B_{2g}	3.18	448.23	4.64
548	A_g	0.61	516.78	0.64
633	B_{3g}	5.73	638.97	3.47
905	B_{1g}	4.85	871.15	6.28
948	A_g	3.40	912.91	5.44
1047	A_g	1.10	1007.71	1.49
1161	B_{3g}	3.30	1130.50	4.02

Table 4.3 Raman frequencies along with their pressure coefficients of orthorhombic phase of InPO$_4$ at ambient pressure and compared with theoretically determined values[110].

The modes (P_3 and P_5) corresponding to symmetric and asymmetric bending of PO_4 tetrahedra show small rate of variation in Raman frequencies with pressure. This indicates, these modes are least affected by compression. All the modes have been assigned based on previously reported study. The mode at 164 cm^{-1}(from previous study[16]) has been assigned to the B_{1g} translation mode by Moreno et al[110]. However, the mode frequency and pressure coefficient of our P_1 mode (175 cm^{-1}) match well with B_{3g} translation mode assigned from theoretical study[110]. The PTM used is hydrostatic only up to ~10 GPa. Above this pressure, the non-hydrostatic stress causes broadening of the Raman spectra. On further compression to 12.3 GPa, the relative intensities of orthrhombic-$InPO_4$ phase decrease and a new mode emerge after P_2 mode (as shown in Figure 4.5) suggesting structural transition to a new phase. Relative intensities of the new peaks increase with pressure indicating increase in fraction of high pressure phase. On further increase of pressure up to 21.6 GPa, broadening of Raman modes were observed. The modes of ambient *Cmcm* phase of $InPO_4$ persist till the highest pressure achieved in the experiment *i.e.* 21.6 GPa. This indicates that pressure induced phase transition is sluggish at room temperature.

4.5 High pressure X-ray diffraction studies

In order to determine the structural behavior of $InPO_4$ under pressure, high pressure X-ray diffraction studies have been carried out. Figure 4.7 shows measured diffraction patterns at different pressures. With the increase in pressure, the diffraction peaks shift towards higher 2θ values as expected due to lattice contraction and no additional peak appear up to 10.2 GPa.

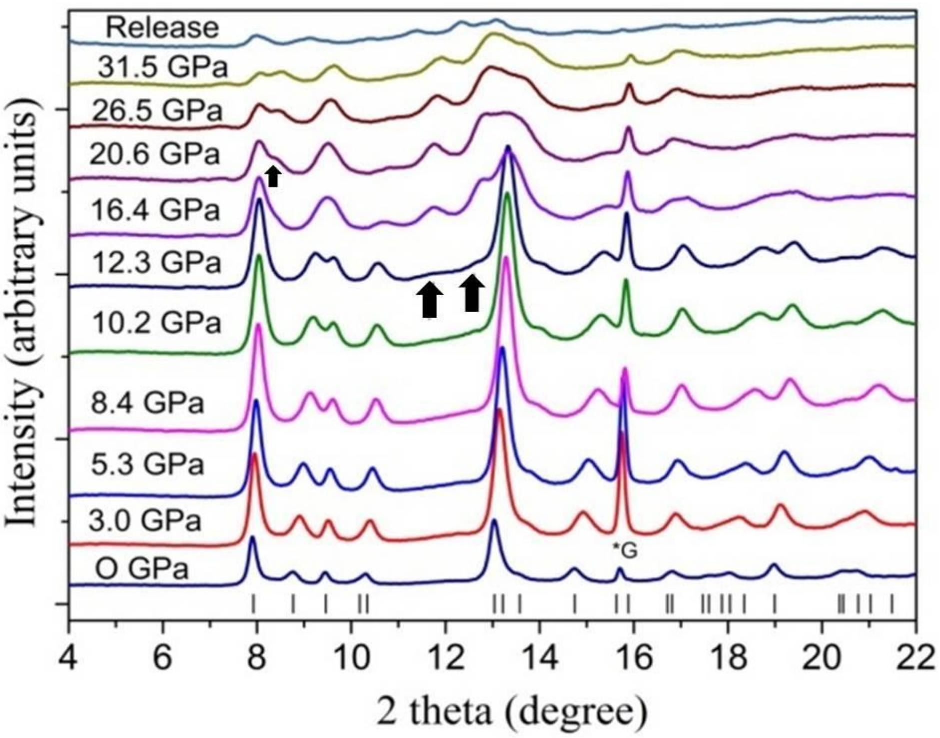

Figure 4.7 X-ray diffraction ($\lambda = 0.6125$ Å) patterns of orthorhombic InPO4 at few selective pressures. Indexing of ambient phase is shown in figure. Diffraction peaks of tungsten gasket is marked by $^{*}G$.

Rietveld refinement results of the observed diffraction patterns indicate that all the three lattice parameters (a, b and c) of orthorhombic phase decrease upon compression. Hanfland et al.[114] have introduced one dimensional analogue of the Murnaghan equation[115] for determination of uniaxial compressibility of the material. The equation is as follows:

$$lp = lo[1 + (P \times \left(\frac{Blo'}{Blo}\right))]^{(-\frac{1}{Blo'})}$$

where, lo is the lattice parameter (a or c) at ambient, lp is the lattice parameter at pressure P , Blo and Blo' are the zero pressure uniaxial bulk modulus and its pressure derivative respectively.

Figure 4.8 shows the variation of lattice parameters of *Cmcm* phase of $InPO_4$ with pressure. $InPO_4$ exhibits anisotropic compression behaviour as indicated by value of uniaxial bulk modulus in Figure 4.8.

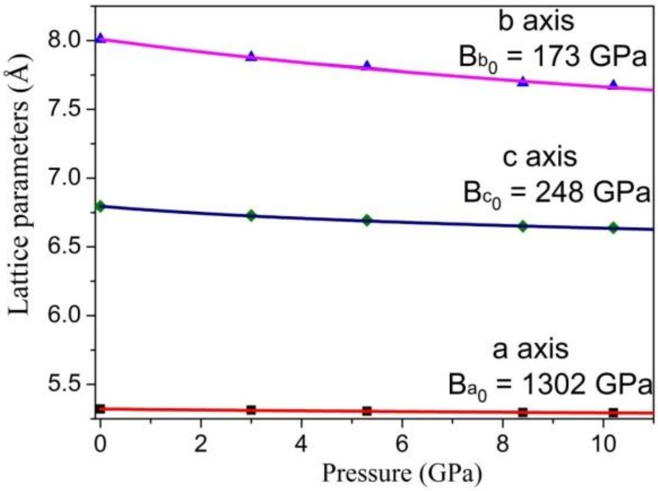

Figure 4.8 Variation of lattice parameters of Cmcm phase of $InPO_4$ with pressure.

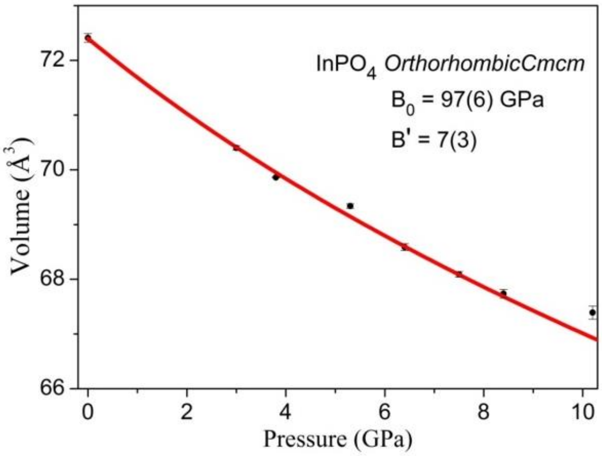

Figure 4.9 Measured volumes per formula unit with pressure are shown by solid symbol and fitted third order Birch-Murnaghan equation of state is shown by solid line (red).

The axis *a* is least compressible while it is easy to compress the structure along *b* axis. As shown in Figure 4.1, the structure consists of InO_6 and PO_4 polyhedra. InO_6 polyhedra have two types of *In-O* bonds. Two apical In-O bonds have longer bond length (2.28 Å at ambient conditions) while four planer *In-O* bond has shorter bond length (1.96 Å at ambient conditions). All the four phosphorous atoms have same bond length (1.52 Å at ambient conditions). Due to strong *P-O* bond and hindered motions of ions, it is difficult to compress the structure along *a* axis. The longer apical *In-O* bond and open structure make *b* axis most compressible.

The non-hydrostatic stress can affect the bulk modulus of the material[116]. Therefore, the bulk modulus of orthrhombic-$InPO_4$ is determined by fitting the third order Birch-Murnaghan equation of state[41] to measured *P-V* data up to 10.2 GPa pressure by using EOSFit7 software[95]. The bulk modulus of orthrhombic-$InPO_4$ is found to be 97 ± 6 GPa as shown in Figure 4.9. The observed bulk modulus of orthrhombic-$InPO_4$ is lower as compared to isostructural $AlPO_4$ and $GaPO_4$ which can be ascribed to more compressibility of In^{3+} ion (Table 4.4).

Compound (*Cmcm* Phase)	**Bulk Modulus B (GPa)**	**Pressure derivative of bulk modulus (B')**
$InPO_4$	97 ± 6	7.1 ± 3.2
$AlPO_4$[53]	118 ± 7	4
$GaPO_4$[54]	144 ± 6	5.2 ± 0.4

Table 4.4 Bulk modulus of Cmcm phase and compared with iso-structural compounds.

On further compression to 12.3 GPa, two new peaks start emerging near 2θ ~12^0. These observations suggest that *Cmcm* phase of $InPO_4$ has undergone a structural phase transition to a new phase. With further increase in pressure, several additional peaks are observed at various 2θ values as indicated with arrows in Figure 4.7 and the intensities of ambient peaks reduce. Our Rietveld refinement of diffraction patterns suggest that at high pressure both the zircon (Space Group $I4_1/amd$) and scheelite (Space Group $I4_1/a$) type tetragonal phases are present along with ambient orthorhombic *Cmcm* phase. The high pressure tetragonal phases are earlier predicted in theoretical studies[110]. The transformation of *Cmcm* phase to zircon and scheelite type tetragonal phases is also reported for $TiSiO_4$[117]. For Rietveld refinement, we have taken the atomic coordinates of high pressure tetragonal phase from theoretical calculations. However, in theoretical studies, Moreno et al. have shown that orthorhombic *Cmcm* phase remains stable up to 6.2 GPa. In the range of 6.2 to 7.5 GPa, zircon type tetragonal phase becomes stable. Further increase in pressure above 7.5 GPa, scheelite type tetragonal structure attains stability. Thus, zircon structure is stable only within a small window of 1.3 GPa. Due to very close energies of these high pressure phases, experimentally both the zircon and scheelite type tetragonal phases were found to coexist up to 31.5 GPa which was the highest pressure of the experiment. This suggests that transformation of zircon phase to scheelite phase may be kinetically hindered. The high pressure phase coexists with ambient orthorhombic *Cmcm* phase which indicates transformation of orthorhombic (*Cmcm*) phase to zircon ($I4_1/amd$) and scheelite ($I4_1/a$) type tetragonal phases is of first order in nature. The Rietveld refined X-ray diffraction patterns of $InPO_4$ at 14.5 GPa is shown in Figure 4.10. In both the zircon and scheelite phases, *In* atom becomes eight coordinated with respect to the oxygen atoms while phosphorous continues to be four coordinated. The schematic representation of zircon and scheelite phases is illustrated in Figure 4.11. The diffraction patterns were Rietveld refined up to 14.5 GPa. On further compression, the width of diffraction peaks increase. This may be due to non-hydrostatic stresses or inherent to the structure. The high pressure tetragonal phases persist on release of pressure which shows that the phase transition from orthorhombic to tetragonal phases is irreversible. In our Raman studies, we have observed two new modes (near 300 cm^{-1}) after 12.3 GPa pressure. These modes have been assigned with the help of previous theoretical high pressure studies of $InPO_4$[110]. These modes may correspond to B_{2g} mode (symmetric bending of PO_4 tetrahedra) of zircon type structure and A_g mode of scheelite type structure respectively[110]. Experimental studies on $TbVO_4$ also show that these modes (B_{2g} mode of zircon and A_g mode of scheelite type structures) are intense modes[118].

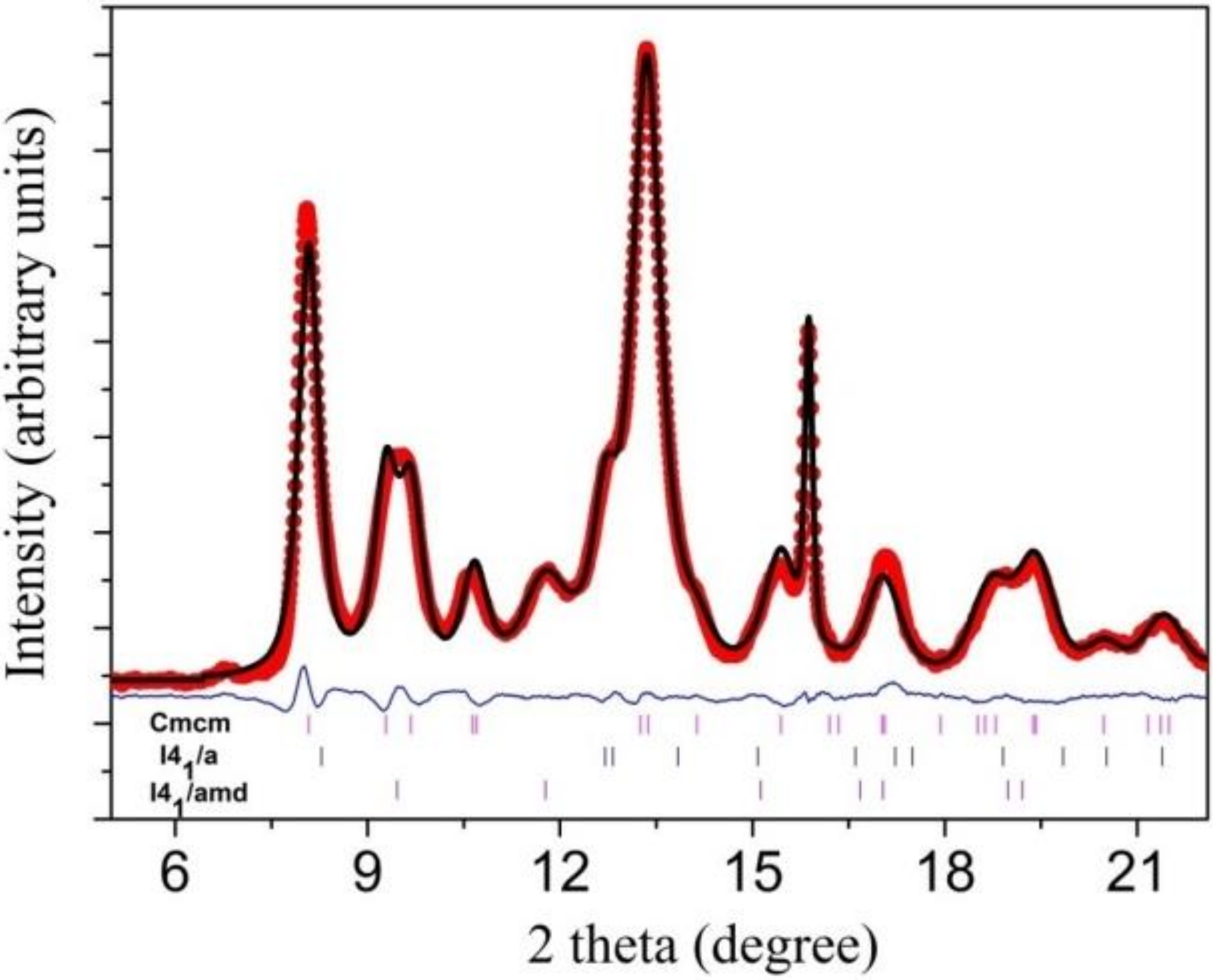

Figure 4.10 Rietveld refined x-ray diffraction pattern of $InPO_4$ *at 14.5 GPa. High pressure tetragonal phases are also present along with ambient orthorhombic Cmcm phase. The observed data points are shown via. red symbols. The calculated data is represented by black line. Blue line shows the difference between observed and calculated data. The goodness of fit parameters are wRp = 0.02, Rp = 0.01 and* $R(F^2)$ *= 0.04. The weight fraction of orthorhombic Cmcm phase (a = 5.308, b = 7.569, c = 6.608) is ~32% while that of tetragonal* $I4_1/a$ *(a = 4.667, c = 10.166) and* $I/4_1/amd$ *(a = 5.970, c = 4.742) phases are ~36% and ~31% respectively.*

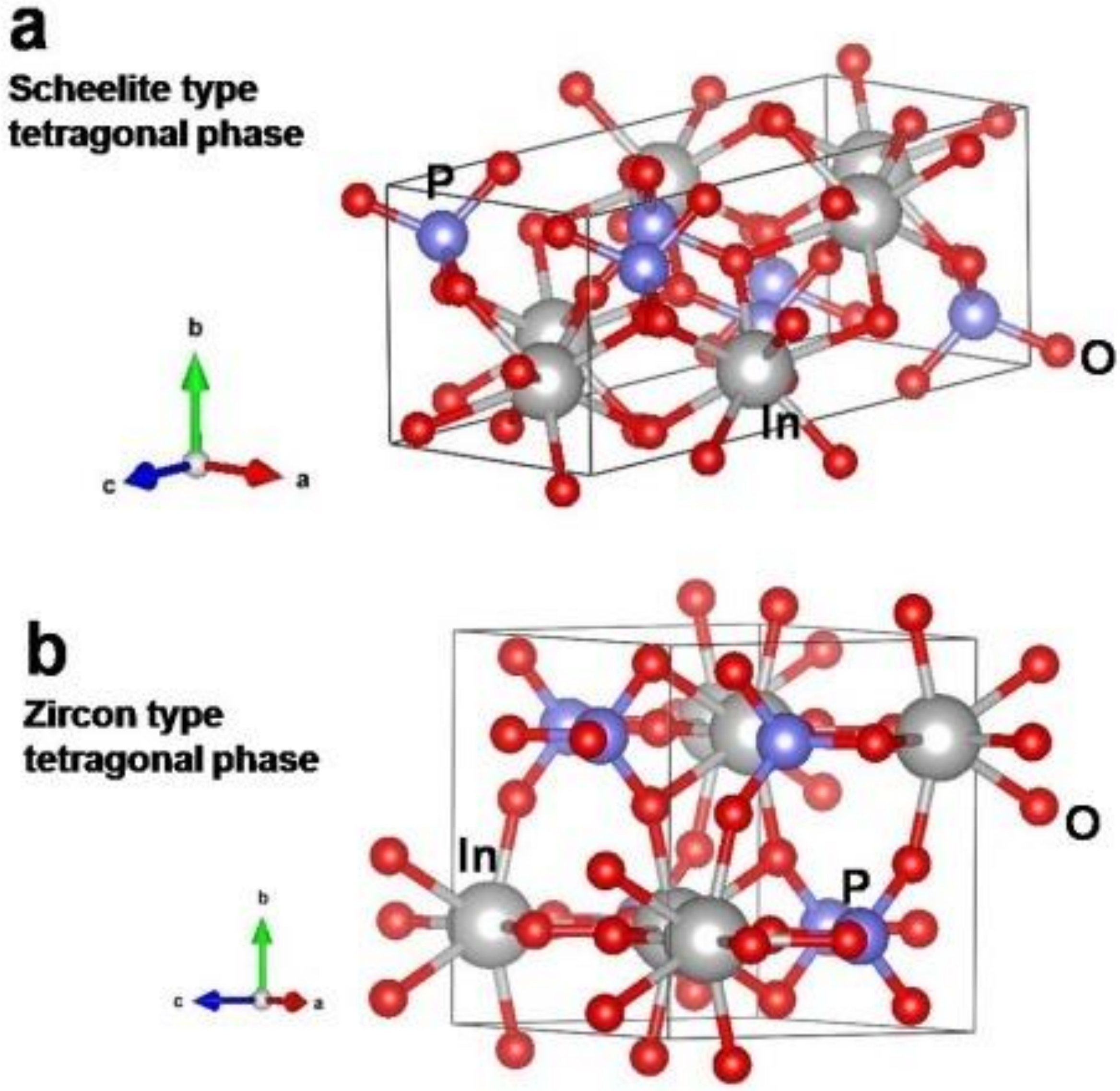

Figure 4.11 The pictorial representation of high pressure phases of InPO₄.

Orthorhombic to tetragonal transition implies ordering of structure with compression, as opposed to commonly observed pressure induced symmetry lowering. In this higher symmetry denser state, the PO_4 tetrahedral rigid units rearrange themselves such that its C_{2v} molecular site symmetry in *Cmcm* phase is transformed a D_{2d} site in Zircon structure and S_4 in the scheelite type structure. The factor group analysis showing correlation of $(PO_4)^{3-}$ site symmetry in each phase has been given in Table 2.

To conclude, in this chapter, I have experimentally shown that under pressure ambient orthorhombic *Cmcm* phase of $InPO_4$ transforms to tetragonal phases having space groups $I4_1/amd$ and $I4_1/a$. Both the high pressure phases are present up to 31.5 GPa which was the highest pressure of the experiment. The structural information may be useful in development of $InPO_4$ based electronic devices.

Chapter 5: High pressure studies on $YInO_3$

5.1 Introduction

Multiferroic compounds have received substantial attention because of their possible applications in memory devices and field-effect transistors[119, 120]. $YMnO_3$ is a well known multiferroic compound which shows magnetic ordering along with ferroelectricity[121, 122]. The conventional ferroelectricity mechanisms based on the presence of d^0 ions or S^2 lone pair ions are unable to explain the ferroelectricity in $YMnO_3$[123, 124]. Van Aken *et al.* have explained that ferroelectricity in this compound arises due to non-centrosymmetric arrangement of the constituent ions in the unit cell. This type of ferroelectricity is named as 'geometric ferroelectricity' which depends merely on tilting of MnO_5 polyhedra and shifting of Y^{3+} ions. In a broader sense, ferroelectricity in $YMnO_3$ depends on the size of constituent ions. The Ga^{3+} and Mn^{3+} ions have almost similar ionic radius, *i.e.* 0.55 Å and 0.58 Å respectively in trigonal bipyramidal coordination[125]. In the case of $YGaO_3$, which is isostructural to $YMnO_3$, Nugroho *et al.*[126] and Zhou *et al.*[127] showed that *Ga* substitution in $YMnO_3$ causes a small change in the ferroelectric curie temperature of the parent compound. In view of the above observations, $YInO_3$ which is isostructural to $YMnO_3$[128], Mn^{3+} is replaced with In^{3+} (ionic radius 0.72 Å), may also exhibit the effect of larger ion on the geometric ferroelectric behaviour. The possible ferroelectricity in $YInO_3$ has been suggested in earlier reports[129]. Tohei *et al*. showed that spontaneous polarization in $RInO_3$ (*R*: Rare Earth) compounds increase with decrease in the size of *R* ion. The decrease in ionic radius *R* or increase in '*B* site' size leads to increase distortion in InO_5 polyhedra[130]. Using pressure which is a pure thermodynamic parameter, one can change the inter-atomic distances and the tilt of InO_5 polyhedra. Therefore, the structural behaviour of $YInO_3$ under high pressure would be very interesting to understand the geometric ferroelectric behaviour in these types of compounds. Apart from technological importance, the high pressure studies on $YInO_3$ compound can help in understanding the structural distortion mechanism observed in $YAlO_3$. The compound $YAlO_3$ is analogous to $MgSiO_3$ which exists in high abundance under Earth's lower mantle. Due to both technological and geological importance, I have performed high pressure Raman scattering and angle dispersive X-ray diffraction studies on hexagonal form of $YInO_3$.

5.2 Sample preparation and characterization

The method of preparation of powdered sample of hexagonal form of $YInO_3$ is described in reference[131]. AR (Analytical Reagent) grade powders of Y_2O_3, In_2O_3 and glycine were used as starting reagents. $YInO_3$ was synthesized by a self-assisted gel combustion route. Y_2O_3 and In_2O_3 were dissolved in diluted HNO_3 in stoichiometric amounts and glycine was used as fuel. The combustion was carried out in fuel-deficient conditions. The solution was slowly evaporated to obtain a gel which on further heating produced voluminous powder. This powder was calcined at 600 ^{o}C for 1 hour in static air to remove extra carbon. The X-ray diffraction pattern of the calcined powder reveals the *C*-type structure (space group: $Ia\overline{3}$). But the diffraction peaks were broad which could be due to nano nature of the compound. The Pictorial view of cubic phase of $YInO_3$ is shown in Figure 5.1. Rietveld refined X-ray diffraction pattern of cubic phase of $YInO_3$ is shown in Figure 5.2. Further heating the sample to 1175 ^{o}C, pure hexagonal $YInO_3$ was obtained[131].

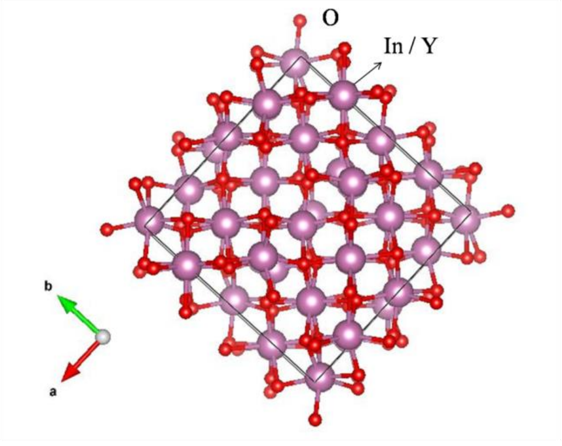

Figure 5.1 Pictorial view of cubic phase of $YInO_3$.

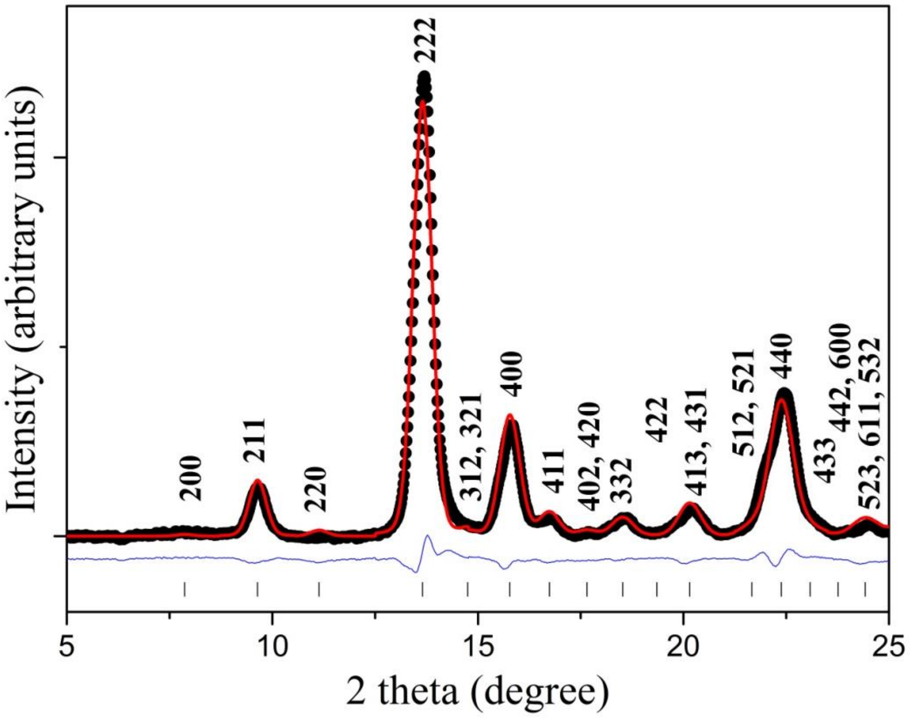

Figure 5.2 Rietveld refined X-ray diffraction (wavelength 0.7107 Å) pattern of cubic phase of $YInO_3$*; a = 10.3598(5) at ambient pressure. Indexing of c-YInO3 phase is shown in figure. Black circles represent observed data points. The calculated data is represented by red line. Blue line shows the difference between 'observed-calculated' data. The goodness of fit parameters are wRp = 0.04, Rp = 0.03 and* $R(F^2) = 0.08$*.*

5.3 Experimental details

High pressure angle dispersive X-ray diffraction (XRD) experiments were carried out on Extreme Conditions X-ray Diffraction (ECXRD) beamline (BL-11) of Indus-2 (synchrotron radiation source, India)[66], using a Mao Bell type diamond anvil cell (DAC). The powdered samples along with gold powder and pressure transmitting medium (Methanol-ethanol) were loaded in a gasket hole of diameter ~ 0.2 mm which was drilled in a pre-indented tungsten gasket. The pressure inside the sample chamber in XRD experiments was determined by diffraction peak of *Au (111)* using known equation of state (EOS) given by Heinz *et al.*[132]. The error in the pressure determination using EOS of gold was less than 0.1 GPa. The XRD experiment on hexagonal phase of $YInO_3$ was carried out using X-ray wavelength of 0.4828

Å up to 29 GPa. The wavelength and the 'sample to detector distance' were refined by diffraction pattern of NIST standards (National Institute of Standards and Technology, USA) CeO$_2$ and LaB$_6$. The diffraction data were collected using MAR345 image plate detector and were converted into one dimensional diffraction profiles with the help of FIT2D software[56]. The diffraction patterns were analyzed using Rietveld refinement method as implemented in GSAS software[58].

Raman spectroscopic measurements were carried out on a Jobin Yvon triple-stage T64000 Raman spectrometer equipped with a Peltier cooled charge-coupled device detector (Synapse) using a 488 nm line of an Ar^+ ion laser for excitation. The laser line was focused on the sample using an optical microscope (Olympus 20X objective lens) connected to the spectrometer. The resolution of collected Raman modes is ~ 3 cm^{-1}. Ruby ball was used to monitor the pressure for Raman scattering experiment[45]. To maintain the hydrostatic pressure conditions, mixture of methanol and ethanol (4:1) was used as a pressure transmitting medium (PTM) in both Raman scattering and X-ray diffraction experiments.

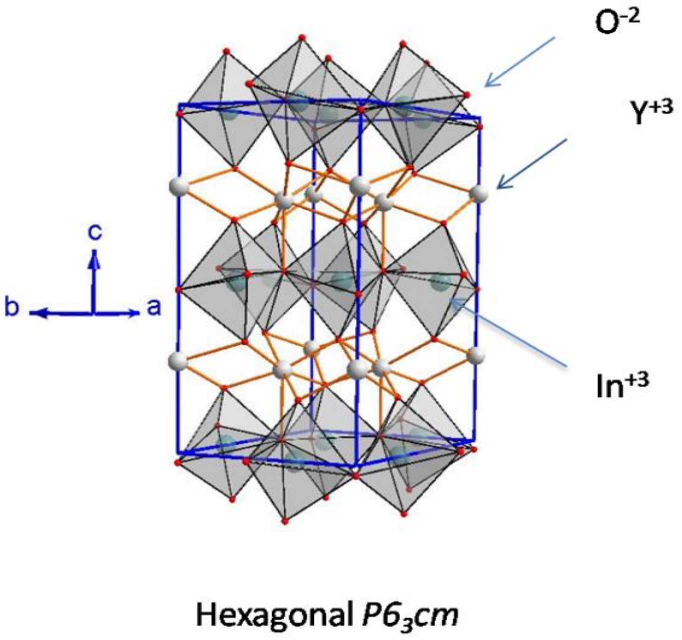

Figure 5.3 Pictorial view of hexagonal phase of YInO$_3$. In the hexagonal phase, Indium ion is coordinated by five oxygen atoms and the Yttrium ion is coordinated by seven oxygen atoms.

Atom	**Wyck. Pos.**	**X** **Exp.**$^{(amb.)}$ **cal.**$^{(0\ GPa)}$	**Y** **Exp.** $^{(amb.)}$ **cal.**$^{(0\ GPa)}$	**Z** **Exp.**$^{(amb.)}$ **cal.**$^{(0\ GPa)}$	**X** **Exp.**$^{(10.7\ GPa)}$ **cal.**$^{(10\ GPa)}$	**Y** **Exp.**$^{(10.7\ GPa)}$ **cal.**$^{(10\ GPa)}$	**Z** **Exp.**$^{(10.7\ GPa)}$ **cal.**$^{(10\ GPa)}$
Y(1)	2(a)	0 **0**	0 **0**	0.2643(19) **0.2675**	0 **0**	0 **0**	0.2633 (10) **0.2679**
Y(2)	4(b)	0.3333 **0.3333**	0.6667 **0.6667**	0.2325(18) **0.2316**	0.3333 **0.3333**	0.6667 **0.6667**	0.2327(12) **0.2311**
In	6(c)	0.3287(21) **0.3334**	0 **0**	0.9884(17) **0.9975**	0.3324(28) **0.3335**	0 **0**	0.9944(14) **0.9970**
O(1)	6(c)	0.3093(15) **0.3044**	0 **0**	0.1755(23) **0.1708**	0.3124 (32) **0.3022**	0 **0**	0.1651(38) **0.1715**
O(2)	6(c)	0.6239(6) **0.6355**	0 **0**	0.3233(9) **0.3262**	0.6411(6) **0.6331**	0 **0**	0.3342(21) **0.3251**
O(3)	2(a)	0 **0**	0 **0**	0.4732 (10) **0.4610**	0 **0**	0 **0**	0.5062 (37) **0.4657**
O(4)	4(b)	0.33333 **0.3333**	0.6667 **0.6667**	0.0354(16) **0.0315**	0.33333 **0.3333**	0.6667 **0.6667**	0.0347(19) **0.0342**

Table 5.1 Experimentally obtained atomic coordinates of hexagonal $P6_3cm$ *phase of* $YInO_3$ *at ambient conditions (a = 6.2730 Å, c = 12.2568 Å) and at 10.7 GPa (a = 6.1791 Å, c = 12.1203 Å). The comparisons with calculated values are shown in bold having lattice parameters: a = 6.2590 Å, c = 12.2250 Å (0 GPa); a = 6.1819 Å, c = 12.1371Å (10 GPa).*

5.4 X-ray diffraction studies on hexagonal phase

At ambient conditions, lattice parameters of hexagonal phase (space group $P6_3cm$) of $YInO_3$ deduced by Rietveld refinement are a = 6.2730(2) Å and c = 12.2568(8) Å, which match well with the earlier reported experimental values, a = 6.2727(1) Å and c = 12.2563(0) Å[133]. The refined atomic coordinates (Table 5.1) also match well with earlier reported experimental values[128]. The structure of hexagonal phase is shown in Figure 5.3.

In order to determine the structural behaviour of $YInO_3$ under pressure, X-ray diffraction studies have been carried out with pressure. Figure 5.4 shows measured diffraction patterns at different pressures. Figure 5.5 represents the Rietveld refined XRD pattern of low pressure hexagonal phase. With the increase in pressure, the diffraction peaks shift towards higher 2θ values as expected due to lattice contraction, albeit without appearance of any additional peaks up to 12 GPa. The pressure transmitting medium (Methanol-ethanol) remains quasi-hydrostatic up to around 10.5 GPa[36]. Therefore, the atomic coordinates of h-$YInO_3$ have been refined up to 10.7 GPa. Above this pressure, the atomic coordinates of h-$YInO_3$ were kept constant to avoid any unphysical refinement while the atomic coordinates of high pressure orthorhombic *Pnma* phase of $YInO_3$ have been deduced from theoretical calculations[134]. Beyond 20.5 GPa, diffraction patterns could not been refined.

Rietveld refinement results of the observed diffraction patterns indicate that both the lattice parameters (*a* and *c*) of hexagonal phase decrease upon compression. The one dimensional analog of the Murnaghan equation[115] is fitted between normalized lattice parameters and pressure *via.* the following equation[114] (Figure5.6).

$$lp = lo[1 + (P \times \left(\frac{Blo'}{Blo}\right))]^{(-\frac{1}{Blo'})}$$

where, lo *is the lattice parameter (a or c) at ambient,* lp *is the lattice parameter at pressure* P *,* Blo *and* Blo' *are the zero pressure uniaxial modulus and its pressure derivative respectively.*

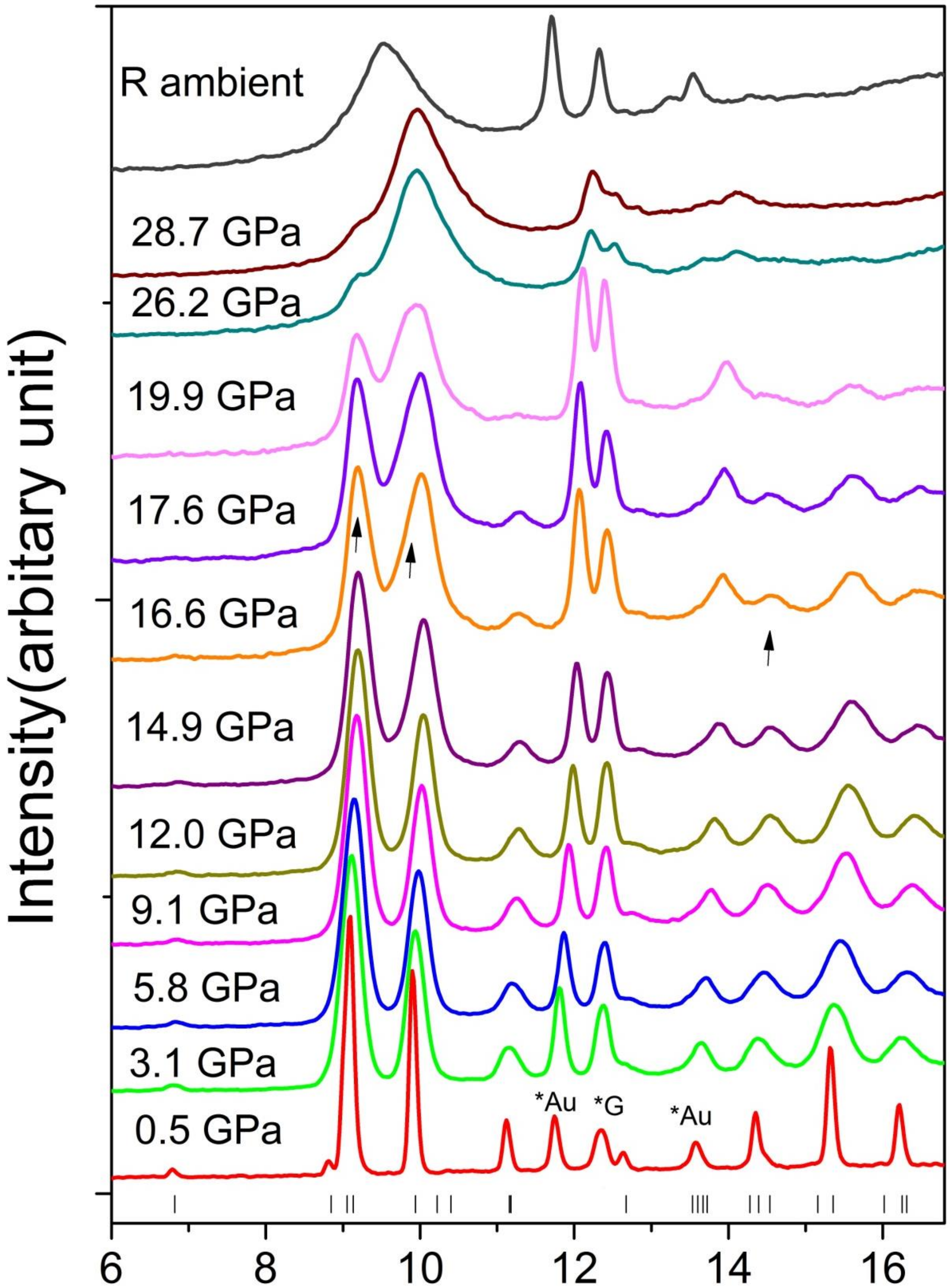

Figure 5.4 X-ray diffraction patterns of hexagonal $YInO_3$ *at few selective pressures. Indexing of ambient hexagonal pressure phase is shown in figure. Diffraction peaks of gold powder and tungsten gasket are marked by* **Au and* **G respectively.*

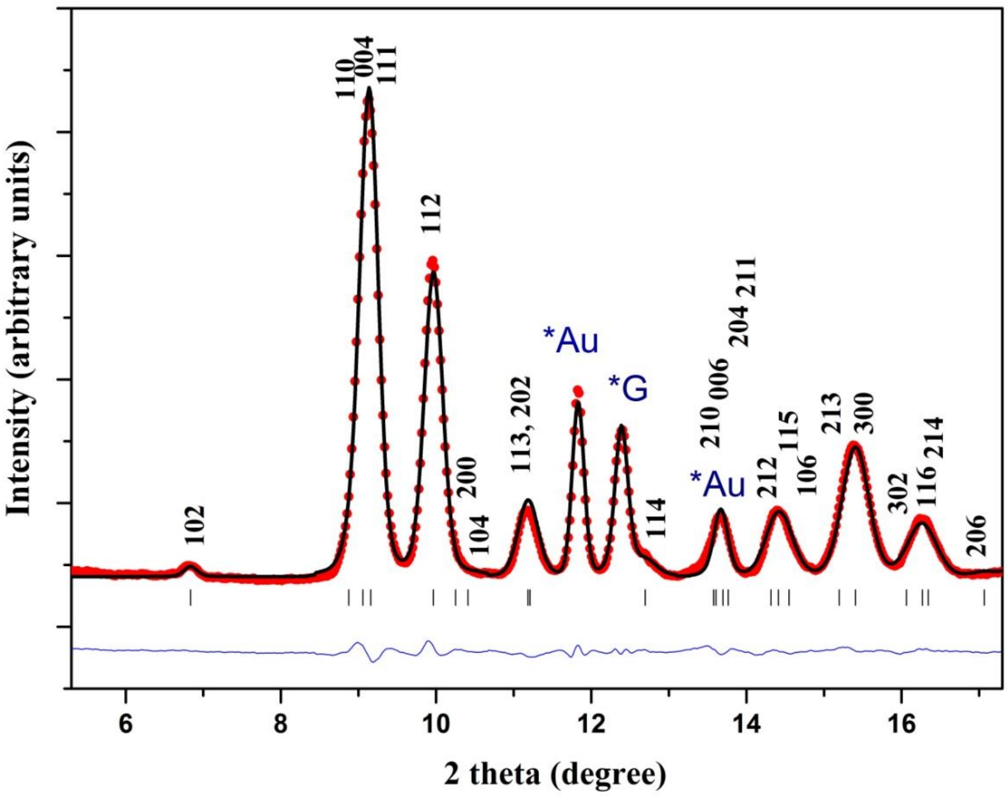

*Figure 5.5 Rietveld refined X-ray diffraction pattern of ambient hexagonal $P6_3cm$ phase of $YInO_3$; a = 6.135(7), c = 12.018(28) at 3.0 GPa pressure. Indexing of h-YInO3 phase is shown in figure. Diffraction peaks of tungsten gasket and gold powder are marked by *G and *Au respectively. Black circles represent observed data points. The calculated data is represented by red line. Blue line shows the difference between 'observed-calculated' data. The goodness of fit parameters are wRp = 0.03, Rp = 0.02 and $R(F^2) = 0.12$.*

The hexagonal phase (*h*) of $YInO_3$ exhibits anisotropic compression behaviour. It has layered structure wherein layers of InO_5 trigonal bipyramids are joined by YO_7 polyhedra through a common oxygen along *c* axis (Figure5.3). Due to open structure along *ab* plane, the rotation of polyhedra occurs more readily in the *ab* plane than along the *c* axis which results in higher compression along the *ab* plane. In fact similar anisotropic compression behaviour has also been observed in several isostructural compounds of *h*-$YInO_3$ *viz.* $AInO_3$ (A = Eu, Gd, Dy)[135] and $BMnO_3$ (B = Y, Ho)[136].

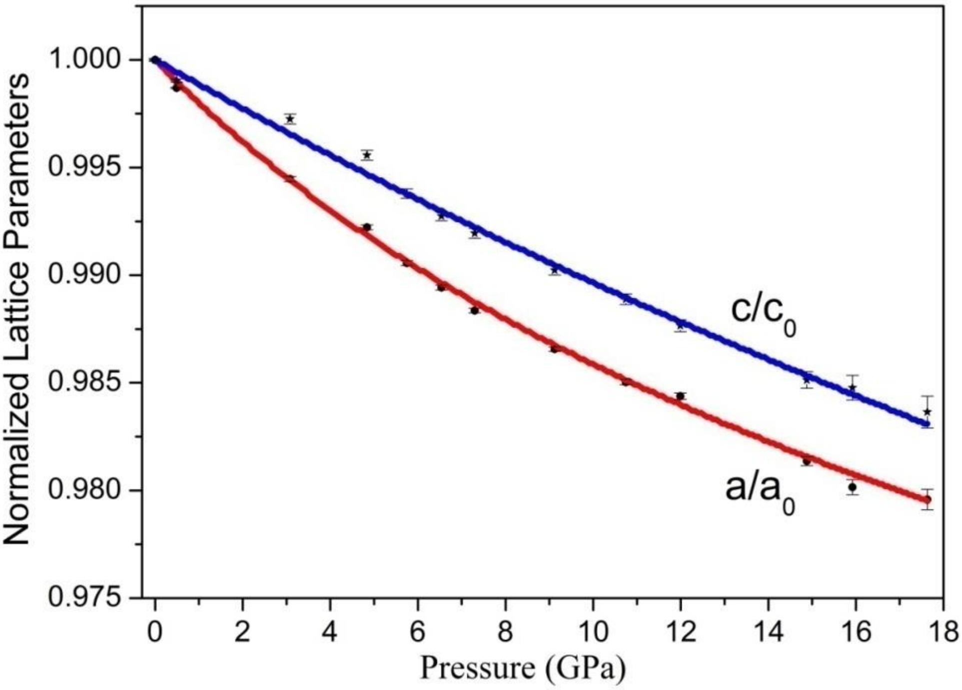

Figure 5.6 Normalized lattice parameters of hexagonal P6$_3$cm phase of YInO$_3$ with pressure are shown by solid symbol and fitted one dimensional analog of the Murnaghan equation of state are shown by solid lines.

Errandonea *et al.* have shown that non-hydrostatic stress can affect the bulk modulus of a material[116]. Therefore, the bulk modulus of *h*-YInO$_3$ is determined by fitting the third order Birch-Murnaghan equation of state[41] to measured *P*-*V* data up to 10.7 GPa pressure by using EOSFit7 software[95]. The bulk modulus of *h*-YInO$_3$ is found to be 194 ± 10 GPa (Figure 5.7).

The first order and second order[137] pressure derivative of bulk modulus are 12 ± 3.2 and -0.3912 GPa^{-1} respectively. Several isostructural compounds of *h*-YInO$_3$ also show large value of first order pressure derivative (B′) of bulk modulus *viz.* YMnO$_3$ (12), HoMnO$_3$ (14), LuMnO3 (26), EuInO$_3$ (21), GdInO$_3$ (11), DyInO$_3$ (19). The Large value of B′ has been ascribed to anisotropic compression behavior in these compounds (Table 5.2)[135, 136].

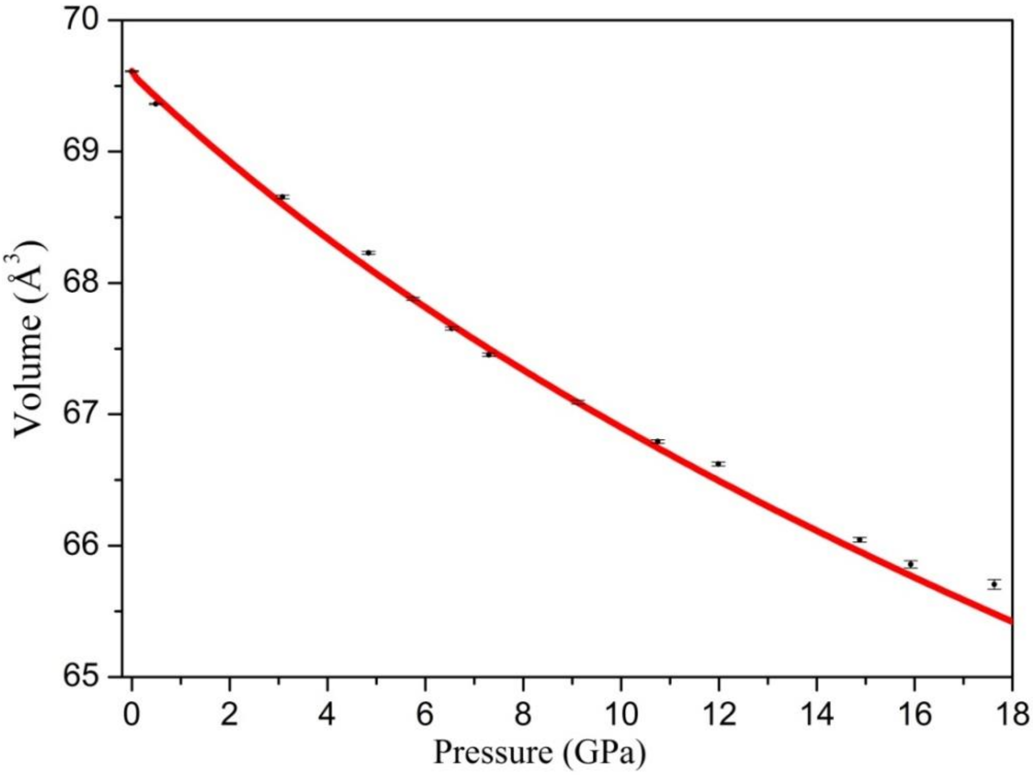

Figure 5.7 Measured volumes per formula unit with pressure are shown by solid symbol and fitted third order Birch-Murnaghan equation of state is shown by solid line (red).

Compound (***P6$_3$cm*** **Phase)**	**Bulk Modulus B (GPa)**	**Pressure derivative of bulk modulus (B$'$)**
YInO$_3$ (Present work)	194 ±10	12.0 ± 3.2
EuInO$_3$	167 ±18	21.0 ± 3.6
GdInO$_3$	177 ±6	11.1 ± 1.7
DyInO$_3$	175 ±15	19.1 ± 3.1
YMnO$_3$	112 ±8	12

Table 5.2 Bulk modulus ***B*** *and its pressure derivative* ***B***$'$ *of AInO$_3$ (A = Y, Eu, Gd, Dy) and YMnO$_3$ compounds.*

The value of bulk modulus of *h*-$YInO_3$ is close to $AInO_3$ (A = Eu, Gd, Dy) compounds due to similar ionic sizes: Y^{3+}(0.96 Å), *Eu* $^{3+}$(1.01 Å) , Gd^{3+} (1.00 Å), Dy^{3+}(0.97 Å)[125]. In contrast to this, the observed bulk modulus of *h*-$YInO_3$ is higher compared to isostructural $YMnO_3$ which can be ascribed to bigger size of In^{3+} ion (Table 5.2).

At 15 GPa, the intensity and width of *h*-(111) diffraction peak (2θ ~10^0) increase as compared to other peaks and Rietveld refinement of diffraction data with *$P6_3cm$* phase was not possible. On further compression to 16.6 GPa, relative intensity of *h*-(111) peak further increases while that of *h*-(112) at 2θ ~9.2^0 and *h*-(115) at 2θ ~14.6^0 peaks reduce. It can be inferred that a new peak emerges and merges with *h*-(111) diffraction peak and these observations suggest that *h*-$YInO_3$ has undergone a structural phase transition to a new phase. Density functional theory (DFT) based calculations with *Vienna ab initio* simulation package (VASP) within the frame work of the projector augmented wave (PAW) approach[102, 103] have also been performed on *h*-$YInO_3$. Local Density Approximation (LDA) method[138] was used for exchange-correlation part of the total energy. For calculations, energy cutoff of plane waves was set to 600 eV and *k* mesh of 18 × 18 × 9 Monkhorst-Pack[105] scheme was used to sample the irreducible part of the Brillouin zone. In the self consistent field (SCF) cycle, the convergence criteria was set to be 10^{-6} eV. The geometric structures have been optimized by minimizing the forces on each atom with the criterion that the total force on it remains below 10^{-2} eV/Å. The details of theoretical calculations are given in reference[134]. The atomic coordinates obtained from theoretical calculations for ambient hexagonal phase are shown in Table 5.1. Refinement of fraction coordinate of low Z atom from experimental data is difficult under pressure. At 10 GPa, difference between calculated and experimentally observed positions of O(3) is ~8.7%. The theoretical studies show that hexagonal phase of $YInO_3$ transforms to orthorhombic *Pnma* phase under pressure. Our Rietveld refined diffraction patterns also suggest that the new high pressure phase of $YInO_3$ may be *Pnma* type orthorhombic phase (atomic coordinates from theoretical calculations, Table 5.3) which coexists with hexagonal $P6_3cm$ phase. The Rietveld refined X-ray diffraction pattern of $YInO_3$ at high pressure (20.5 GPa) is shown in Figure 5.8.

Atom	Wyckoff notation	X	Y	Z
Y	4(c)	0.0748	0.2500	0.9762
In	4(b)	0	0	0.5000
O(1)	4(c)	0.4274	0.2500	0.1524
O(2)	8(d)	0.3141	0.0729	0.6768

Table 5.3 Calculated atomic coordinates of orthorhombic Pnma phase of $YInO_3$ *at 20 GPa having lattice parameters: a = 5.8147 Å, b = 7.7884 Å, c = 5.3806 Å.*

The volume per formula unit for orthorhombic *Pnma* phase is ~2% lower than that of hexagonal $P6_3cm$ phase at 20.5 GPa. Isostructural compounds of $YInO_3$ such as $YMnO_3$, $ErMnO_3$ and $TmMnO_3$ have also shown pressure induced transition to *Pnma* type orthorhombic phase at 23 GPa, 17 GPa and 10 GPa pressure respectively[136, 139, 140].

The pictorial view of orthorhombic *Pnma* phase of $YInO_3$ is shown in Figure 5.9. In the hexagonal phase, each oxygen atom is connected with three In^{3+} in *ab* plane and with one In^{3+} in *z* axis. In the orthorhombic phase of $YInO_3$, each oxygen atom is connected with two In^{3+} ions and the coordination number of In^{3+} ions changes from five to six. Signature of ambient hexagonal $P6_3cm$ phase is noted up to 29 GPa, which is the maximum pressure achieved in this X-ray diffraction experiment. The fact that ambient and high pressure phases coexist suggests that the transition to high pressure phase is of first order in nature.

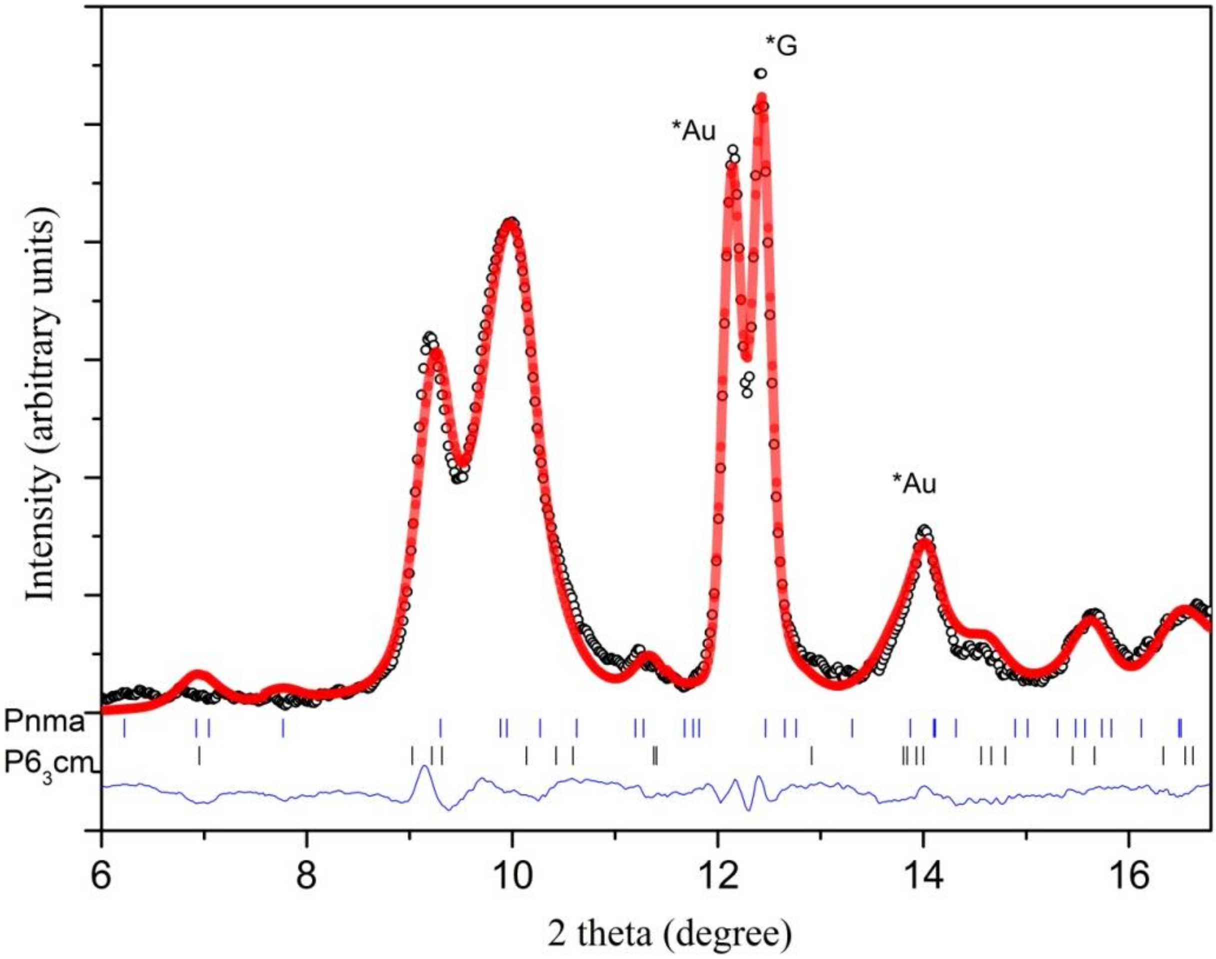

Figure 5.8 Rietveld refined X-ray diffraction patterns of $YInO_3$ *at 20.5 GPa pressure. Diffraction peaks of tungsten gasket and gold powder are marked by *G and *Au respectively. Black circles represent observed data points. The calculated data is represented by red line. Blue line shows the difference between 'observed-calculated' data. The weight fraction of hexagonal* $P6_3cm$ *phase (a = 6.135, c = 12.018) is ~43% while that of orthorhombic Pnma phase (a = 6.009, b = 7.7234, c = 5.5123) is ~57%. The goodness of fit parameters are wRp = 0.03, Rp = 0.03 and* $R(F^2) = 0.13$.

Coexistence of hexagonal $P6_3cm$ phase with orthorhombic *Pnma* phase has already been reported for similar compounds *viz.* $YMnO_3$, $ErMnO_3$ and $TmMnO_3$[136, 139, 140]. These studies show that the phase transition from hexagonal $P6_3cm$ phase to orthorhombic *Pnma* phase is kinetically hindered.

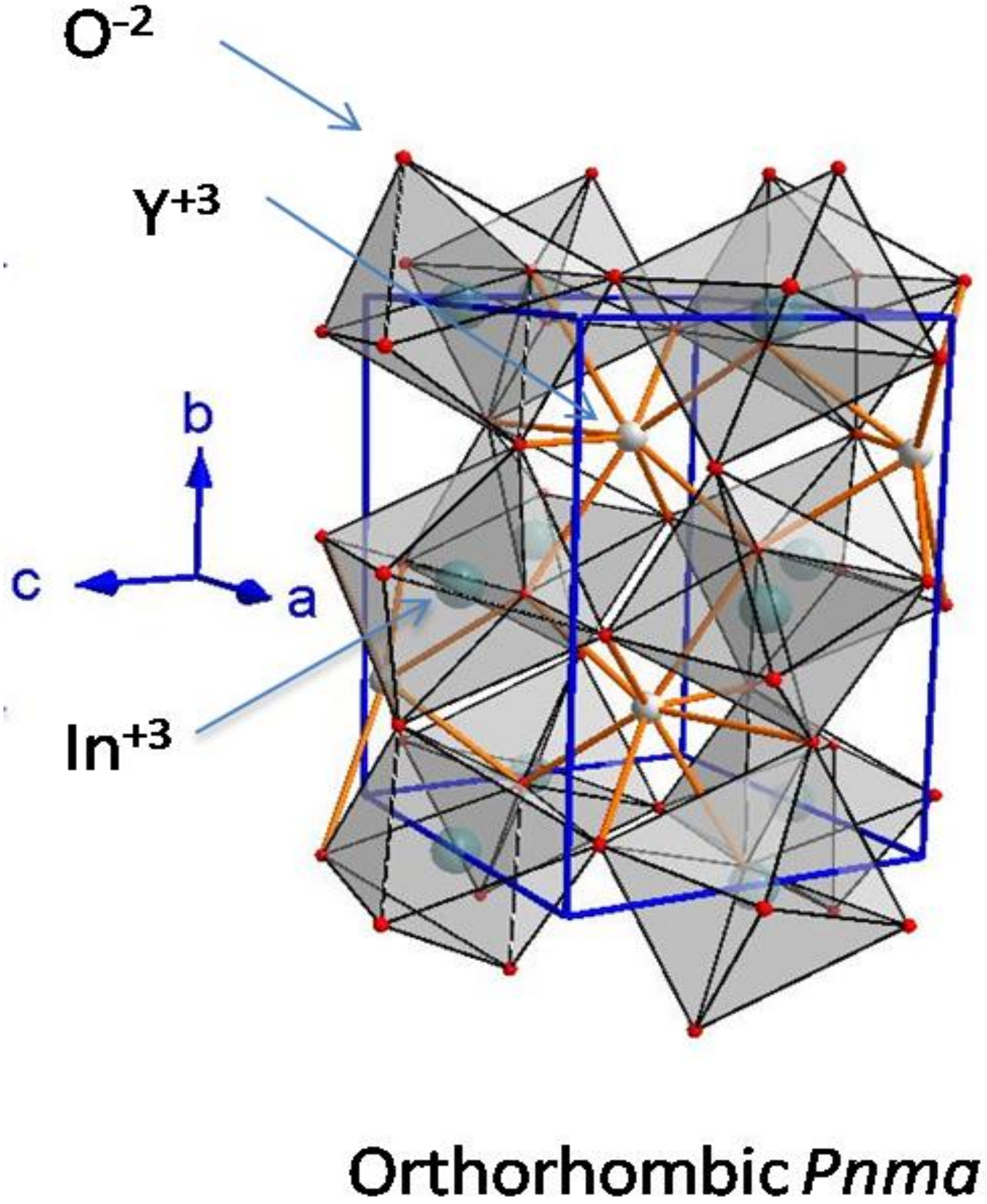

Figure 5.9 The pictorial view of orthorhombic Pnma phase of $YInO_3$.

Therefore, the sample inside the DAC (at 29 GPa) was heated up to ~400^{0}C (limiting temperature in the DAC) for ~10 hours using resistive heating method. However, there was no change observed in the measured diffraction pattern, indicating higher transition barrier. In order to overcome the barrier to achieve complete transformation to orthorhombic *Pnma* phase of $YInO_3$, higher heating temperature may be required.

5.5 Raman scattering studies on hexagonal phase

The unit cell of hexagonal $P6_3cm$ phase of $YInO_3$ contains six formula units. The analysis from group-theory shows that this phase has total 60 Γ point phonon modes[141].

$$\Gamma_{\text{Total}} = 10\ A_{1g} + 5\ A_{2g} + 10\ B_{1g} + 5\ B_{2g} + 15\ E_{1g} + 15\ E_{2g}$$

Out of 60 modes, 38 modes are Raman active [141].

$$\Gamma_{\text{Raman}} = 9\ A_{1g} + 14\ E_{1g} + 15\ E_{2g}$$

The Raman spectroscopic studies on hexagonal $P6_3cm$ phase of $YInO_3$ were performed up to 32.7 GPa at room temperature. At ambient conditions, the Raman modes are observed at 151, 207, 221, 248, 299, 325, 364, 379, 432 and 611 cm^{-1} (named as P_1, P_2….. P_{10} respectively) as shown in Figure 5.10. These modes match well with the earlier reported experimental values[142, 143]. The most intense peak centred at 611cm^{-1}(P_{10}) is A_{1g} mode, which involves symmetric z (coincide with *c* axis) movement of apical oxygen atoms in InO_5 trigonal bipyramid. Iliev *et al.*[144] have reported a similar mode for $YMnO_3$ at 681 cm^{-1}. The large shift in wavenumber may be due to relatively longer *In-O* apical bonds as compared to *Mn-O* bonds[145]. The modes at 364 cm^{-1}(P_7) and 379 cm^{-1}(P_8) are E_{1g} modes which are originated from +x, y ($O_{\text{apical 1}}$); -x, y ($O_{\text{apical 2}}$) movements of apical oxygen atoms in *ab* plane. The modes at 151 cm^{-1}(P_1) mode is assigned as symmetric z stretching of *Y* ions [144].

The observed Raman spectra of hexagonal phase of $YInO_3$ (*h*-$YInO_3$) at a few selective pressures are shown in Figure 5.11. Variation of Raman frequencies with pressure of hexagonal $P6_3cm$ phase of $YInO_3$ is shown in Figure 5.12. The rate at which Raman frequencies vary with pressure is shown in Table 5.4.

With increase in pressure, all the Raman modes monotonously shifted to higher wave numbers up to 17.4 GPa suggesting the persistence of the ambient hexagonal phase up to 17.4 GPa. On further compression to 20.4 GPa, the relative intensities of *h*-$YInO_3$ phase decrease and two new broad modes emerge close to P_8 and P_{10} modes suggesting structural transition

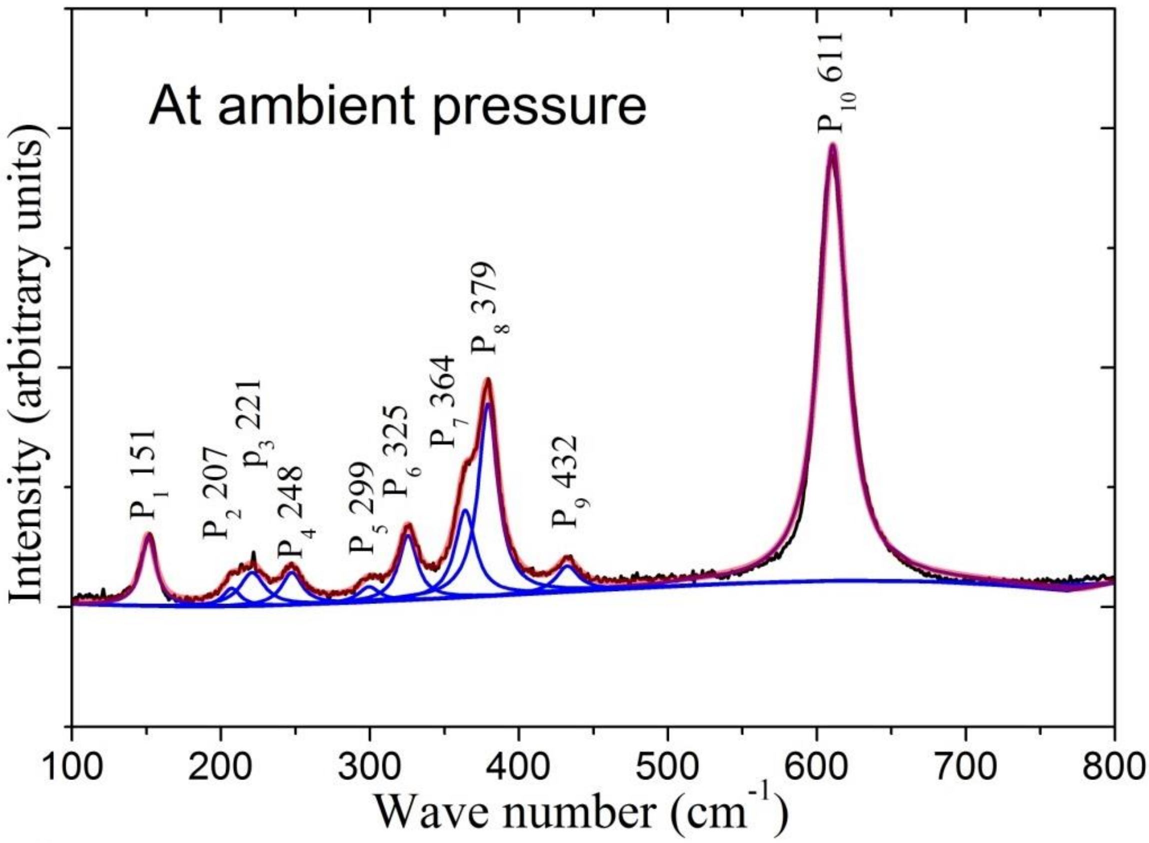

Figure 5.10 Raman spectra of h-YInO$_3$ *at ambient condition. Black line represents observed data while the fitted data is represented by red line. Each individual peak is shown by blue line.*

to new phase. The reduction of P_8 and P_{10} modes to lower wave numbers suggest that the coordination of *In* atom increases across the transition. Our XRD studies also show that under pressure, hexagonal phase of $YInO_3$ has transformed to orthorhombic (*Pnma*) phase in which coordination of *In* atom increases. Relative intensities of these new peaks increase with pressure indicating increase in fraction of high pressure phase. On further increase of pressure up to 32.7 GPa, broadening and diminishing in intensities of Raman modes were observed. This could be due to structural distortion of constituent polyhedra. The strongest mode of hexagonal $P6_3cm$ phase (P_{10} mode) persists till the highest pressure achieved in the experiment *i.e.* 32.7 GPa. This indicates that pressure induced phase transition is sluggish at room temperature. On releasing the pressure from the sample, only broad bands remain, which indicates that the phase transition is irreversible.

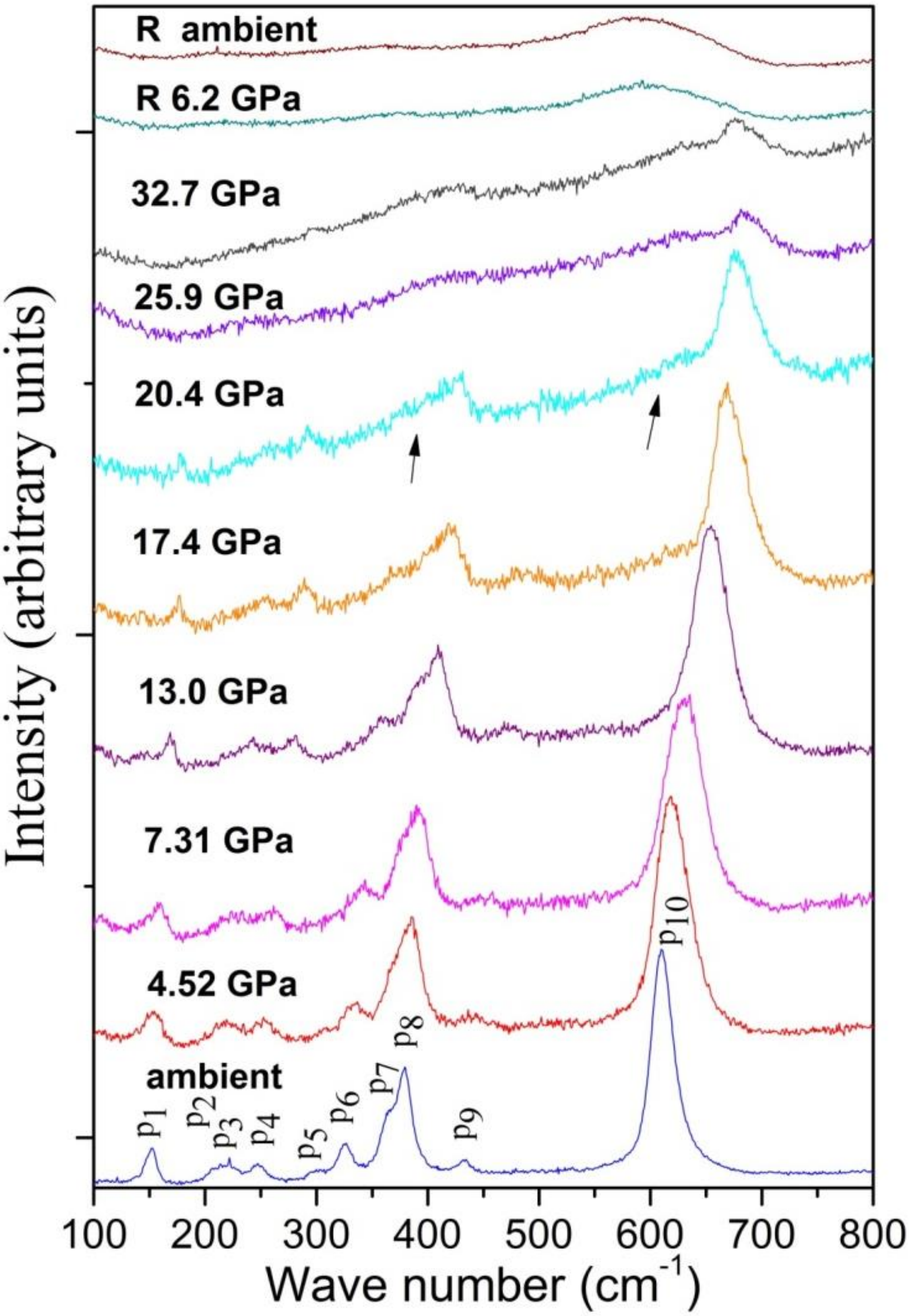

Figure 5.11 Raman spectra of h-YInO$_3$ at a few selective pressures. The mixture Methanol-Ethanol (4:1) was used as a pressure transmitting medium.

υ (cm^{-1}) Exp.	Mode	d υ/dp (Exp.) (cm^{-1}/GPa)	υ (cm^{-1}) Theory	d υ/dp (Theory) (cm^{-1}/GPa)
151	A_{1g}	1.2	150.9	0.95
207	E_{2g}	1.1	212.8	1.3
221	A_{1g}	1.7	227.3	1.6
248	A_{1g}	2.5	237.3	2.5
299	A_{1g}	0.8	289.9	2.7
325	A_{1g}	2.6	318.9	3.2
364	E_{1g}	2.4	362.4	2.8
379	E_{1g}	2.5	377.3	2.4
432	A_{1g}	4.0	438.3	2.3
611	A_{1g}	3.5	610.2	3.3

Table 5.4 Raman frequencies of hexagonal $P6_3cm$ phase of $YInO_3$ at ambient pressure and compared with theoretically determined values.

In order to identify weak Raman modes, Density Functional Perturbation Theory (DFPT) based calculations have also been performed on high pressure orthorhombic phase. The details of these theoretical calculations are given in reference[134] .The calculated Raman frequencies are shown in Figure 5.13. In our experimental Raman studies on hexagonal $YInO_3$, I have found that two new broad bands (~378 and 625 cm^{-1}) appeared at 20.4 GPa which correspond to calculated intense A_g modes of orthorhombic *Pnma* phase.

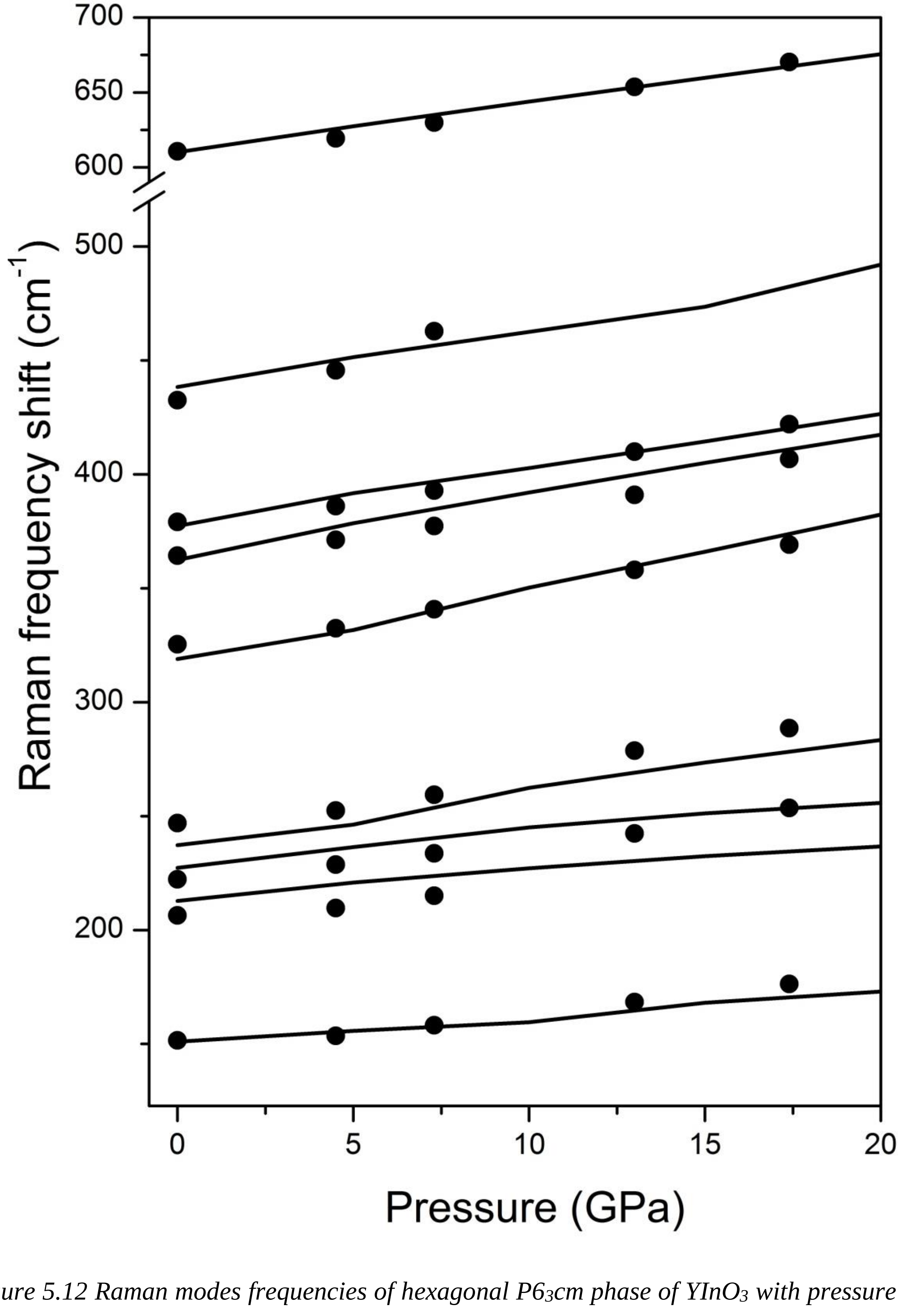

Figure 5.12 Raman modes frequencies of hexagonal P6$_3$cm phase of YInO$_3$ with pressure are shown. The methanol-ethanol (4:1) is used as pressure transmitting medium. The solid spheres represent observed data points. The calculated data points are shown via. solid lines.

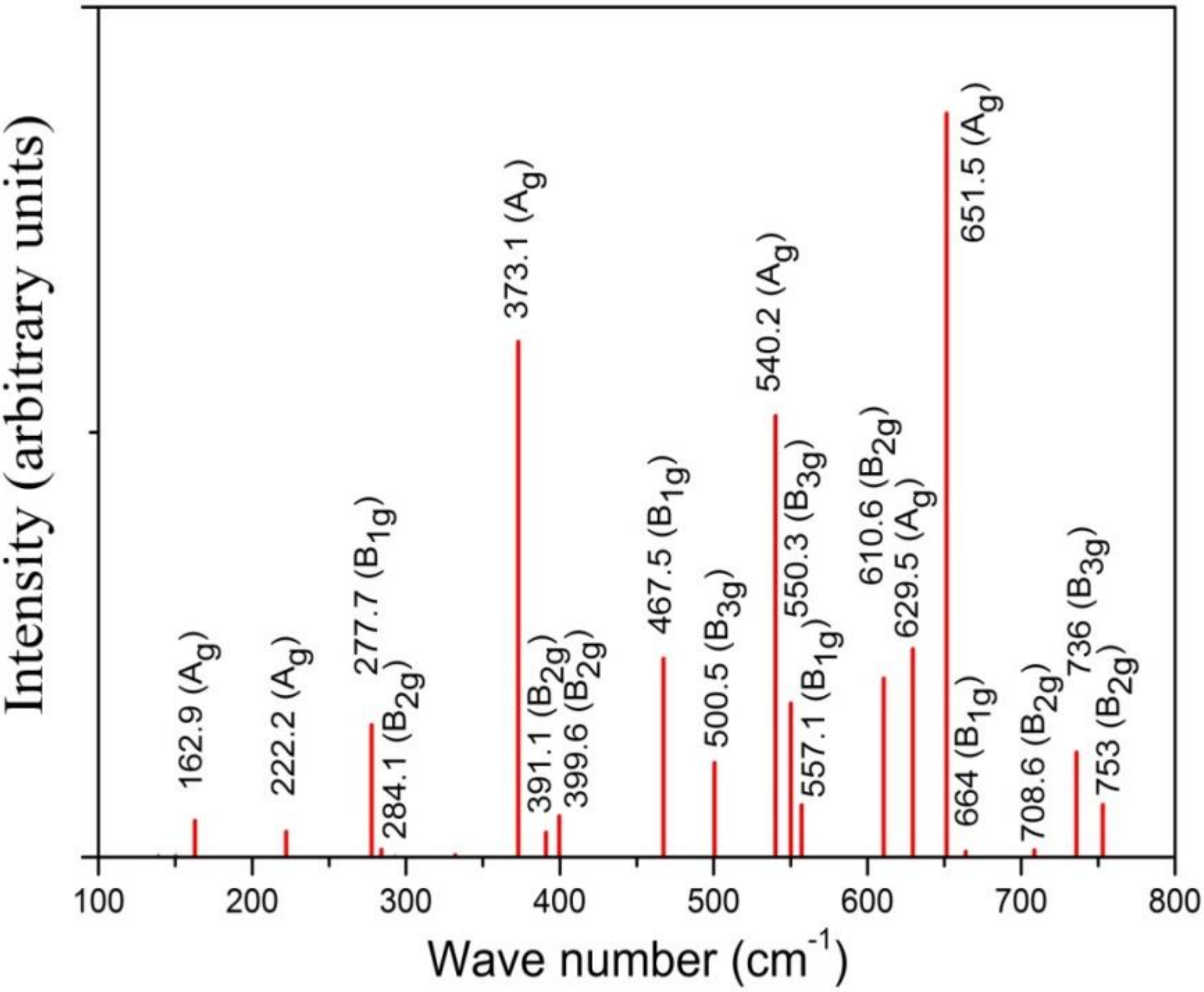

Figure 5.13 Theoretically determined Raman modes frequencies of Orthorhombic Pnma phase of $YInO_3$ *at 20 GPa.*

5.6 Phase stability of cubic phase under high pressure

As mentioned in the section 5.2, heating of the cubic phase (space group: $Ia\bar{3}$) of $YInO_3$ to 1175 ^{o}C, hexagonal phase of $YInO_3$ is obtained. The XRD pattern of cubic phase which is formed at 600 ^{o}C, shows nano nature of the compound. Further heating of the sample to 1000 ^{o}C, the width of the diffraction peaks reduce. The Rietveld refinement of this sample is shown in Figure 5.14.

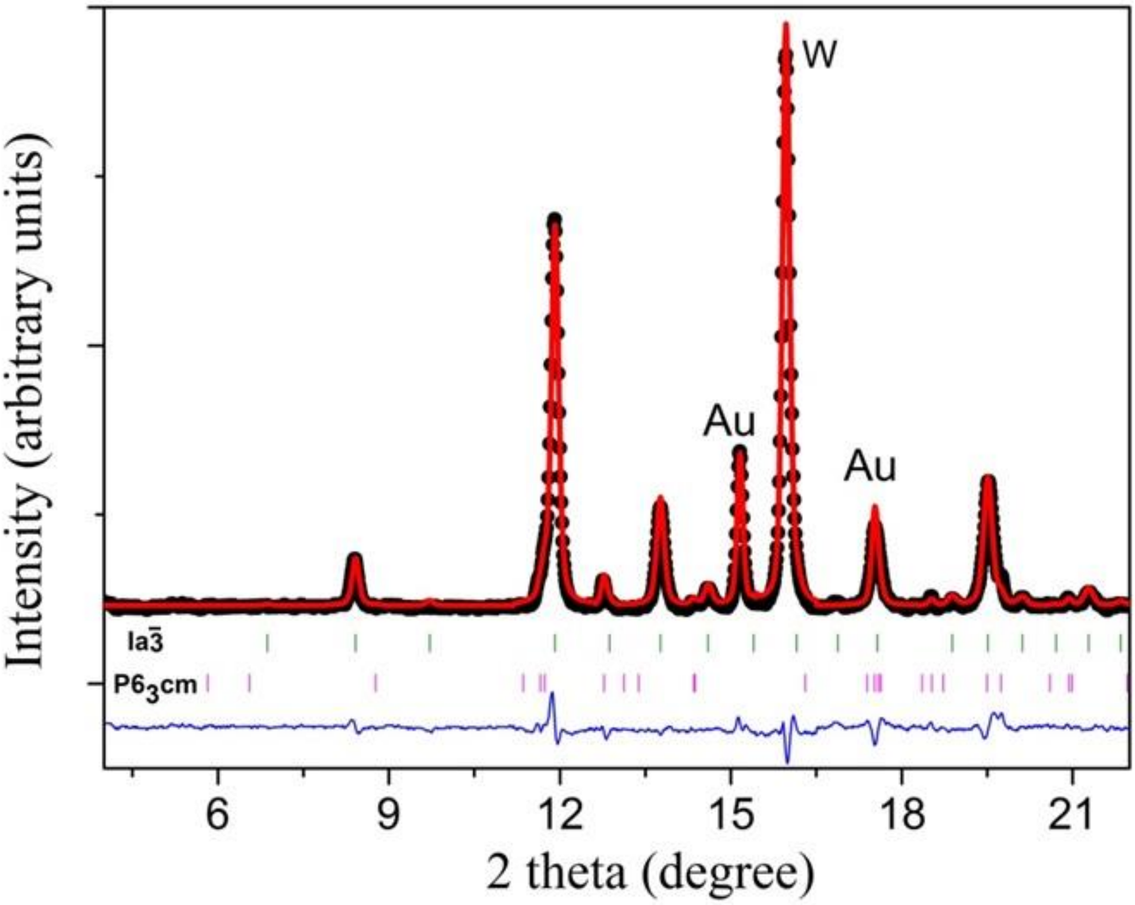

Figure 5.14 Rietveld refined X-ray diffraction patterns (λ = 0.6207 Å) of $YInO_3$ *at 0.6 GPa pressure with lattice constant a = 10.3509(3). Diffraction peaks of tungsten gasket and gold powder are marked by W and Au respectively. Black circles represent observed data points. The calculated data is represented by red line. Blue line shows the difference between 'observed-calculated' data. The weight fraction of hexagonal* $P6_3cm$ *phase is ~5%. The goodness of fit parameters are wRp = 0.03, Rp = 0.02 and* $R(F^2) = 0.12$.

I have carried out two sets of high pressure XRD experiments on the cubic phase of $YInO_3$ which was heated to 1000 °C. The first experiment was performed up to 18 GPa with $\lambda = 0.6207$ Å. The second experiment was performed up to 28 GPa with $\lambda = 0.4828$ Å. X-ray diffraction patterns of cubic $YInO_3$ (c-$YInO_3$) at few selective pressures obtained in first experiment is shown in Figure 5.15.

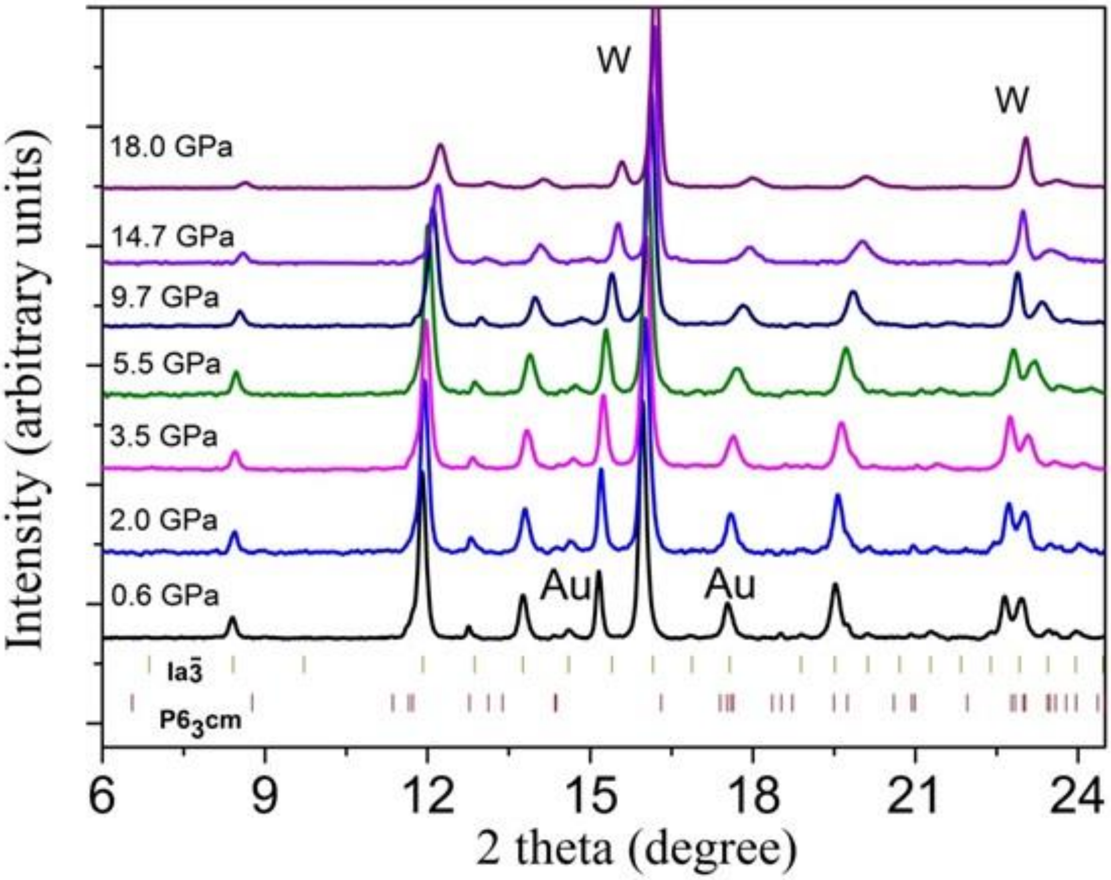

Figure 5.15 X-ray diffraction patterns (λ = 0.6207 Å) of cubic $YInO_3$ at few selective pressures. The weight fraction of high temperature hexagonal phase was ~5%. Diffraction peaks of gold powder and tungsten gasket are also mentioned.

With the increase in pressure, the diffraction peaks shift towards higher 2θ values as expected due to lattice contraction, albeit without appearance of any additional peaks up to 18 GPa. This implies that the cubic phase remains stable up to 18 GPa. The bulk modulus of *c*-$YInO_3$ is determined by fitting the second order Birch-Murnaghan equation of state[41] to measured *P*-*V* data by using EOSFit7 software[95]. The bulk modulus of *c*-$YInO_3$ is found to be 167 ± 9 GPa (Figure 5.16) which is the average of *c*-Y_2O_3 (*i.e.* 144 GPa), *c*-In_2O_3 (*i.e.* 173 GPa).

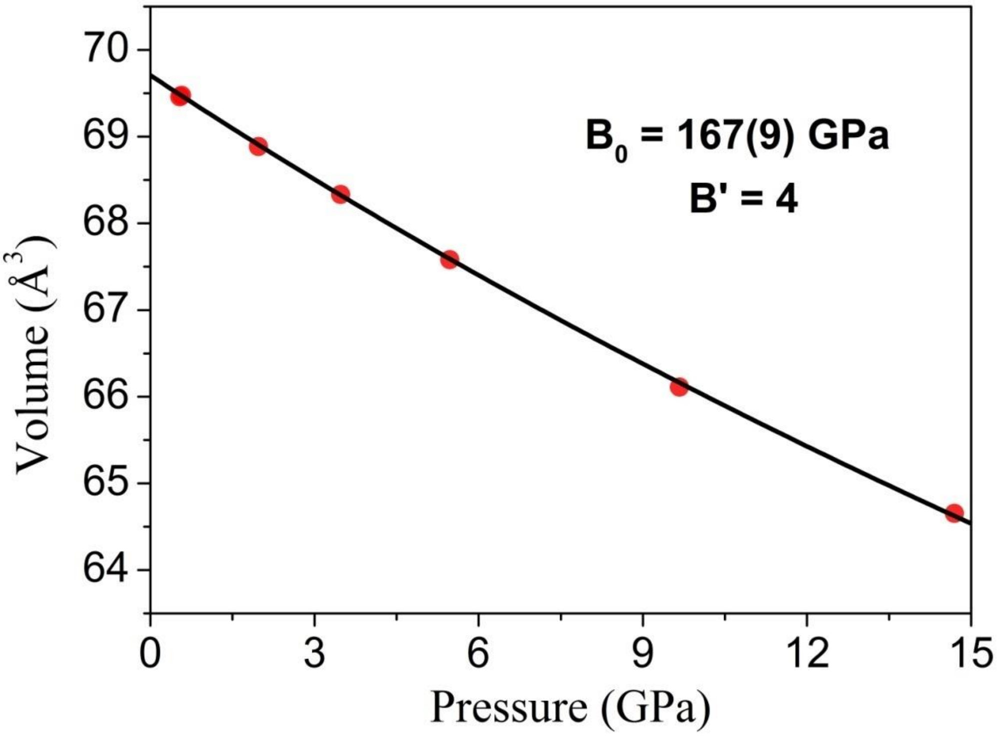

Figure 5.16 Measured volumes per formula unit with pressure of cubic $YInO_3$ *are shown by solid symbol and fitted second order Birch-Murnaghan equation of state is shown by solid line (red). The errors in volumes are well within the size of symbols.*

To explore the structural behavior of cubic phase at higher pressures, we have performed second set of XRD experiment up to 28 GPa. X-ray diffraction patterns of cubic $YInO_3$ at few selective pressures obtained in second experiment are shown in Figure 5.17. Similar to first experiment, no additional diffraction peak was observed up to 17 GPa. With further increase in pressure to 19 GPa, few new diffraction peaks emerge and these observations suggest that *c*-$YInO_3$ has undergone a structural phase transition to a new phase. With further increase in pressure up to 28 GPa, the intensities of these new peaks increase while that of ambient phase reduce. Our Rietveld refinements of diffraction patterns suggest that at high pressure the orthorhombic (Space Group *Pnma*) phase is present along with ambient cubic phase. The Rietveld refined XRD data of 25.8 GPa pressure is shown in Figure 5.18. The drop in volume per formula unit from cubic to orthorhombic phase transition was ~ 6.7% at 25.8 GPa. In the previous high pressure studies on hexagonal phase of $YInO_3$, transformation of hexagonal phase to orthorhombic phase was observed in the pressure range of 12 GPa-15 GPa[134]. However, in the present high pressure study on cubic phase of $YInO_3$, signature of orthorhombic phase is observed at 19 GPa.

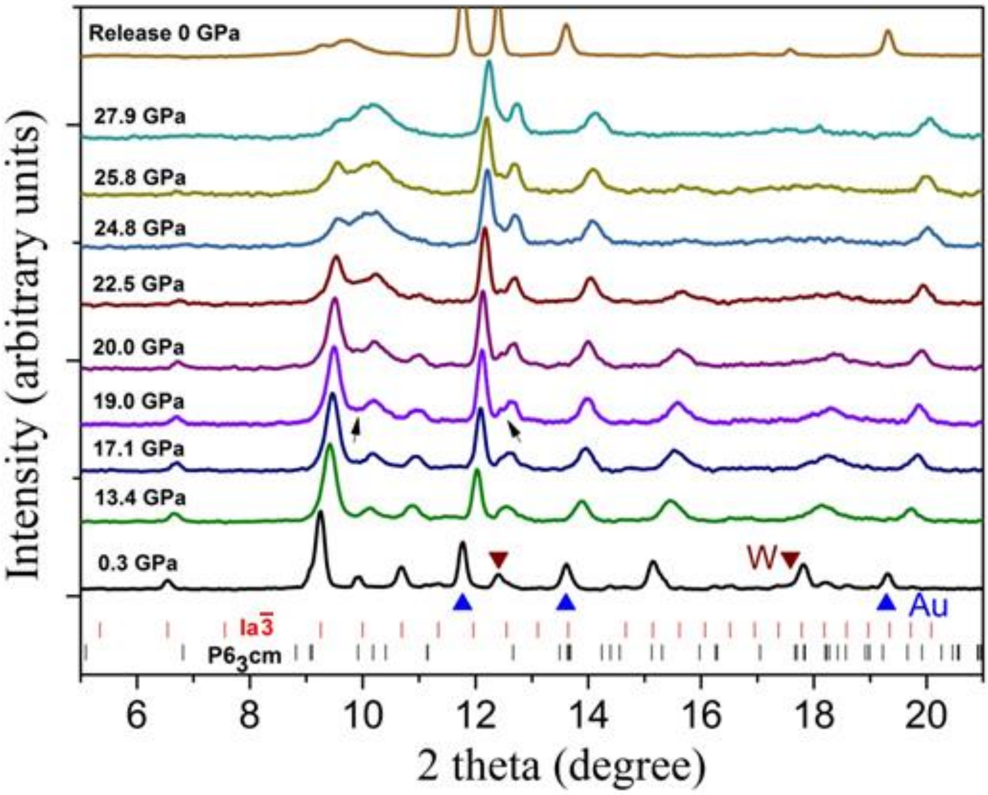

Figure 5.17 X-ray diffraction patterns (λ = 0.4828 Å) of cubic $YInO_3$ at few selective pressures. The weight fraction of high temperature hexagonal phase was ~5%. Diffraction peaks of gold powder and tungsten gasket are also mentioned.

The ambient cubic phase persists up to 28 GPa along with high pressure orthorhombic phase which shows that the transformation of cubic to orthorhombic phase is of first order in nature. The high pressure orthorhombic phase remains even after releasing the pressure which shows transformation of cubic to orthorhombic phase is irreversible.

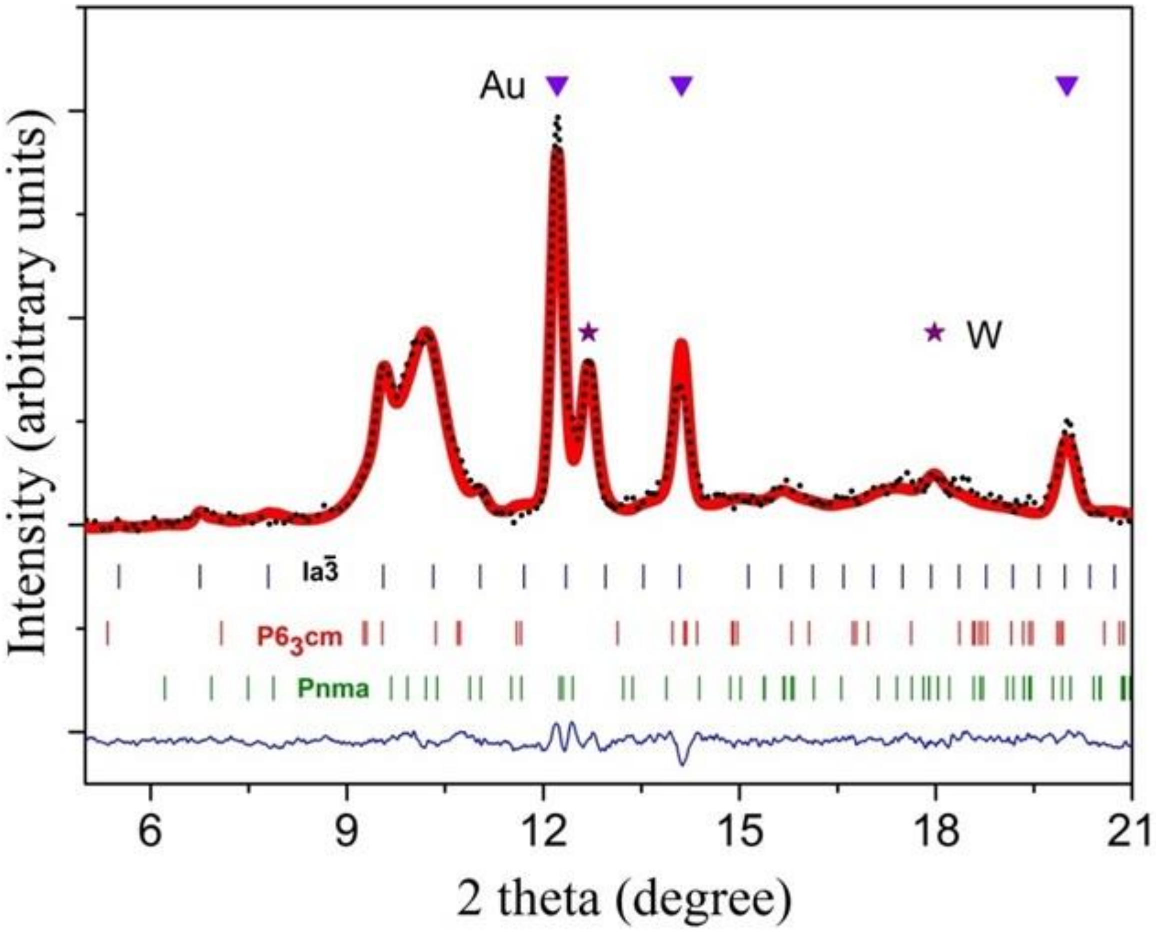

Figure 5.18 Rietveld refined X-ray diffraction pattern ($\lambda = 0.4828$ Å) of cubic $YInO_3$ at 25.8 GPa pressure with lattice constant $a = 10.037(4)$. Diffraction peaks of tungsten gasket and gold powder are marked by W and Au respectively. Black circles represent observed data points. The calculated data is represented by red line. Blue line shows the difference between 'observed-calculated' data. The weight fraction of high pressure orthorhombic Pnma phase is ~44%. The lattice parameters of orthorhombic phase is $a = 5.711(19)$, $b = 7.391(11)$, $c = 5.588(8)$. The goodness of fit parameters are $wRp = 0.02$, $Rp = 0.01$ and $R(F^2) = 0.08$.

In the phase transformation of cubic phase to orthorhombic phase, the coordination number of Indium ion remains same while the coordination number of yttrium ion changes from six to eight.

To conclude, in this chapter, I have shown that both the hexagonal and cubic phases of $YInO_3$ show transformation to orthorhombic phase under pressure. The high pressure studies on $YInO_3$ may be useful to understand the geometric ferroelectric behaviour of $YMnO_3$ type multiferroic compounds.

Chapter 6: Summary and Conclusions

This thesis explores pressure induced structural phase transitions in some polyhedral compounds of Group 3A, such as $Al_{0.5}Ga_{0.5}PO_4$, $InPO_4$ and $YInO_3$, which are of technological and geological importance. High pressure X-ray diffraction studies of the materials have been carried out on Extreme Conditions X- ray Diffraction (ECXRD) beamline[66] at Indus -2 which is an indigenously developed Indian Synchrotron beamline[63]. Various software programs for different aspects of the ECXRD beamline have been developed using Visual Basic 6.0 software language and were implemented so that ECXRD beamline can be remotely operated with the help of a computer. The developed software program for alignment of diamond anvil cell[1] has made the alignment process fast and accurate.

The α-cristobalite (orthorhombic $C222_1$) form of $Al_{0.5}Ga_{0.5}PO_4$[107] which has four co-ordinated Al or Ga atoms transforms to orthorhombic *Cmcm phase* (having six co-ordinated Al or Ga atoms) under hydrostatic conditions using neon as a pressure transmitting medium (PTM). While, under non-hydrostatic conditions (without any PTM) a new monoclinic phase $P2_1$ is observed, which contains layers of both six and five coordinated Al or Ga atoms. In both hydrostatic and non-hydrostatic pressure conditions, the high pressure phases (orthorhombic *Cmcm* and monoclinic $P2_1$) co-exist with the ambient phase suggesting the transformation is of first order in nature. The emergence of a distinct phase under non-hydrostatic stress is a remarkable effect and shows that non-hydrostatic stress plays an important role in the high pressure polymorphism of α–cristobalites. $Al_{1-x}Ga_xPO_4$ is used in piezoelectric resonators[92]. Hence, this study could be useful in the formation of new piezoelectric resonator materials. Apart from the technological applications, several phosphates of Group 3A, such as $AlPO_4$, $GaPO_4$ and $Al_{0.5}Ga_{0.5}PO_4$ are isoelectronic analogous of silica and form isostructural compounds. High pressure investigations on these materials can help in understanding the mechanism of various transformations observed in silica[83, 84] which is the major constituent of the Earth's crust and mantle[79]. $InPO_4$ crystallizes in the orthorhombic *Cmcm* phase at ambient conditions and this is the high pressure phase of $Al_{0.5}Ga_{0.5}PO_4$. $InPO_4$ also has various applications in electronic, optoelectronics and telecommunications industries[106]. The orthorhombic *Cmcm* phase of $InPO_4$ has been synthesized *via.* co-precipitation method. In this phase, Indium atoms have six co-ordination with oxygen atoms and InO_6 octahedra form chains that propagate along *c* axis. These octahedra are linked to each other in *ab* plane through PO_4 tetrahedra. Rietveld refinement of diffraction patterns suggest that at high pressure both the zircon (Space Group $I4_1/amd$) and scheelite (Space Group $I4_1/a$) type tetragonal phases are present along with ambient orthorhombic *Cmcm* phase. In both the zircon and scheelite phases, *In* atom becomes eight coordinated with respect to the oxygen atoms while phosphorous continues to be four coordinated. The phase transitions from orthorhombic *Cmcm* phase to tetragonal phases are of first order and irreversible in nature. The observation of zircon and scheelite type tetragonal phases of $InPO_4$ under high pressure is of importance in the context of optoelectronics for exploring new phases of $InPO_4$ based compounds with desired properties.

I have carried out the high pressure studies on hexagonal phase of $YInO_3$. The studies [134] show that the compression in *ab* plane is higher than along the *c* axis. This anisotropic compression behaviour is due to open structure of $YInO_3$ along *ab* plane and leads to large value of first order pressure derivative of bulk modulus. The hexagonal phase (in which, *In* atoms are in five co-ordination) shows transformation to orthorhombic *Pnma* phase (six co-ordinated Indium atom) in the pressure range of 12 GPa - 15 GPa. It is observed that the ambient phase coexists with high pressure orthorhombic phase. This phase transformation is of first order and irreversible in nature. The hexagonal $P6_3cm$ form of $YInO_3$ is ferroelectric while the orthorhombic *Pnma* phase is paraelectric. The transformation of ferroelectric to paraelectric phase in $YInO_3$ may be useful to understand the geometric ferroelectric behaviour of $YMnO_3$ type multiferroic compound. I have also carried out the high pressure studies on cubic phase of $YInO_3$. The results show that the cubic phase of $YInO_3$ has also transformed to orthorhombic *Pnma* phase under pressure. The phase transformation is also of first order and irreversible in nature.

In short, this thesis describes the diamond anvil cell based high pressure studies on some framework structural compounds. I have observed first order irreversible phase transition and the co-ordinations of Group 3A elements with oxygen change under pressure. The results of this thesis provide insight into the nature of structural phase transitions in the framework structural compounds of Group 3A which may be useful in their future studies.

References

[1] A. Jayaraman, Scientific American ISSN 36-8733 **250**, 54 (1984).

[2] H. K. Mao and R. J. Hemley, *Rev. Mod. Phys.* **66**, 671 (1994).

[3] J. V. Badding, L. J. Parker, and D. C. Nesting, J. Solid State Chem **117**, 229 (1995).

[4] R. Reichlin, A. K. Mcmahan, M. Ross, J. Hu, R. J. Hemley, H. K. Mao, and Y. Wu, Phys. Rev. B **49**, 3725 (1994).

[5] M. Otani, K. Yamaguchi, H. Miyagi, and N. Suzuki, J. Phys. Cond. Matt. **10**, 11603 (1998).

[6] M. I. Ermets, E. Gregoryanz, H. K. Mao, R. J. Hemley, N. Mulders, and N. Zimmerman, Phys. Rev. Lett. **83**, 2797 (2001).

[7] M. I. Eremets, R. J. Hemley, H.-K. Mao, and E. Gregoryanz, Nature **411**, 170 (2001).

[8] E. Wigner and H. B. Huntington, J. Chem. Phys. **3**, 764 (1935).

[9] N. W. Ashcroft, Phys. Rev. Lett. **21**, 1748 (1968).

[10] R. P. Dias and I. F. Silvera, Science **355**, 715 (2017).

[11] X.-D. Liu, P. Dalladay-Simpson, R. T. Howie, B. Li, and E. Gregoryanz, Science **357**, eaan2286 (2017).

[12] A. F. Goncharov and V. V. Struzhkin, Science **357**, eaam9736 (2017).

[13] A. P. Drozdov, M. I. Eremets, I. A. Troyan, V. Ksenofontov, and S. I. Shylin, Nature **525**, 73 (2015).

[14] P. Baettig and E. Zurek, Phys. Rev. Latt. **106**, 237002 (2011).

[15] H. Wang, J. S. Tse, K. Tanaka, T. Iitaka, and Y. Ma, Proc.Natl. Acad. Sci. **109**, 6463 (2012).

[16] M. Somayazulu, M. Ahart, A. K. Mishra, Z. M. Geballe, M. Baldini, Y. Meng, V. V. Struzhkin, and R. J. Hemley, Physical Review letters **122**, 027001 (2019).

[17] F. Bundy, H. Hall, H. Strong, and R. Wentorf, Nature **176**, 51 (1955).

[18] Z. Zeng, et al., Nat. Commun **8**, 322 (2017).

[19] R. H. Wentorf, The Journal Of Chemical Physics **34**, 809 (1961).

[20] C. Ji, et al., Proc. Natl. Acad. Sci. **114**, 3596 (2017).

[21] M. Somayazulu, P. Dera, A. F. Goncharov, S. A. Gramsch, P. Liermann, W. Yang, Z. Liu, H. K. Mao, and R. J. Hemley, Nat. Chem **2**, 50 (2010).

[22] W. L. Mao, H. K. Mao, Y. Meng, P. Eng, M. Y. Hu, P. Chow, Y. Q. Cai, J. Shu, and R. J. Hemley, Science **314**, 636 (2006).

[23] G. N. Ramachandran and V. Sasisekaran, Adv. Protein. Chem. **23**, 283 (1968).

[24] S. K. Sikka and S. M. Sharma, Current Science **63**, 317 (1992).

[25] S. M. Sharma and S. K. Sikka, Prog. Mater. Sci. **44**, 1 (1996).

[26] G. Jaeger, Arch. Hist. Exact Sc **81**, 51 (1998).

[27] P. W. Bridgman, J. Biol. Chem **19**, 511 (1914).

[28] R. J. Hemley, P. M. Bell, and H. K. Mao, Science **237**, 605 (1987).

[29] R. J. Hemley, H. K. Mao, G. Shen, J. Badro, P. Gillet, M. Hanfland, and D. Ha¨usermann, Science **276**, 1242 (1997).

[30] R. J. Hemley, Rigaku journal **6**, 2 (1989).

[31] T. Takahashi and W. A. Bassett, Science **145**, 483 (1964).

[32] H. K. Mao and P. M. Bell, Science **103**, 1004 (1979).

[33] A.J. Gratz, L. D. Deloach, T. M. Clough, and W. J. Nellis, Science **259**, 663 (1993).

[34] Y. Tsuchida and T. Yagi, Nature **340**, 217 (1989).

[35] D. C. Palmer and L. W. Finger, American Mineralogist **79**, 1 (1994).

[36] S. Klotz, J. C. Chervin, P. Munsch, and G. L. Marchand, J. Phys.D: Appl. Phys **42**, 075413(1) (2009).

[37] S. Klotz, L. Paumier, G. L. March, and P. Munsch, High Pressure Research **29**, 649 (2009).

[38] G. N. Peggs, High pressure-high temperature. **12**, 1 (1980).

[39] J. C. Jamieson, J. N. Fritz, and M. H. Manghnani, High pressure research in geophysics, 27 (1982).

40 C. S. Zha, H. K. Mao, and R. J. Hemley, Proc. Natl. Acad. Sci.USA, **97**, 13494 (2000).

41 F. Birch, J. Geophys. Res. **83**, 1257 (1978).

42 S. M. Sharma and Y. M. Gupta, Phys. Rev. B **43**, 879 (1991).

43 J. D. Barnet, S. Block, and G. J. Piermarini, Rev. Sci. Instrum. **44**, 1 (1973).

44 G. J. Piermarini and S. Block, Rev. Sci. Instrum. **46**, 973 (1975).

45 H. K. Mao, J. Xu, and P. M. Bell, Journal of Geophysical Research- Solid Earth and Planets **91**, 4673 (1986).

46 H. K. Poswal, Ph.D. thesis Homi Bhabha National Institute, Mumbai (2013).

47 R. M. Hazen and L. W. Finger, John Wiley & Sons Ltd, New York (1982).

48 M. B. Kruger and R. Jeanloz, Science **249**, 647 (1990).

49 S. M. Sharma, N. Garg, and S. K. Sikka, Physical Review B **62**, 8824 (2000).

50 S. M. Sharma, N. Garg, and S. K. Sikka, Journal of Physics: Condensed Matter **12**, 6683 (2000).

51 J. Badro, J. P. Itié, and A. Polian, The European Physical Journal B **1**, 265 (1998).

52 J. Pellicer-Porres, A. Saitta, A. Polian, J. Paul Itié, and M. Hanfland, Nature Materials **6**, 698 (2007).

53 H. K. Poswal, N. Garg, M. Somayazulu, and S. M. Sharma, Am Mineral. **98**, 285 (2013).

54 L. C. Ming, Y. Nakamoto, S. Endo, C. H. Chio, and S. K. Sharma, J Phys Condens Matter. **19**, 425202 (2007).

55 N. L. Ross, J. Zhao, and R. J. Angel, Journal of Solid State Chemistry **177**, 1276 (2004).

56 A. P. Hammersley, S. O. Svensson, M. Hanfland, A. N. Fitch, and D. Hausermann, High Pressure Research **14**, 235 (1996).

57 H. M. Rietveld, Journal of Applied Crystallography **2**, 65 (1969).

58 A. B. Larson and R. B. Dreele, General Structure Analysis System, 86 (2000).

59 G. Caglioti, A. Paoletti, and F. P. Ricci, Nucl. Instrum. **3**, 223 (1958).

60 B. H. Toby, Journal of Applied Crystallography **34**, 210 (2001).

61 D. Long, McGraw-Hill International Book Company (1977).

62 A. F. Goncharov, International Journal of Spectroscopy **2012**, 1 (2011).

63 http://www.rrcat.gov.in/technology/accel/indus/indus2.html.

64 M. Sánchez del Río and R. J. Dejus, Status of XOP-an x-ray optics software toolkit **8141** (2011).

65 S. Mobilio and A. Balerna, Conference Proceedings-Italian Physical Society **82**, 1 (1999, 2003).

66 K. K. Pandey, H. K. Poswal, A. K. Mishra, A. Dwivedi, R. Vasanthi, Nandini Garg, and S. M. Sharma, Pramana - J. Phys **80**, 607 (2013).

67 E. F. Skelton, Adv. X-ray Anal. **31**, 1 (1988).

68 B. Buras and L. Gerward, Prog. Crystal Growth Charact. **18**, 93 (1989).

69 D. Hausermann and P. Barnes, Phase Transitions **39**, 99 (1992).

70 B. Buras and L. Gerward, International tables for crystallography, 2nd edn, edited by A J C Wilson and E Prince; Kluwer Acad. Publ.- Dordrecht, **C**, 87 (1999).

71 K. K. Pandey, H. K. Poswal, A. K. Mishra, V. Srihari, N. Garg, A. Dwivedi, R. Vasanthi, M. N. Deo, and S. M. Sharma, Physics News; Bulletin of the Indian Physics Association **48**, 48 (2018).

72 V. K. Raghuvanshi, V. P. Dhamgaye, A. K. Singh, and R. V. Nandedkar, AIP Conference Proceedings **879**, 631 (2007).

73 V. B. 6.0, Microsoft-USA (1998).

74 H. K. Mao and P. M. Bell, Science **103**, 1004 (1979).

75 F. Ciocci, World Scientific Publishing Company **chap. 9**, 287 (2001).

76 P. Kirkpatrick and A. V. Baez., J. Opt. soc. Am. **38**, 766 (1948).

77 W. H. Zachariasen, John wiley and sons (1944).

78 D. Lahiri and S. M. Sharma, Shielding Report for Indus-2 Beamlines Bhabha Atomic Research Centre **BARC / E** (2007).

79 A. E. Ringwood and S. E. Kesson, The Moon **16**, 425 (1977).

80 T. Tsuchiya and J. Tsuchiya, Proceedings of the National Academy of Sciences **108**, 1252 (2011).

81 A. F. Wright and A. J. Leadbetter, Philosophical Magazine **31**, 1391 (1975).

82 R. T. Downs and D. C.Palmer, American Mineralogist **79**, 9 (1994).

83 D. C. Palmer and L. W. Finger, American Mineralogist **79**, 1 (1994).

84 D. C. Palmer, R. J. Hemley, and C. T. Prewitt, Physics and Chemistry of Minerals **21**, 481 (1994).

85 A. J. Gratz, L. D. Deloach, T. M. Clough, and W. J. Nellis, Science **259**, 663 (1993).

86 R. C. L. Mooney, Acta Crystallogr. **9**, 728 (1956).

87 A. Perloff, J. Am. Ceram. Soc. **39**, 83 (1956).

88 J. Haines, O. Cambon, G. Fraysse, and A. Van der Lee, Journal of Physics: Condensed Matter **17**, 4463 (2005).

89 J. F. Huang, W. Yang, and L. Cao, Journal of Materials Science & Technology **26**, 1021 (2010).

90 Y. N. Pitak and Y. V. Churilova, Refractories and Industrial Ceramics **45**, 275 (2004).

91 J. Haines and O. Cambon, Z. Kristallogr. **219**, 314 (2004).

92 J. Haines, O. Cambon, D. Cachau-Herreillat, G. Fraysse, and F. E. Mallassagne, Solid State Science **6**, 995 (2004).

93 S. N. Acharya, O. D. Jayakumar, A. K. Tyagi, and S. K. Kulshresththa, Journal of Solid State Chemistry **176**, 37 (2003).

94 E. Soignard, C. J. Benmore, and J. L. Yarger, Rev Sci. Instruments **81**, 035110 (2010).

95 R. J. Angel, J. Gonzalez-Platas, and M. Alvaro, Z. Kristallogr. **229**, 405 (2014).

96 J. L. Robeson, R. R. Winters, and W. S. Hammack, Phys. Rev. Letters **73**, 1644 (1994).

97 E. Angot, et al., Physical Review Materials **1**, 033607 (2017).

98 R. Shirley, Crysfire software (http://www.webcitation.org/6CmNiWa74) (2004).

99 V. V. Murashov, Physical Review B **53**, 107 (1996).

100 A. Ĉernok, et al., Nature Communications **8**, 15647 (2017).

101 J. Badro, D. M. Teter, R. T. Downs, P. Gillet, R. J. Hemley, and J.-L. Barrat, Physical Review B **56**, 5797 (1997).

102 G. Kresse and J. Furthmuller, Phys. Rev. B **54**, 11169 (1996).

103 G. Kresse and D.Joubert, Phys. Rev. B **59**, 1758 (1999).

104 J. P. Perdew, K. Burke, and M. Ernzerhof, Phys. Rev. Lett. **77**, 3865 (1996).

105 H. J. Monkhorst and J. D. Pack, Phys. Rev. B **13**, 5188 (1976).

106 O. Pluchery, J. Eng Jr., R. L. Opila, and Y. J. Chabal, Surf. Sci. **502**, 75 (2002).

107 A. Dwivedi, H. K. Poswal, K. K. Pandey, H.-P. Liermann, C. Murli, M. N. Deo, and High Pressure Research **39**, 81 (2019).

108 R. C. Mooney, H. Kissinger, and A. Perloff, Acta Cryst. **7**, 642 (1954).

109 M. Bosacka, Thermochimica Acta **523**, 137 (2011).

110 S. L´opez-Moreno and D. Errandonea, Physical Review B **86**, 104112 (2012).

111 E. Go¨rlich, PAN, Krako´w (1997).

112 G. Korotcenkov, I. Boris, A. Cornet, J. Rodriguez, A. Cirera, V. Golovanov, Y. Lychkovsky, and G. Karkotsky, Sens Actuators **B120**, 657 (2007).

113 M. Rojas-L´opez, J. Nieto-Navarro, E. Rosendo, H. Navarro-Contreras, and M. A. Vidal, Thin Solid Films **379**, 1 (2000).

114 M. Hanfland, H. Beister, and K. Syassen, Phy. Rev. B **39**, 12598 (1989).

115 F. D. Murnaghan, Proc. Natl. Acad. Sci. **30**, 244 (1944).

116 D. Errandonea, A. Muñoz, and J. Gonzalez-Platas, Journal of Applied Physics **115**, 216101(1) (2014).

117 L. Gracia, A. Beltran, and D. Errandonea, Physical Review B **80**, 094105 (2009).

118 D. Errandonea and A. B. Garg, Progress in Materials Science **97**, 123 (2018).

119 N. Fujimura, T. Ishida, T. Yoshimura, and T. Ito, Appl. Phys. Lett. **69**, 1011 (1996).

[120] D. Ito, N. Fujimura, T. Yoshimura, and T. Ito, J. Appl. Phys. **93**, 5563 (2003).

[121] E. F. Bertaut, E. F. Forrat, and P. H. Fang, C. R. Acad. Sci. Paris. **256**, 1958 (1963;).

[122] H. L. Yakel, W. C. Koehler, E. F. Bertaut, and E. F. Forrat, Acta Cryst. **16**, :957 (1963).

[123] B. B. V. Aken, T. T. M. Palstra, A. F. Petti, and N. A. Spaldin, Nat. Mater. **3**, 164 (2004).

[124] R. E. Cohen, Nature **358**, 136 (1992).

[125] R. D. Shannon, Acta Crystallogr. **A32**, 751 (1976).

[126] A. A. Nugroho, N. Bellido, U. Adem, G. Nénert, Ch. Simon, M. O. Tjia, M. Mostovoy, and T. T. M. Palstra, Physical Review B **75**, 174435(1) (2007).

[127] H. D. Zhou, J. C. Denyszyn, and J. B. Goodenough, Phys. Rev. B **72**, 224401(1) (2005).

[128] C. W. F. T. Pistorius and G. J. Kruger, J. Inorg. Nucl. Chem. **38**, 1471 (1976).

[129] S. C. Abrahams, Acta Crystallogr. B **57**, 485 (2001).

[130] T. Tohei, H. Moriwake, H. Murata, A. Kuwabara, R. Hashimoto, T. Yamamoto, and I. Tanaka, Phy. Rev. B **79**, 144125(1) (2009).

[131] R. Shukla, S. K. Gupta, V. Grover, V. Natarajan, and A. K. Tyagi, Dalton Trans. **44**, 10628 (2015).

[132] D. L. Heinz and R. Jeanloz, J. Appl. Phys. **55**, 885 (1984).

[133] R. Shukla, F. N. Sayed, V. Grover, S. K. Deshpande, A. Guleria, and A. K. Tyagi, Inorg Chem. **53**, 10101 (2014).

[134] A. Dwivedi, H. K. Poswal, R. Shukla, S. Velaga, B. D. Sahoo, V. Grover, and M. N. Deo, High Pressure Research **39**, 17 (2019).

[135] C. Lin, J Liu, Y. Li, and X. Li, Solid State Commun. **173**, 51 (2013).

[136] P. Gao, Z. Chen, T. A. Tyson, T. Wu, K. H. Ahn, Z. Liu, R. Tappero, S. B. Kim, and S.-W. Cheong, Phys. Rev. B: Condens. Matter Mater. Phys. **83**, 224113(1) (2011).

[137] D. Errandonea, C. Ferrer-Roca, and D Martínez-Garcia et al., Physical Review B **82**, 174105(1) (2010).

[138] M. Ceperley and B. J. Alder, Phys. Rev. Lett. **45 (7)**, 566 (1980).

[139] C. Lin, J. Liu, and X Li et al., J Appl Phys. Rev. B **112**, 113512(1) (2012).

[140] L. J. Wang, S. M. Feng, and J L Zhu et al., High Press. Res. **30**, 258 (2010).

[141] D. L. Rousseau, R. P. Bauman, and S. P. S. Porto, J. Raman Spectrosc. **10**, 253 (1981).

[142] R. Shukla, V. Grover, and S. K. Deshpande et al., Inorg Chem **52**, 13179 (2013).

[143] N. Arai, N. Saito, and H. Nishiyama et al., Chem. Lett. **37**, 46 (2008).

[144] M. N. Iliev, H.-G. Lee, and V. N. Popov et al., Phys. Rev. B **56**, 2488 (1997).

[145] A. E. Smith, H. Mizoguchi, and K Delaney et al., J. Am. Chem. Soc. **131**, 17084 (2009).